Measuring open charm hadron production at 7 TeV using the LHCb detector

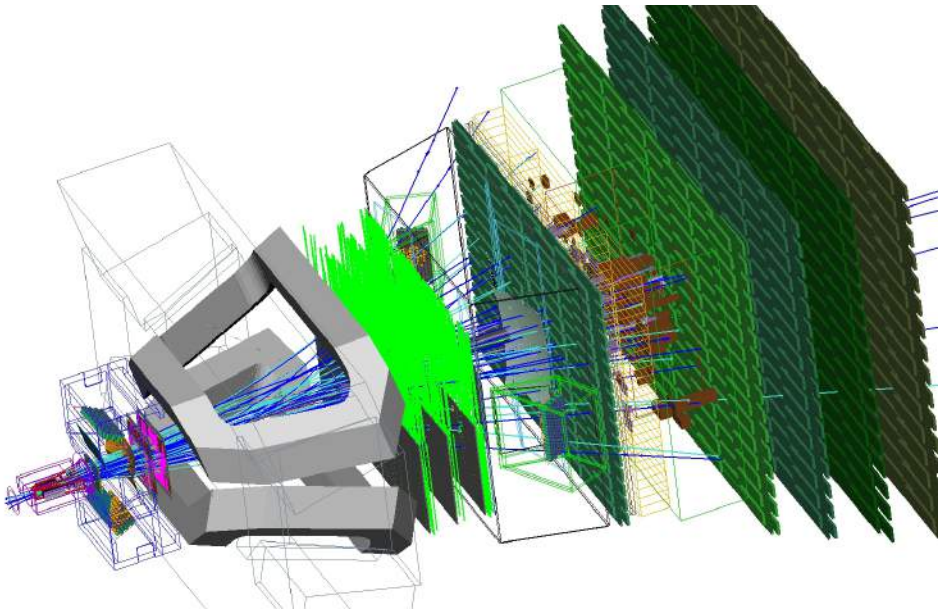

A dissertation presented by
Christopher Burr
to
The School of Physics and Astronomy

in partial fulfillment of the requirements
for the degree of
Master of Particle Physics

University of Southampton
Southampton, United Kingdom
May 2015

Thesis advisor: Sajan Easo Christopher Burr

Measuring open charm hadron production at 7 TeV using the LHCb detector

Abstract

Using data taken by the LHCb detector at $\sqrt{s} = 7$ TeV during 2011 the normalised double differential production cross-sections of D^0, D^{*+}, D^+, D_s^+ and L_c^+ are presented in bins of rapidity and transverse momentum. Comparisons are also made to the previous LHCb measurement at $\sqrt{s} = 7$ TeV[1] and, where available, to theoretical predictions obtained using the FONLL model[2]. This analysis has been developed for the start of LHC Run 2 where the LHCb collaboration will repeat this measurement at $\sqrt{s} = 13$ TeV.

Acknowledgments

With many thanks to Patrick Spradlin and my supervisor Sajan Easo for providing guidance and support. To Alex Pearce and Dominik Müller with whom this analysis is being performed. Finally, I would like to give special thanks to The University of Southampton, Rutherford Appleton Laboratory and the course coordinator Professor Stefano Moretti for both the opportunity to attend the 2015 Institute of Physics conference and without whom this project would not have been possible.

Contents

Listing of figures

List of Tables

1 Introduction

This thesis will outline the progress that has been made toward measuring the production cross-sections of D^0, D^{*+}, D^+, D_s^+ and Λ_c^+ in bins of transverse momentum and rapidity at $\sqrt{s} = 7\,\text{TeV}$ using data taken in 2011 by the LHCb detector. The measurement has been previously performed using LHCb data taken in 2010[1] and this analysis serves to cross-check the 2010 measurement as well as validating the new analysis strategy that will be used for a measurement at $\sqrt{s} = 13\,\text{TeV}$ during the initial weeks of LHC Run 2. Preliminary results for the normalised, bin integrated, cross-sections are presented with comparisons to the previous LHCb results. In addition comparisons are made to theoretical predictions calculated using the FONLL model where available.

Chapter 3 begins with a discussion of the motivation for these measurements and presents a selection of ways in which the previous result has been used. This is followed by a summary of the methodology used for calculating the results with a description the the dataset. The hadron selections, yield extraction and efficiency determination are then described in Chapter 5, 6 and 7 respectively. Penultimately the status of the ongoing evaluation of the uncertainties associated with these measurements are shown before presenting the preliminary results in Chapter 9.

2

The LHCb detector

The Large Hadron Collider (LHC) is a 27 km synchrotron at CERN in Geneva, Switzerland, which primarily produces proton-proton collisions for the fundamental physics research conducted by the ATLAS, CMS, LHCb and ALICE collaborations.

A series of older accelerators from the CERN accelerator complex (Figure 2.0.1) are used as pre-accelerators to the LHC. Initially protons are produced using a duoplasmatron and are subsequently accelerated by LINAC2 to 50 MeV. The Proton Synchrotron Booster (PBS) then accelerates the protons to 1.4 GeV before injecting them into the Proton Synchrotron (PS) where they are accelerated to 26 GeV. Finally the protons are accelerated to 450 GeV using the Super Proton Synchrotron (SPS) and injected into the Large Hadron Collider which has a design energy of 14 TeV.[1] The beam of the LHC is made up of 2,808 bunches each containing approximately 1.15×10^{11} protons which corresponds to a bunch spacing of 25 ns around the ring.[2]

The Large Hadron Collider beauty (LHCb) experiment is situated approximately 100 m underground at point 8 of the Large Hadron Collider and unlike the general purpose detectors which aim for the highest integrated luminosities possible LHCb is designed for lower luminosities as is clear from Figure 2.0.2. This lower luminosity is achieved by fixing the mean number of visible proton-proton interactions[3] in each bunch crossing, μ, through a feedback loop which varies the transverse distance between the beams in order to maintain a constant instantaneous luminosity as shown in Figure 2.0.3.

[1] To date the centre of mass collision energies used have been 7 TeV and 8 TeV in 2011 and 2012 respectively, the first 13 TeV collisions are expected to occur in May 2015.

[2] While the design bunch spacing is 25 ns the 2010-2012 data taking periods used reduced number of bunches and a 50 ns bunch spacing. The first data that will be used for physics with 25 ns bunch spacing will be taken in 2015.

[3] "Visible" is used to describe the collisions which result in interactions rather than scattering and is generally taken to be 69.9 % of the total number of proton-proton interactions.

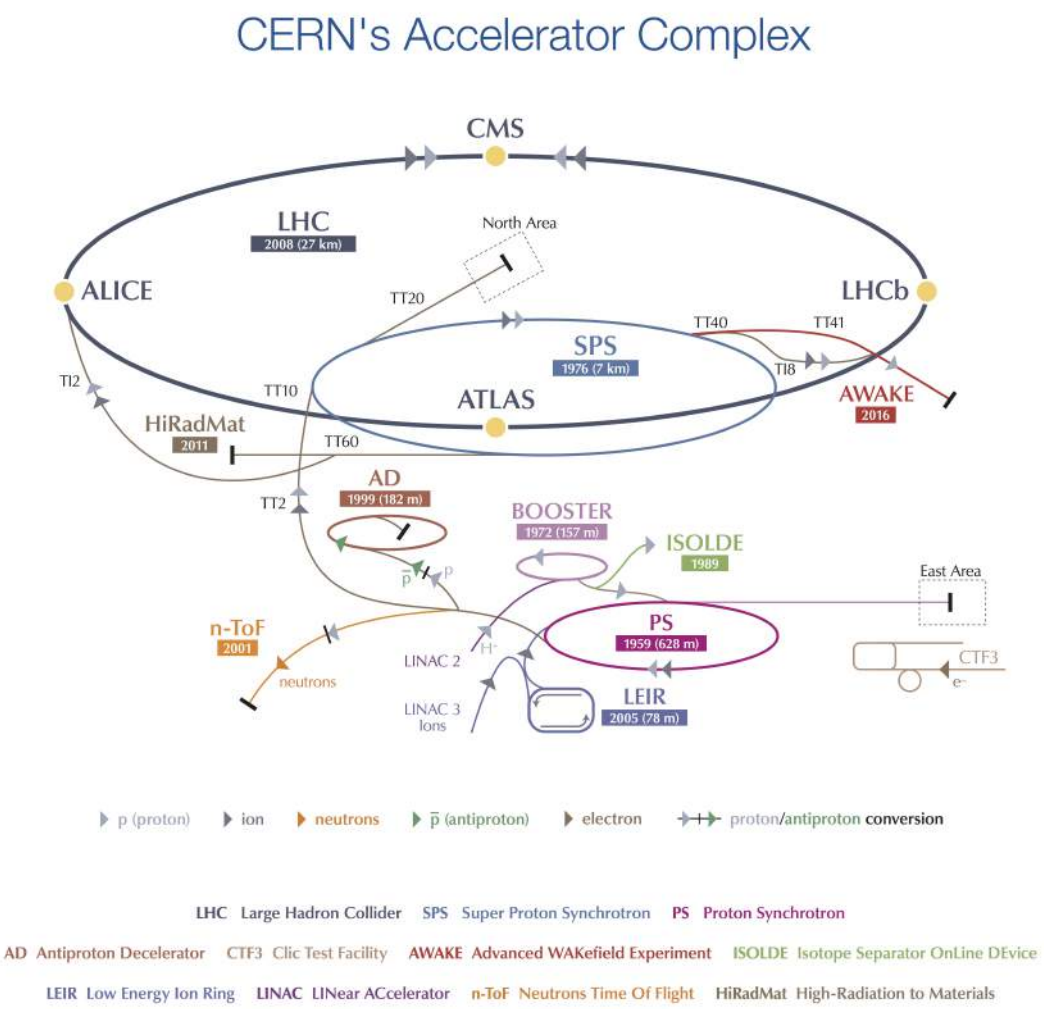

Figure 2.0.1: The layout of the CERN accelerator complex[3].

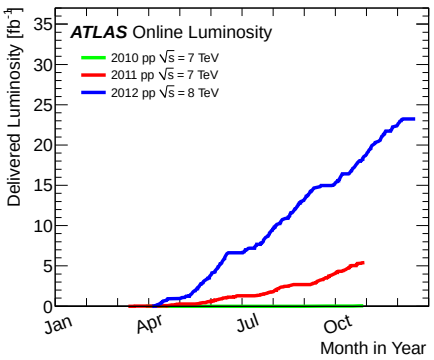

(a) ATLAS[4]

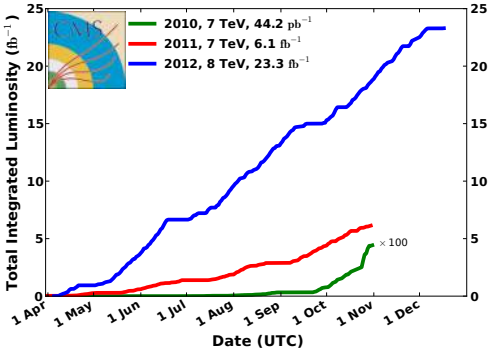

(b) CMS[5]

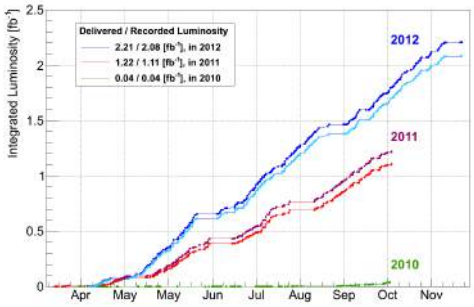

(c) LHCb[6]

Figure 2.0.2: Plots of the total integrated luminosity collected by each detector at the LHC in 2010, 2011 and 2012.

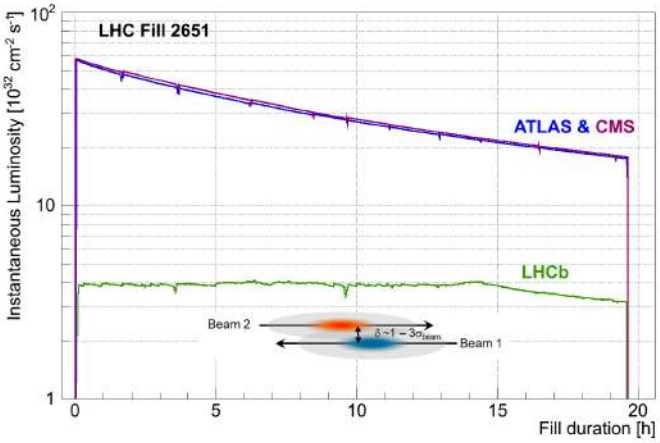

Figure 2.0.3: Variation in the instantaneous luminosity at the ATLAS, CMS and LHCb interaction points.[7]

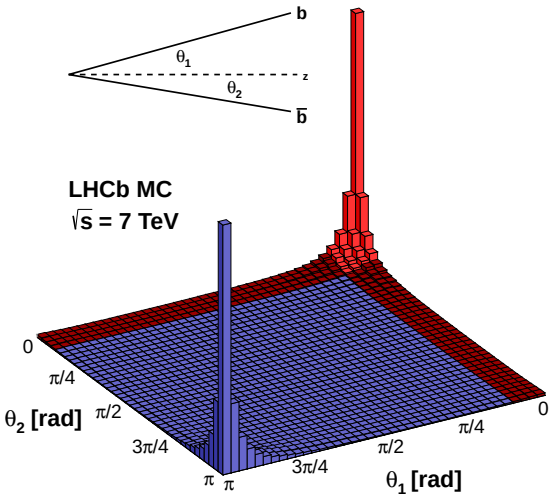

Figure 2.0.4: Plot of the rapidity distribution of $b\bar{b}$ production, taken from [8]

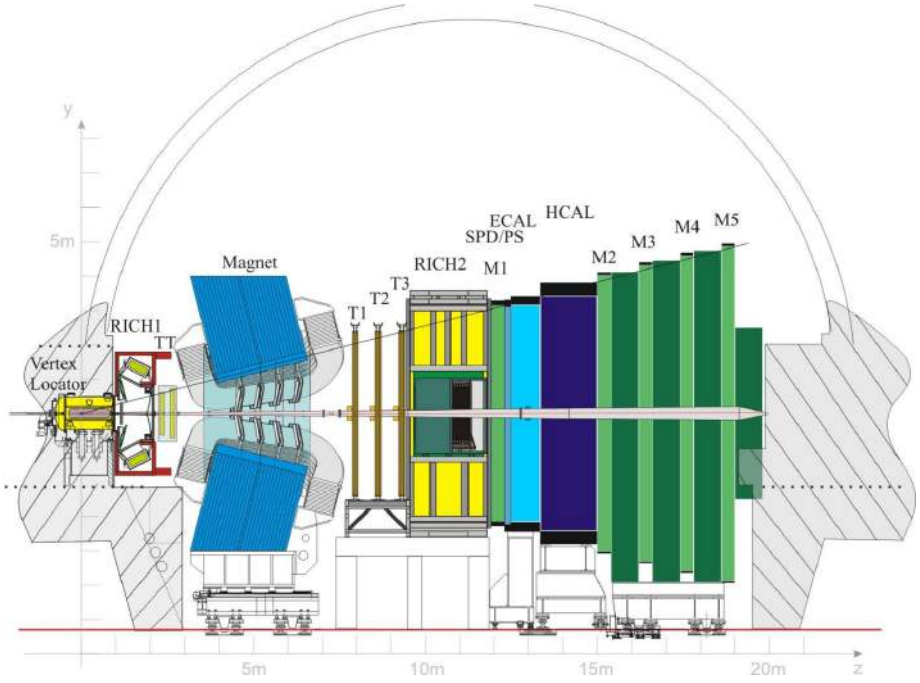

Figure 2.0.5: Cross-section of the LHCb detector[9].

2.1 The LHCb detector

The LHCb detector is a single armed forward spectrometer, covering the pseudorapidity[4] range $2 < \eta < 5$ (15 to 300 mrad)[10], which is designed to perform precision measurements of beauty and charm quarks which are favourably produced near to the beam pipe as shown in Figure 2.0.4. The forward design also allows the majority of the detector to be made in flat planes perpendicular to the beam pipe with the majority of readout electronics and physical support structures being kept outside the acceptance of the detector. This reduces the amount of passive material that particles must pass though in order to be detected and allows LHCb to have excellent momentum resolution. In addition, LHCb is designed to efficiently provide the flavour tagging of particles therefore opening a wide range of opportunities, particularly in the measurement of CP violation.

The detector itself is made up of a vertex locator, five tracking stations, two ring imaging Cherenkov detectors, an electromagnetic calorimeter, a hadronic calorimeter and five muon detectors arranged as in Figure 2.0.5.

2.2 Vertex Locator

The LHCb detector's vertex locator (VELO) is unique at the LHC as it can be moved between a distance of 35 mm and 7 mm from the beam of the LHC. This movement is necessary to protect the VELO during the initial injection of protons when the beam is unstable and may deviate from its nominal path. After each fill of the LHC, the position of the beam is measured and the VELO is manoeuvred into position prior to the start of data taking.

The VELO itself is made up of 42 modules of silicon strip detectors with a pitch of 38 µm to 102 µm which varies linearly from the beam edge. Each module provides a measurement of the r and ϕ coordinates and are arranged as shown in Figure 2.2.1 to optimise the reconstruction performance.

The close proximity of the VELO to the LHC beam allows for an excellent primary vertex (PV) resolution of 13 µm in the transverse plane and 71 µm in the axis parallel to the beam[11]. In addition, thanks to its close proximity to the interaction point, the VELO is also able to directly observe tracks from B-mesons, which have a typical lifetime of 10^{-12} s, opening up opportunities for precision lifetime measurements and the study of processes such as B_s^0 mixing[12].

[4] See Equation 5.1 for a definition of pseudorapidity.

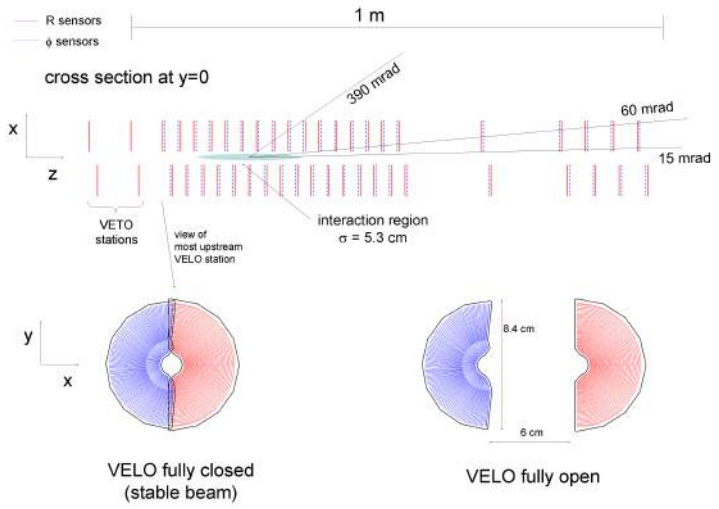

Figure 2.2.1: Top: Cross-section in the x-y plane of the LHCb VELO. Below: Example of two modules in the close and open position where the left, blue, half measures the angular component and the right, red, half measures the radial position.

2.2.1 Silicon Tracker

The Silicon Tracker is comprised of two parts; the Tracking Turicensis (TT) and the Inner Tracker (IT). Both parts are comprised of four vertical silicon microstrip detectors with a strip pitch of around 200 µm in a x-u-v-x layout of where the inner two layers, u and v, are rotated by $-5°$ and $5°$ respectively. The TT is located upstream of the magnet and covers the full acceptance of the detector. In contrast, the IT is placed downstream of the magnet and only covers the innermost region of the acceptance where the occupancy is greatest. The remainder of the acceptance is measured using the Outer Tracker as described in the following section. In all elements of the Silicon Tracker the length of the silicon strips is varied to minimise the occupancy expected in any given strip while reducing the number of required readout channels.

2.2.2 Outer Tracker

The Outer Tracker (OT) is a drift-time detector and is comprised of around 55,000 hollow tubes containing a gas mixture and a thin wire in the centre. When a charged particle enters the tube the gas mixture is ionised resulting in the delocalisation of electrons which are then attracted towards the charged wire in the centre. As the electron drifts a phenomena known as Townsend discharge occurs increasing the number of electrons to a level at where they can be detected by electronics at the end of the wire. Rather than being limited to the spacial spacing of the straws, the resolution can be improved by measuring the time since the last beam crossing to establish the

distance from the wire at which the particle travelled. The gas mixture is chosen such that the maximum drift time is 50 ns to minimise spillover from other bunch crossings.[5]

2.3 Particle Identification

Particle Identification (PID) is used for distinguishing between long lived particles which have similar characteristics in the detector such as; protons, pions and kaons or neutral pions and photons. The main elements of LHCb for distinguishing these charged hadrons are the calorimeters and the two ring-imaging Cherenkov detectors named RICH 1 and RICH 2.

2.3.1 Ring Imaging Cherenkov Detectors

RICH detectors contain a medium with refractive index (η) slightly greater than 1 therefore when charged particles pass through the detector Cherenkov radiation is emitted at an angle, θ_c, given in Equation 2.1. As this is related to the velocity of the particle, v, this can be combined with a momentum measurement to give a mass hypothesis. Plotting track momentum against Cherenkov angle (Figure 2.3.1) shows the formation of bands, each of which corresponds to a different species of particle.

$$\cos\left(\theta_c\right) = \frac{c}{\eta v} \tag{2.1}$$

As pions are the most commonly produced particle at the LHC a log-likelihood algorithm is used to perform a ratio likelihood test of whether a candidate is an electron, kaon, muon or proton against the likelihood that the candidate is a pion. Below threshold (9.3 GeV for kaons and 17.8 GeV for protons in RICH 1) the refractive indices of the RICH detectors are too small to produce Cherenkov radiation and the log-likelihood must instead be calculated in veto mode, i.e. the likelihood that this track is not a pion.

The likelihood produced by the RICH is combined with the likelihoods provided by the other PID subdetectors in LHCb to provide delta-log-likelihood (DLL) variables which can be used as particle identification discriminant. A more advanced set of variables, ProbNN, are also provided by the LHCb collaboration which are produced by training a neural network with the log-likelihood variables calculated from each subdetector with track properties, such as p, p_T, and various quality variables. This results in a more powerful discriminant with the added advantage that it defines a normalised Bayesian probability for each hypothesis.

[5] For 25 ns data taking the hits in the OT from the previous and following bunch crossing are used during reconstruction due to the drift time having some potential overlap.

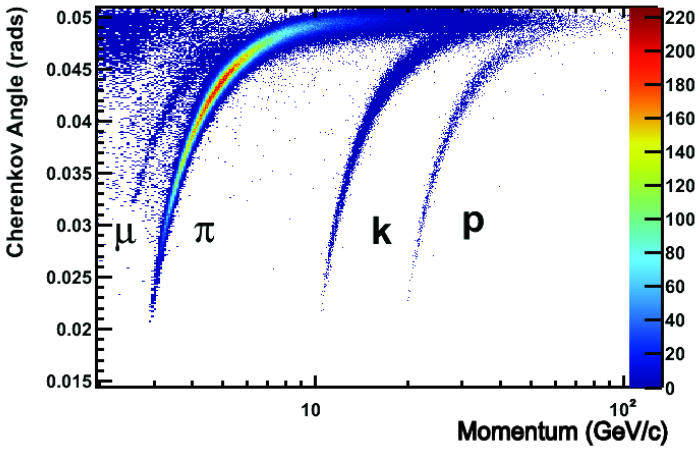

Figure 2.3.1: Plot of Cherenkov angle against momentum for 2 % of the real data taken at $\sqrt{s} = 7\,\text{TeV}$ in the C_4F_{10} radiator of RICH 1[7].

2.3.2 Calorimeters

In addition to Particle Identification, calorimetry is used to measure the energy and position of electrons, photons and hadrons as well as providing signal for them at the lowest level of the LHCb trigger, prior to any tracking considerations. All calorimeters follow the principle that scintillation light, that is light that is emitted due to the presence of ionising radiation, is measured by photon detectors. In LHCb wavelength shifting fibres are used to convert these photons into the spectral range of multianode photomultiplier tubes. The first layer of the LHCb calorimeter is the Scintillator Pad Detector and is used to distinguish between charged and neutral particles as they enter the calorimeter and is then followed by the PreShower which distinguishes between electrons, photons and pions. These are both primarily used to provide a signal for the trigger. The Electromagnetic Calorimeter measures the transverse energy of electrons, photons and neutral pions and is used in the reconstruction of such particles, whereas, the Hadronic Calorimeter is mostly used to provide a transverse energy measurement for triggering purposes.[13]

2.4 Simulation

For evaluation of efficiencies Monte Carlo events are generated using Pythia 8[14] with a specific LHCb configuration[15]. The decays of hadronic states are then simulated using EvtGen[16] and final state radiation is modelled using PHOTOS[17]. Detector effects and interactions are implemented using GEANT4[18] as described in Reference [19].

3 Motivation

Production cross-sections form a group of essential measurements that must be performed by all collider based experiments early in their running in order to assist in the analysis of the remainder of their datasets. For example they are used to tune Monte Carlo generators and to understand the properties of standard model backgrounds in searches for new physics. This section will describe some of the ways in which the previous measurement by LHCb has been used.

3.1 Comparison with theoretical models

The measurement of open charm production provides an interesting test of QCD dynamics particularly in the forward region and at high transverse momenta. A selection of theoretical models exists including the "Fixed Order + Next-to-Leading Log" (FONLL) framework by Cacciari et al.[2] and the "General-Mass Variable-Flavour-Number Scheme" (GMVFNS) by Kniehl et al.[20] both of which have produced predictions for the previous LHCb measurement. In general, predictions in the charm sector prove challenging for theorists and for cross-section measurements the production of charm with low transverse momentum is plagued with large errors as assumptions regarding the charm quark mass fail. On the other hand increasing transverse momentum results in large logarithms which require resummation and challenges experimentalists with exponential reduction of the cross-section limiting the statistical confidence that can be obtained. Despite this the high luminosities and energies available at the LHC allows for precise tests of theory as was shown by the previous measurement (Figure 3.1.1) where predictions were provided for both the FONLL and GMVFNS models.

3.2 Parton distribution functions

Parton distribution functions (PDFs) describe the complex internal structure of protons by calculating the probability that a specific species of parton, that is a quark or a gluon,

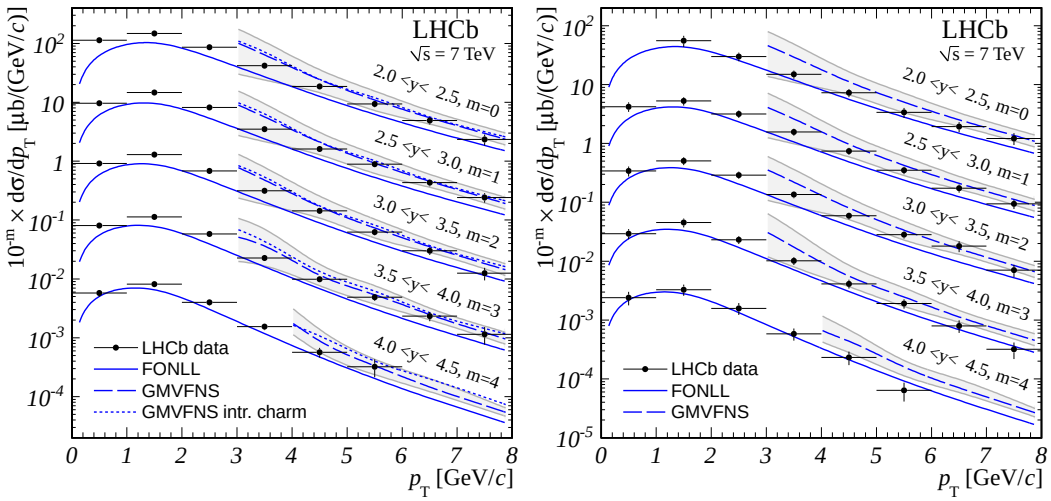

(a) D^0 **(b)** D^{*+}

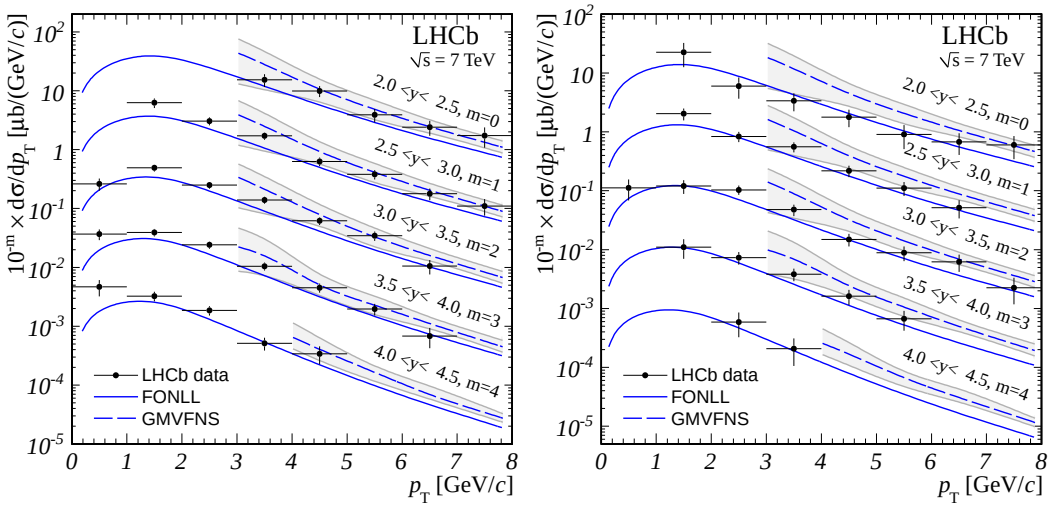

(c) D^+ **(d)** D_s^+

Figure 3.1.1: Differential cross-sections in p_T of the specified charm hadron presented along side predictions from the FONLL and GMVFNS models[1]. Note the use of m as a scaling factor to separate the results for each rapidity range.

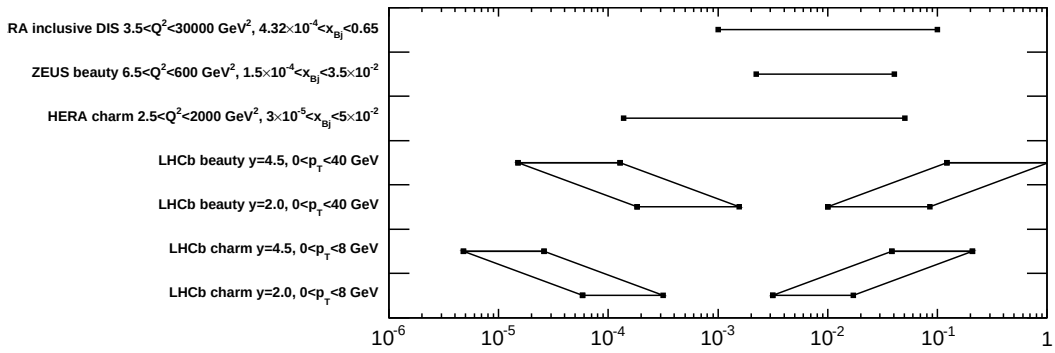

Figure 3.2.1: Plot showing the kinematic range of x probed by various datasets.[25]

will exist with a specified fraction of the proton's momentum, x, at a given energy scale. Several PDFs have been produced by the phenomenological community such as HERAPDF[21], CTEQ[22], MSTW[23] and NNPDF[23] and all of these rely upon data to constrain the parameters that exist in each approach.

HERAFitter[24] is an open-source fitting framework for PDFs and is produced at DESY for the PDF set, HERAPDF. This primarily uses the cross-section measurements of deep inelastic lepton-proton scattering (DIS) processes by the ZEUS and H1 collaborations as the input data, however, this dataset is limited to the region $10^{-4} \lesssim x \lesssim 10^{-1}$. The PROSA collaboration have therefore investigated the potential of the LHCb dataset for extending this region, motivated by the the leading order approximation in Equation 3.1. This describes the scale of x probed by calculating the cross-section of a heavy quark with mass, m_Q, in proton-proton collisions each with a beam energy, E_p, in a region of transverse momentum, p_T, and rapidity, y.

$$x = e^{\pm y} \frac{\sqrt{p_T^2 + m_Q^2}}{E_p} \tag{3.1}$$

As shown in Figure 3.2.1, the LHCb dataset compliments the existing HERA data in part thanks to the acceptance of the LHCb detector being particularly suited to extending the range of PDFs by exploiting the exponential increase in reach that comes with increasing rapidity. The effect of using normalised and absolute cross-sections on the fitted PDFs is shown in Figure 3.2.2 and demonstrates a significant improvement in the PDF uncertainties, particularly when using normalised cross-sections.

3.3 Atmospheric backgrounds in neutrino experiments

Recent advancements in neutrino detectors have allowed for the first observations of neutrinos with energies in the PeV range. With experiments such as IceCube investigating extraterrestrial sources of neutrinos[26] there is a need to understand and

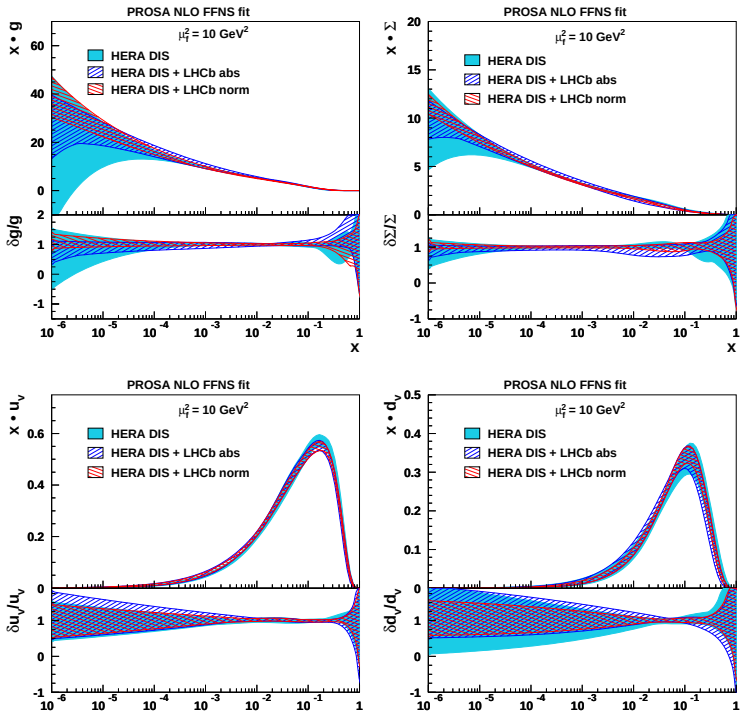

Figure 3.2.2: Results provided by PROSA showing the improvement the LHCb dataset has when included in the HERAFitter input for the; gluon (top left), sea-quark (top right), up-valence quark (bottom left) and down-valence quark (bottom right).[25]

quantify the atmospheric backgrounds that are present at these high energies. These arise from interactions between cosmic rays and atmospheric nuclei with ~PeV neutrinos corresponding to an incident energy of ~30 PeV. Such energies are unreachable to modern fixed target experiments however the LHC, with a centre of mass energy of 7 TeV, is equivalent to a incoming cosmic ray of 26 PeV. Therefore LHC cross-sections prove useful in improving the constrains on these backgrounds as demonstrated by Bhattacharya et al.[27]

4
Methodology

4.1 Calculation

There exists a variety of options for reporting the open production cross-section of charm hadrons from proton-proton collisions, all of which require the yield, N_i, to be extracted from the dataset. The simplest of these is to measure is the total integrated cross-section of a specified hadron within a region of transverse momentum and rapidity as shown in Equation 4.1 where H_c is the hadron under study, f represents the final state decay products and $c.c.$ shows that the charge conjugation of the process is also included.

$$\sigma_i\left(H_c\right) = \frac{N_i\left(H_c \to f + c.c.\right)}{\epsilon_{i,\text{tot}}\left(H_c \to f\right) \cdot \mathscr{B}\left(H_c \to f\right) \cdot \mathscr{L}_{\text{int}}} \tag{4.1}$$

The extracted yield must be corrected to account for any events which have been lost due to inefficiencies as described in Chapter 7. This factor is denoted by ϵ_{tot} and represents the combination of many effects from both the physical detector and the analysis techniques used. Another correction must then be applied to the yield to obtain the total number of hadrons of the specified species that have been produced, rather than the number which are undergo a specific decay. This factor is known as the branching ratio, $\mathscr{B}$, and is taken from the Particle Data Group's (PDG) review of particle physics[28], an annual publication which congregates and averages the results obtained by all relevant experiments in a single freely accessible document.

Once the other terms have been calculated the cross-section is obtained using the measured total integrated luminosity that the dataset corresponds to, $\mathscr{L}_{\text{int}}$. From the total integrated cross-section an estimation can be made for the double differential cross-section at any point within a region of phase space, i, by dividing the integrated cross-section by the size of the region in both transverse momentum and rapidity, as in Equation 4.2.

$$\left.\frac{\partial^2\sigma_i\left(H_c\right)}{\partial p_T \partial y}\right|_i \approx \frac{\sigma_i\left(H_c\right)}{\Delta p_T \Delta y} \tag{4.2}$$

At the time of writing a measurement for the total integrated luminosity of the available 2011 dataset is not available and therefore absolute cross-sections cannot be measured. Despite this the groups mentioned in Section 3.1 have stated that measurements involving ratios dramatically reduce the theoretical uncertainty of their predictions, thus allowing for higher precision comparisons. Ratios also result in a cancellation of the luminosity dependence and therefore the preliminary results presented here are of cross-sections normalised to single phase space bin.

4.2 Data

The dataset used for this analysis was collected in 2011 during LHC Run 1 at a centre of mass energy of 7 TeV with an average of 1.4 inelastic collisions per bunch crossing. This lower than design energy was used due to concerns for the safety of the machine following the accident in 2008[29]. In addition the LHC ran at a reduced bunch spacing of 50 ns corresponding to a 20 MHz rate of data collection. A pass-though trigger was used for this measurement which stores a random sample of events to disk with no selections applied. This trigger was chosen to prevent the difficulties which arise when calculating the absolute efficiency of the L0Hadron trigger.

To allow for cross checks of the analysis the dataset was split by the polarity of the magnet to obtain two approximately equal subsets which are referred to as MagUp and MagDown. This not only allows for two statistically independent datasets to be compared but also provides a test of detector asymmetries which may bias the result. Simulated data is produced for both magnet polarities therefore each dataset can be analysed in isolation to each other. All results presented in his document are from the MagDown dataset unless explicitly stated.

4.3 Decay channels

The decay channels used for this measurement are selected in order to maximise the number of fully selected events and as such channels with large branching ratios are favoured. In addition, the efficiency by which the decays can be selected is important, therefore, the measurement cross-sections typically favour decays involving muons as has been used in the previous LHCb measurements, such as the J/ψ cross-section[30]. Leptonic decays are however impractical for the measurement of other charm hadrons due to the extremely small Leptonic branching ratio. Table 4.3.1 lists the modes used for this measurement alongside their branching ratios taken from the 2014 edition of the PDG review of particle physics[28]. In all cases both the stated channel and the charge conjugation have been combined for this measurement.

Hadron	Decay channel	Branching Ratio
D^0	$K^-\pi^+$	$(3.88 \pm 0.05) \times 10^{-2}$
D^0	$K^-\pi^+\pi^-\pi^+$	$(8.08 \pm 0.21) \times 10^{-2}$
D^{*+}	$D^0\pi^+$	0.677 ± 0.005
D^+	$K^-\pi^+\pi^+$	$(9.13 \pm 0.19) \times 10^{-2}$
D^+	$K^-K^+\pi^+$	$(9.54 \pm 0.26) \times 10^{-3}$
D_s^+	$K^-K^+\pi^+$	$(5.39 \pm 0.21) \times 10^{-2}$

Table 4.3.1: Hadrons included in this measurement with the decay modes and respective branching ratio.

5 Event Selection

In order to obtain candidates for the decay which is to be studied the data collected must have selections applied to reduce the background which is present in the dataset. The most common background which is present in almost all modern HEP experiments at hadron colliders is combinatoric background. This is when the reconstruction algorithm has incorrectly combined the tracks which have been found by the tracking algorithm into candidates and is generally formed a of a smooth linear background which prior to any selections being applied dramatically reduces the statistical significance of any true candidates, as shown in Figure 5.1.1.

5.1 Strategy

Initially the effectiveness of two differing selection strategies was evaluated using $D^0 \to K^-\pi^+$ the first of which used the rectangular cuts from the previous LHCb open charm cross-section measurement. The alternative strategy which was investigated was to use multivariate techniques where a classifier is trained using a two samples one of which is known to be signal and the other which is representative of the background which is to be removed. The classifier can then be used to obtain a variable, like in Figure 5.1.2, which is proportional to the confidence the classifier has that a particular event displays signal-like characteristics. This variable can then be cut upon to provide a particular signal and background efficiency as is shown by the ROC curve in Figure 5.1.3.

The first decision that must be made when using multivariate techniques is to decide upon signal and background samples for the classifier to be trained with. One option is to use a signal sample generated using Monte Carlo techniques and a background sample of the events from the mass distribution that exist outside the region containing the peak. This option has the benefit of being easy to implement and provides good description of combinational backgrounds whose characteristics typically have very little dependence on the reconstructed mass, however, the quality of the signal sample is dependent upon having high quality Monte Carlo generators.

Figure 5.1.1: Plot of the D^0 mass for $D^0 \to K^-\pi^+$showing that background is dominant despite being a high yield mode and having some preselection applied.

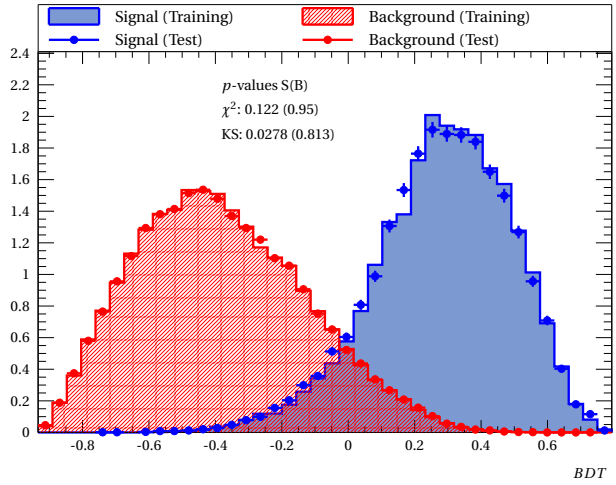

Figure 5.1.2: Normalised histogram of the classifier response to the training datasets where red is used to represented the signal events and blue is used to represent background events. The shaded region and points show the response of the BDT to the training and testing samples respectively and demonstrate there is no evidence for overtraining in the classifier.

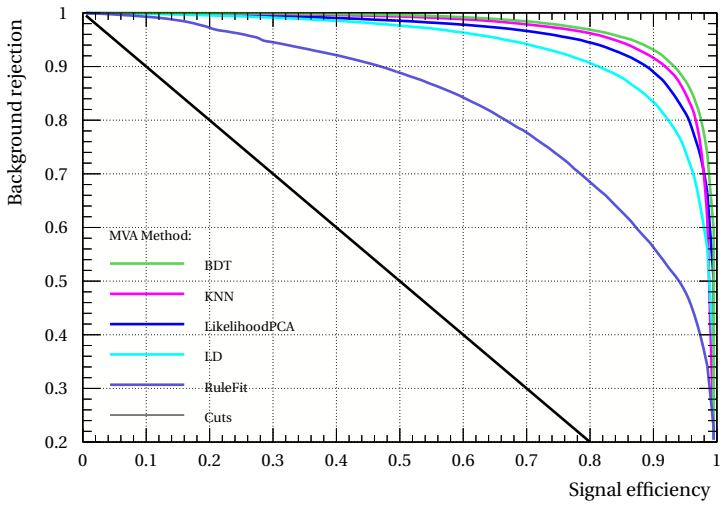

Figure 5.1.3: Plot of the background vs signal efficiency (ROC curve) for selection of multivariate algorithms trained to select $D^0 \to K^-\pi^+$.

The main alternative source for a training data is to use a technique known as sPlot[31] for which real events are fitted to obtain an estimated signal yield. Each event is given a weight which describes to what extent the MVA training should "trust" the features of that event. This method has the advantage of being data driven and therefore should perfectly describe the data which is to be selected however it requires that am estimated yield can be obtained by fitting the mass distribution of the mother hadron.

The Monte Carlo signal/data side-band background option was chosen for the training dataset as the mass distributions for most of the decay modes in this study peak in the mass distribution small in comparison to the background weakening the sPlot method. In addition simulated events are used for evaluating the efficiency of the selection and therefore any variables which aren't well described by the Monte Carlo generators are undesirable for inclusion in the training even if they are well described by the training dataset.

Due to the vast of background produced by the reconstruction algorithm and the limited computing resources available, it is necessary to preform a preselection of rectangular cuts on the events prior to the BDT. This selection was developed by examining the cuts used in the previous analysis and loosening the cuts which had the worst efficiency or those that caused a shaping in the efficiency in the rapidity and transverse momentum of the mother particle. This is undesirable as it introduces a systematic uncertainty as described in Section 10.

For the classifier the selection of multivariate algorithms (MVAs) available in TMVA[32] were each evaluated and it was found that a binary decision tree (BDT) produced the optimal separation between signal and background. To find variables

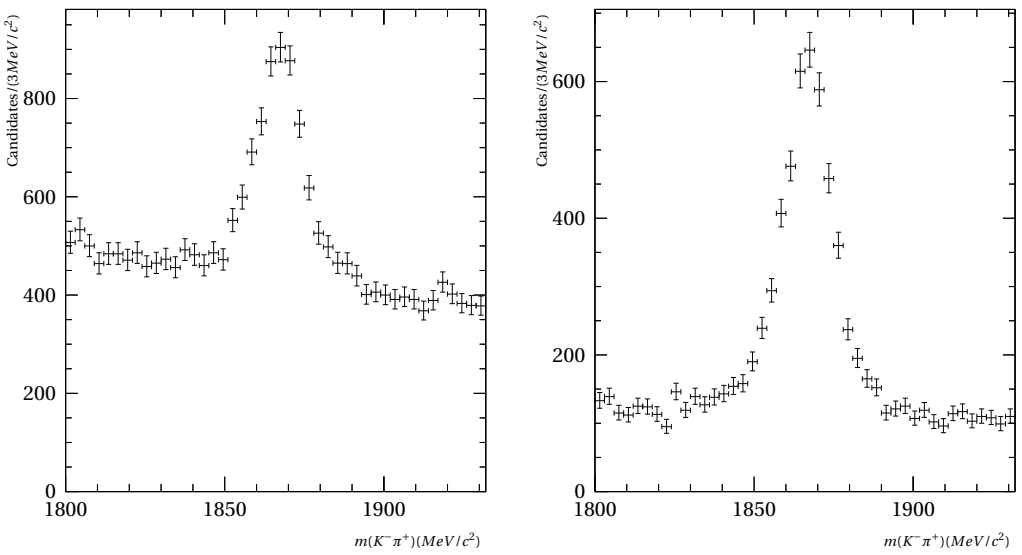

(a) **(b)**

Figure 5.1.4: Comparison between the cut based selection used in 2010 (a) and a preliminary BDT based selection (b).

which could potentially provide discriminatory power the normalised distributions were plotted for the signal and background samples so they could be inspected for differences which might be exploitable by the BDT. The result of this study was then used to train a preliminary classifier from which variables were iteratively removed until only those which provided significant improvement remained.

The result from the two strategies is presented in Figure 5.1.4 and shows that the BDT provides significant improvements over traditional cut based selection.

5.2 Choice of variables

The cuts applied during the selection of candidates fall into two categories, some are used to account for physical properties or limitations of the detector while the majority are used for their ability to discriminate between signal and background. Here the meaning of variables and the motivation for their use is discussed.

Child transverse momentum p_T

Transverse momentum corresponds to the vector sum of the x and y components of the track's momentum where the z axis is defined as being along the beam. This discriminates upon the property that any child from the decay of a charm hadron will typically have a larger transverse momentum than a child produced

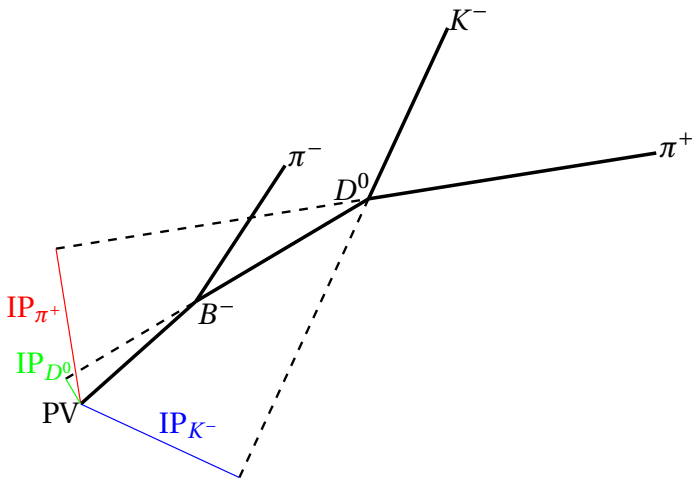

Figure 5.2.1: Graphic showing the meaning of the impact parameter with PV referring to the primary vertex.

directly at the primary vertex.

Child momentum, p

Any track for which PID cuts are applied must be constrained to the range $2\,\mathrm{GeV} < p < 100\,\mathrm{GeV}$ due to the limited calibration samples available for calculating the efficiency of the aforementioned PID cut as discussed in Section 7.4.

Child pseudorapidity, η

The pseudorapidity of a track is a measure of the angle, θ, of a track relative to the beam axis and is defined by Equation 5.1. A pseudorapidity of zero is perpendicular to the beam, increasing to infinity which corresponds to the beam axis itself. The motivation for constraining pseudorapidity to the range $2 < \eta < 5$ is due to the acceptance of the LHCb detector.

$$\eta = -\ln\left(\tan\left(\frac{\theta}{2}\right)\right) = -\ln\left(\frac{p + p_L}{p - p_L}\right) \tag{5.1}$$

Child impact parameter χ^2

The impact parameter corresponds to the closest distance a track makes to the primary vertex when extrapolated backwards as shown in Figure 5.2.1. In addition a χ^2 test is a statistical measure which can be used to assess the quality of a fitted quantity as described in [33]. The impact parameter χ^2 is then the difference in the fit quality of the primary vertex when the track is either included or excluded. The daughters of charm decays are typically produced far from the primary vertex

and therefore result in a much reduced quality of fit, i.e. a large impact parameter χ^2.

Child DLL variables, $\mathrm{DLL}_{K-\pi}$

The delta log likelihood (DLL) variables describe the likelihood that the track is of one species relative to another, in the above case the likelihood that the track is a kaon relative to being a pion. These variables are born of the particle identification system described in Section 2.3.1 with further detail available in Reference [34]. DLL variables were chosen over their ProbNN counterparts as this analysis will be repeated early in LHC Run 2 with the selection applied in the trigger, as part of the new Turbo stream[35], where ProbNN variables will not initially be available.

Mother mass constraint, $m_{\mathrm{PDG}}(D^0) - m(K^-\pi^+)$

Due to the finite resolution of the detector the reconstructed invariant mass from any child particles is not exactly equal to the known mass in the PDG.[1] As a result a mass window must be used to keep the useful two body combinations. This range is also set to contain enough candidates outside the mass peak to allow for fitting of the combinatoric background as described in Chapter 6.

Mother vertex fit χ^2

The child tracks of a candidate mother can never exactly intersect to give a vertex at which the mother decayed therefore a χ^2 test is performed on the fit of this vertex. Large values corresponds to tracks which are unlikely to originate from the same vertex.

Mother direction angle

The angle between the sum of the child track momenta and the vector that intersects both the primary vertex and the reconstructed mother vertex. If both the child tracks have been correctly associated and fitted this angle should be zero.

Mother vertex displacement

The ground state of excited hadrons typically decay though weak interactions and as such have observably long lifetimes. Two parameters are used to discriminate on the lifetime, one is to use the proper lifetime (τ) directly, the other is to perform a χ^2 as described for the child impact parameter χ^2.

[1] This effect can also be observed in the case of very short lived particles having poorly defined masses from the uncertainty principle however this effect is not observable in any of these measurements.

Decay axis angle, $\cos(\theta_\pi)$

The cosine of the angle between the momentum of the pion in the D^0rest frame and the momentum of the D^0meson in the lab frame. In $D^0 \to K^-\pi^+$this value is seen to peak towards $|\cos(\theta_\pi)| = 1$ in background candidates while remaining isotropic for signal.

Distance of closest approach

This refers to the largest distance of closest approach (DOCA) measured out of all combinations of the parent's daughter tracks and clearly likely candidates are expected to minimise this quantity.

5.3 Selection tables

Tables 5.3.1 to 5.3.5 shows the selections that were found for use in this analysis. A different preselection and BDT was used for each decay mode with exception of $D^+$where individual selections were shown to give a statistically insignificant improvement, likely due to the the BDT's input variables lack of daughter dependence. As a result a single selection was used with the BDT being trained using $D^+ \to K^-K^+\pi^+$signal and background.

Particle	Variable	Cut value	BDT Input
K^-, π^+	p_T	$> 250\,\text{MeV}$	✓
	p	$3 < p < 100\,\text{GeV}$	-
	η	$2 < \eta < 5$	✓
	Impact parameter χ^2	> 4	-
π^+	$\text{DLL}_{K-\pi}$	< 3	-
K^-	$\text{DLL}_{K-\pi}$	> 5	-
D^0	$m_{\text{PDG}}(D^0) - m(K^-\pi^+)$	$< 80\,\text{MeV}$	-
	Vertex fit χ^2	< 25	✓
	Direction angle	$< 35\,\text{mrad}$	✓
	Vertex displacement	$VD\chi^2 > 16$ OR $\tau > 0.150\,\text{ps}$	-
	Proper time	-	✓
	$\cos(\theta_\pi)$	-	✓
	BDT discriminant	> 0.2	-
D^{*+}	$m(K^-\pi^+\pi^+_{\text{Soft}}) - m(K^-\pi^+)$	$< 160\,\text{MeV}$	-
	Vertex fit χ^2	< 25	-

Table 5.3.1: Selections used for $D^0 \to K^-\pi^+$

Particle	Variable	Cut value	BDT Input
$\pi^{\pm}$, K^{-}	p_T	$> 200, 300, 350, 400\,\text{MeV}$	✓
	p	$3 < p < 100\,\text{GeV}$	-
	η	$2 < \eta < 5$	✓
	Impact parameter χ^2	> 4	-
$\pi^{\pm}$	$\text{DLL}_{K-\pi}$	< 3	-
K^{-}	$\text{DLL}_{K-\pi}$	> 5	-
D^0	$m_{\text{PDG}}(D^0) - m(K^-\pi^+\pi^-\pi^+)$	$< 80\,\text{MeV}$	-
	DOCA	$< 0.5\,\text{mm}$	✓
	Vertex fit χ^2	< 25	✓
	Direction angle	$< 35\,\text{mrad}$	✓
	Vertex displacement	$VD\chi^2 > 16$ OR $\tau > 0.150\,\text{ps}$	-
	Proper time	-	✓
	$\cos(\theta_\pi)$	-	✓
	BDT discriminant	> 0.1	-

Table 5.3.2: Selections used for $D^0 \to K^-\pi^+\pi^-\pi^+$where "$A$, B, C, D" requires at least one child track to pass the strongest selection, two to pass the second strongest selection etc.

Particle	Variable	Cut value	BDT Input
$\pi^{\pm}$, $K^{\pm}$	p_T	$> 200, 400, 400\,\text{MeV}$	-
	p	$3 < p < 100\,\text{GeV}$	-
	η	$2 < \eta < 5$	-
	Impact parameter χ^2	$> 4, 10, 50$	-
$\pi^{\pm}$	$\text{DLL}_{K-\pi}$	< 3	-
$K^{\pm}$	$\text{DLL}_{K-\pi}$	> 5	-
D^+	$m(h^-h^+h^+)$	$1790 < m < 1940\,\text{MeV}$	-
	DOCA	$< 0.5\,\text{mm}$	✓
	Vertex fit χ^2	< 25	✓
	Direction angle	$< 35\,\text{mrad}$	✓
	Vertex displacement	$VD\chi^2 > 16$ OR $\tau > 0.150\,\text{ps}$	-
	Vertex displacement χ^2	-	✓
	Proper time	-	✓
	Flight distance	-	✓
	BDT discriminant	> 0.15	-

Table 5.3.3: Selections used for $D^+ \to K^-K^+\pi^+$and $D^+ \to K^-\pi^+\pi^+$where "A, B, C" requires at least one child track to pass the strongest selection, two to pass the second strongest selection etc.

Particle	Variable	Cut value	BDT Input
π^+, K^-	p_T	$> 200\,\text{MeV}$	`max`, `min`
	p	$3 < p < 100\,\text{GeV}$	-
	η	$2 < \eta < 5$	-
	Impact parameter χ^2	> 4	-
π^+	$\text{DLL}_{K-\pi}$	< 3	-
K^-	$\text{DLL}_{K-\pi}$	> 5	-
ϕ	$m_{\text{PDG}}(\phi) - m(K^-K^+)$	$< 20\,\text{MeV}$	-
D_s^+	$m(\phi\pi^+)$	$1900 < m < 2050\,\text{MeV}$	-
	DOCA	-	✓
	Vertex fit χ^2	< 25	✓
	Direction angle	$< 35\,\text{mrad}$	✓
	Vertex displacement	$VD\chi^2 > 25$ OR $\tau > 0.150\,\text{ps}$	-
	Vertex displacement χ^2	-	✓
	Proper time	-	✓
	Flight distance	-	✓
	BDT discriminant	> 0.05	-

Table 5.3.4: Selections used for $D_s^+ \to (\phi \to K^-K^+)\pi^+$where "$A$, B, C" requires at least one child track to pass the strongest selection, two to pass the second strongest selection etc.

Particle	Variable	Cut value	BDT Input
π^+, K^-, p	p_T	$> 200, 400, 1000\,\text{MeV}$	`max`, `min`
	p	$3 < p < 100\,\text{GeV}$	-
	η	$2 < \eta < 5$	-
	Impact parameter χ^2	$> 4, 4, 6$	-
π^+	$\text{DLL}_{K-\pi}$	< 3	-
K^-	$\text{DLL}_{K-\pi}$	> 5	-
p	$\text{DLL}_{p-\pi}$	> 10	-
	DLL_{p-K}	> 5	-
Λ_c^+	$m_{\text{PDG}}(\Lambda_c^+) - m(pK^-\pi^+)$	$< 90\,\text{MeV}$	-
	DOCA	$< 0.5\,\text{mm}$	-
	Vertex fit χ^2	< 25	✓
	Direction angle	$< 35\,\text{mrad}$	✓
	$\cos(\theta_\pi)$	-	✓
	Vertex displacement	$VD\chi^2 > 4$ OR $\tau > 0.075\,\text{ps}$	-
	Vertex displacement χ^2	-	✓
	Proper time	-	✓
	BDT discriminant	> 0.1	-

Table 5.3.5: Selections used for $\Lambda_c^+ \to pK^-\pi^+$where "$A$, B, C" requires at least one child track to pass the strongest selection, two to pass the second strongest selection etc.

5.4 Selected mass distributions

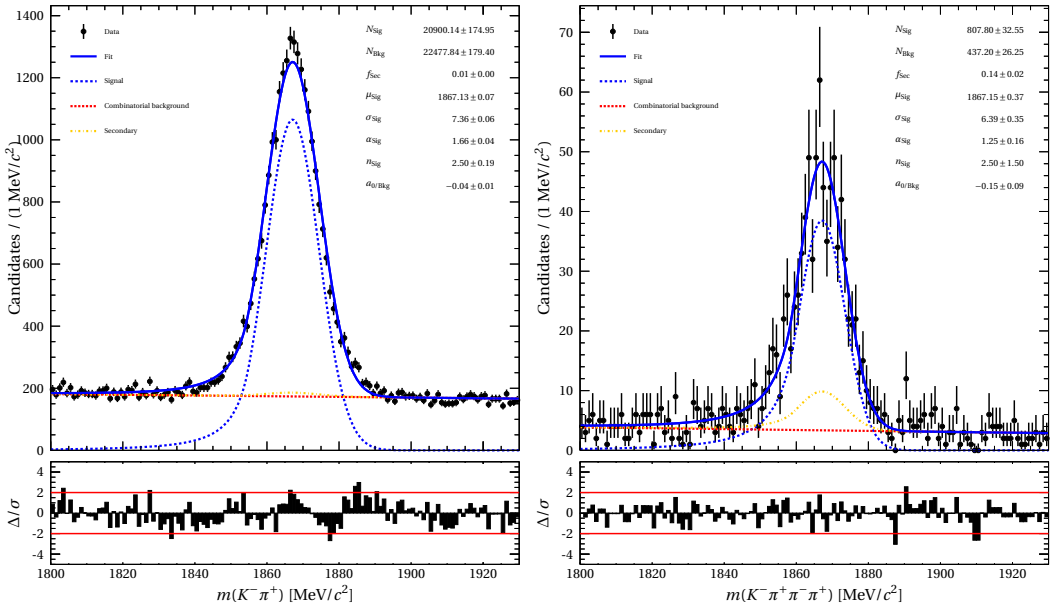

(a) $D^0 \to K^-\pi^+$ **(b)** $D^0 \to K^-\pi^+\pi^-\pi^+$

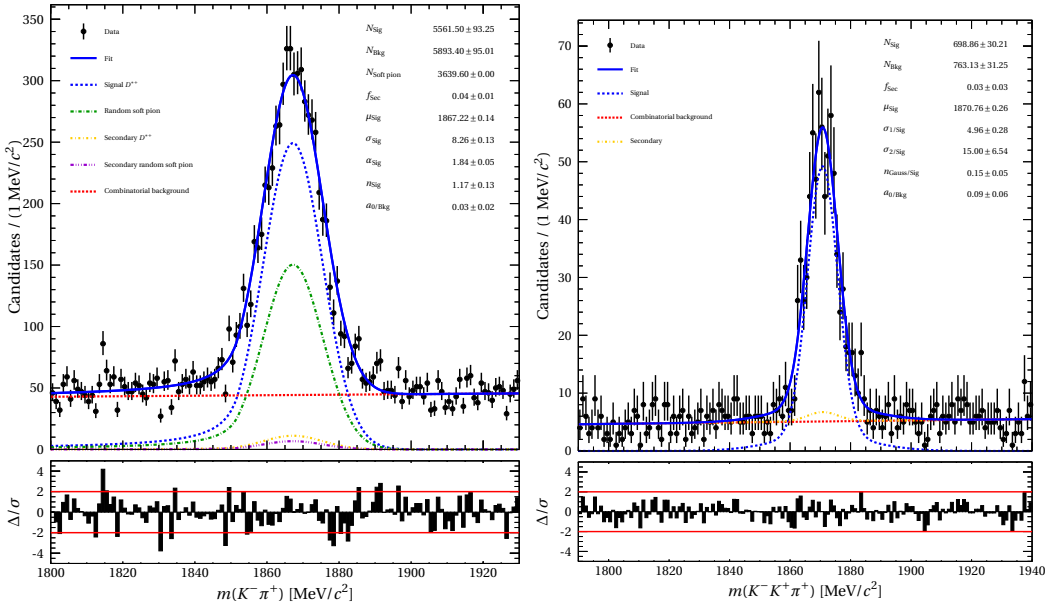

(c) $D^{*+} \to \left(D^0 \to K^-\pi^+\right)\pi^+$ **(d)** $D^+ \to K^-K^+\pi^+$

Figure 5.4.1: Fully selected mass distributions for the 2011 `MagDown` dataset.

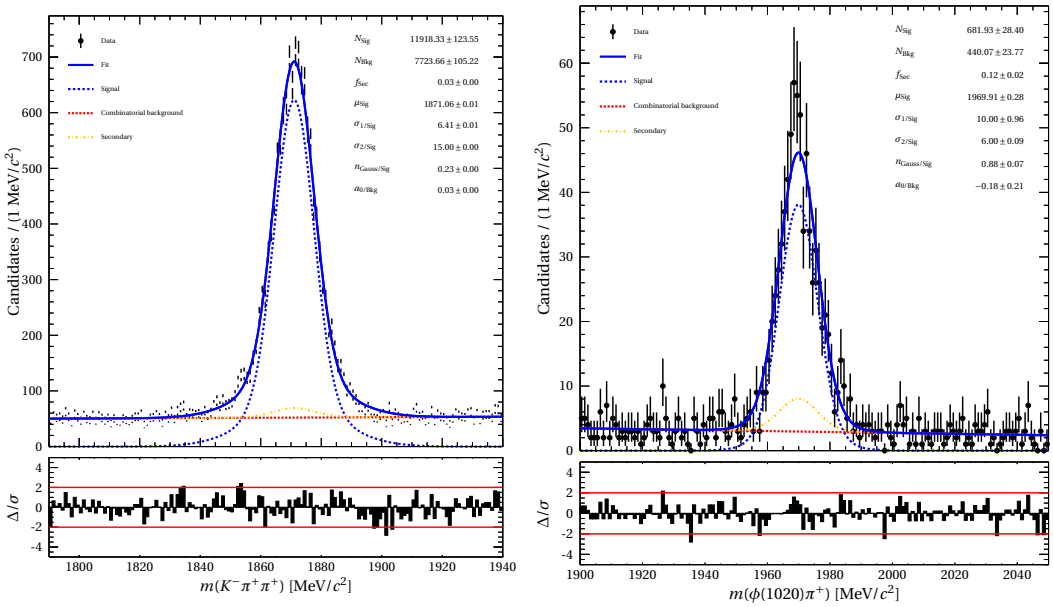

(a) $D^+ \to K^-\pi^+\pi^+$

(b) $D_s^+ \to (\phi \to K^-K^+)\pi^+$

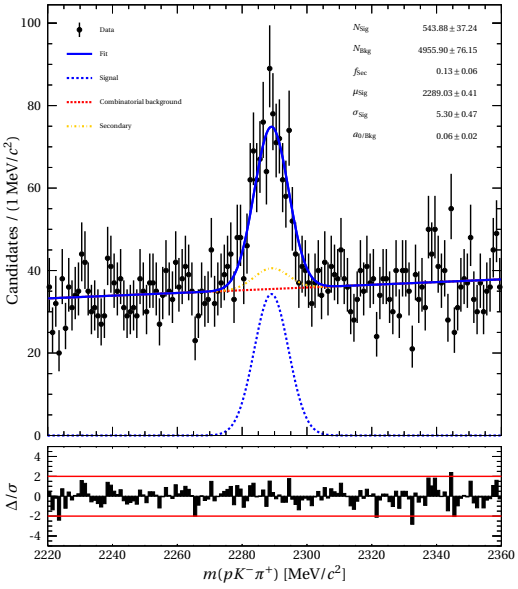

(c) $\Lambda_c^+ \to pK^-\pi^+$

Figure 5.4.2: Fully selected mass distributions for the 2011 `MagDown` dataset.

6
Yield Extraction

Once selected candidates have been obtained a signal yield must be extracted by performing a fit to the data. From this fit three yields are extracted, including the number of candidates that are classified as both signal events and as combinatorial background. The last parameter that is extracted is the fraction of secondariness in the signal yield, where a candidate is defined as secondary if was produced by the decay of a b quark as opposed to being prompt and produced directly at the primary vertex from the proton-proton interaction.

First, to extract these quantities a series of four prefits are used to obtain values for parameters of the probability density function (PDF) that are fixed in across the full transverse momentum/rapidity phase space, as shown in Figure 6.1.1. These fits are performed to candidates from across the entire LHCb acceptance.

Mass shape

This fit is performed to the mass distribution of real data and is used to contain any parameters in the signal mass probability density function.

Prompt signal IP χ^2 shape

This fit is performed to the impact parameter χ^2 shape of prompt signal Monte Carlo events that have pass the selection that has been applied to the data, less any particle identification cuts. A parent hadron is classified as prompt if the total lifetime of any ancestor particles is less than 0.1 fs.

Secondary signal IP χ^2 shape

This fit is performed to the impact parameter χ^2 shape of secondary selected signal Monte Carlo events where an event is secondary if it fails the aforementioned ancestor lifetime cut.

Combinatorial background IP χ^2 shape

This fit is performed to the impact parameter χ^2 shape of fully selected data candidates that exist outside the signal peak of the mass distribution and are therefore known to be background.

		Mass		$\ln\left(\mathrm{IP}\chi^2\right)$			δm	
Hadron	Decay channel	Sig	Bkg	Sig	Sec	Bkg	Sig	Bkg
D^0	$K^-\pi^+$	SGS	FOP	AGE	AGE	BGS		
D^0	$K^-\pi^+\pi^-\pi^+$	SGS	FOP	AGE	AGE	AGE		
D^+	$K^-\pi^+\pi^+$	SGS	FOP	AGE	BGS	BGS		
D^+	$K^-K^+\pi^+$	SGS	FOP	AGE	BGS	BGS		
D_s^+	$\phi\pi^+$	SGS	FOP	AGE	BGS	BGS		
D^{*+}	$D^0\pi^+$	SGS	FOP	AGE	BGS	BGS	SCB	DST
Λ_c^+	$pK^-\pi^+$	SGS	FOP	AGE	BGS	BGS		

Table 6.0.1: Table of the PDF components used for each decay channel where the three digit codes and method for combining the components are explained in Section 6.1.

After performing the prefits a simultaneous unbinned 2D fit is performed across all bins where the unbinned refers to the fact that the distributions of the fit variables are not placed into histograms and are instead fitted directly.

In the case of D^{*+} a 3 dimensional fit is used to allow the slow pion background to be measured. The additional fit parameter used is the delta mass, $\delta m = m\left(D^{*+}\right) - m\left(D^{*0}\right)$, where these masses correspond to the reconstructed invariant mass of the child tracks rather than the known PDG values. The motivation for using δm as opposed to $m\left(D^{*+}\right)$ is due to this distribution peaking more sharply therefore typically proving easier for numeric minimisation techniques. In addition the δm distribution is less strongly correlated with $m\left(D^0\right)$ further assisting in the fitting of the distributions.

6.1 Probability density functions

The probability density function used for each hadron and mode has been determined heuristically to provide a good description of the observed distributions in both real and simulated candidates. There is also no reason to expect the distributions to be identical for all hadrons and decay channels and these differences are present in the PDFs that have been used in the fitting procedure. The PDF used for each component of the fits are in Table 6.0.1 where the three digit codes refer to:

SGS Gaussian

A normal distribution with mean, μ, and standard deviation, σ.

$$f_{\mathrm{SGS}}\left(x;\mu,\sigma\right) = e^{-\frac{(x-\mu)^2}{2\sigma^2}} \tag{6.1}$$

`FOP` **First order polynomial**

A linear polynomial with gradient a and y-intercept b.

$$f_{\texttt{FOP}}\left(x;a,b\right) = ax + b \tag{6.2}$$

`AGE` **Gaussian with asymmetric exponential tails**

A modified Gaussian PDF with exponential tails of strength ρ_L and ρ_R either side of the mean μ and an asymmetrical width σ governed by ϵ.

$$f_{\texttt{AGE}}(x;\mu,\sigma,\epsilon,\rho_L,\rho_R) = \begin{cases} e^{\frac{\rho_L^2}{2}+\rho_L\cdot\frac{x-\mu}{(1-\epsilon)\cdot\sigma}} & x < \mu-(\rho_L\cdot\sigma\cdot(1-\epsilon)), \\ e^{-\left(\frac{x-\mu}{\sqrt{2}\cdot\sigma\cdot(1-\epsilon)}\right)^2} & \mu-(\rho_L\cdot\sigma\cdot(1-\epsilon)) \le x < \mu, \\ e^{-\left(\frac{x-\mu}{\sqrt{2}\cdot\sigma\cdot(1+\epsilon)}\right)^2} & \mu \le x < \mu+(\rho_R\cdot\sigma\cdot(1+\epsilon)), \\ e^{\frac{\rho_R^2}{2}-\rho_R\cdot\frac{x-\mu}{(1+\epsilon)\cdot\sigma}} & x \ge \mu+(\rho_R\cdot\sigma\cdot(1+\epsilon)) \end{cases} \tag{6.3}$$

`BGS` **Bifurcated Gaussian**

A modified Gaussian PDF with an asymmetrical width σ_L and σ_R either side of the mean μ.

$$f_{\texttt{BGS}}(x;\mu,\sigma_L,\sigma_R) = \begin{cases} e^{\frac{(x-\mu)^2}{2\sigma_L^2}} & x < \mu, \\ e^{\frac{(x-\mu)^2}{2\sigma_R^2}} & x \ge \mu \end{cases} \tag{6.4}$$

`SCB` **Single crystal ball**

A Crystal Ball function, that is Gaussian with an n$^t h$ order power-law tail on the left hand side starting $\alpha\sigma$ before the central value.

$$f_{\texttt{SCB}}(x;\mu,\sigma,\alpha,n) = \begin{cases} e^{-\frac{(x-\mu)^2}{2\sigma^2}} & \frac{x-\mu}{\sigma} > -\alpha, \\ \left(\frac{n}{|\alpha|}\right)^n \cdot e^{-\frac{|\alpha|^2}{2}} \cdot (\frac{n}{|\alpha|} - |\alpha| - \frac{x-\mu}{\sigma})^{-n} & \frac{x-\mu}{\sigma} \le -\alpha \end{cases} \tag{6.5}$$

`DST` **Empirical δm background shape**

A commonly used shape for δm distributions with free parameters; A, B and C and a cut off δm_0 below which the PDF evaluates to zero.

$$f_{\texttt{DST}}(x;\delta m_0,A,B,C) = \left(\frac{x}{\delta m_0}\right)^A \cdot (1 - e^{-\frac{x-\delta m_0}{C}}) + B\cdot\left(\frac{x}{\delta m_0} - 1\right) \tag{6.6}$$

The total PDF for the 2D fit with observables; m and $\mathrm{IP}\chi^2$, is:

$$\begin{aligned} f(m,\ \log(\mathrm{IP}\chi^2)) = & N_{\mathrm{sig}} \cdot f_{\mathrm{sig}}(m) \cdot f_{\mathrm{sig}}(\log \mathrm{IP}\chi^2) \\ & + N_{\mathrm{sec}} \cdot f_{\mathrm{sig}}(m) \cdot f_{\mathrm{sec}}(\log \mathrm{IP}\chi^2) \\ & + N_{\mathrm{bkg}} \cdot f_{\mathrm{bkg}}(m) \cdot f_{\mathrm{bkg}}(\log \mathrm{IP}\chi^2), \end{aligned} \tag{6.7}$$

and the total PDF for the 3D fit with observables; m, $\mathrm{IP}\chi^2$ and δm is:

$$\begin{aligned} f(m,\ \log(\mathrm{IP}\chi^2),\ \delta_m) = & N_{\mathrm{sig}} \cdot f_{\mathrm{sig}}(m) \cdot f_{\mathrm{sig}}(\delta_m) \cdot f_{\mathrm{sig}}(\log \mathrm{IP}\chi^2) \\ & + N_{\mathrm{sec}} \cdot f_{\mathrm{sig}}(m) \cdot f_{\mathrm{sig}}(\delta_m) \cdot f_{\mathrm{sec}}(\log \mathrm{IP}\chi^2) \\ & + N_{\mathrm{Rnd}_\pi} \cdot f_{\mathrm{sig}}(m) \cdot f_{\mathrm{bkg}}(\delta_m) \cdot f_{\mathrm{sig}}(\log \mathrm{IP}\chi^2) \\ & + N_{\mathrm{Sec}_\pi} \cdot f_{\mathrm{sig}}(m) \cdot f_{\mathrm{bkg}}(\delta_m) \cdot f_{\mathrm{sec}}(\log \mathrm{IP}\chi^2) \\ & + N_{\mathrm{bkg}} \cdot f_{\mathrm{bkg}}(m) \cdot f_{\mathrm{bkg}}(\delta_m) \cdot f_{\mathrm{bkg}}(\log \mathrm{IP}\chi^2). \end{aligned} \tag{6.8}$$

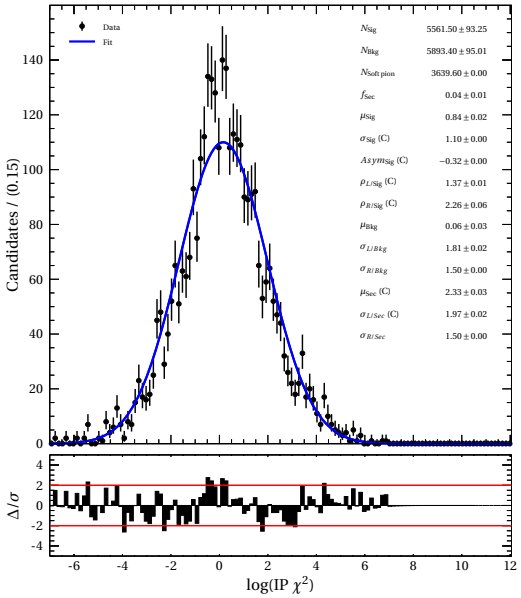

(a) D^0 impact parameter χ^2 background prefit

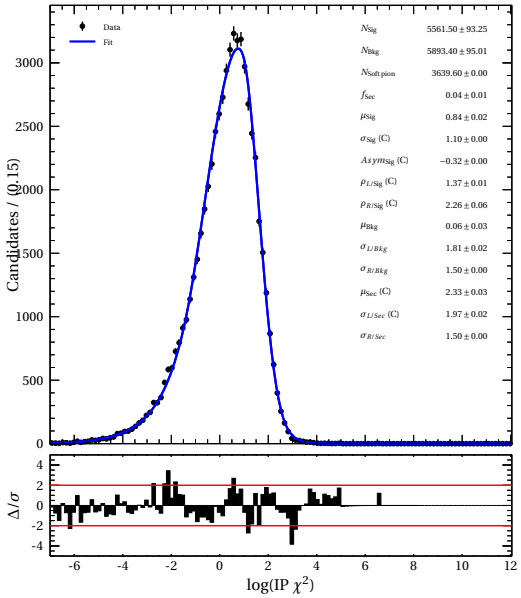

(b) D^0 impact parameter χ^2 prompt prefit

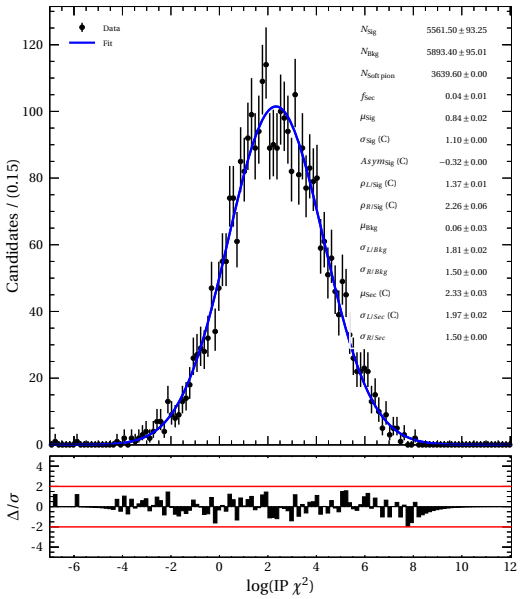

(c) D^0 impact parameter χ^2 secondary prefit

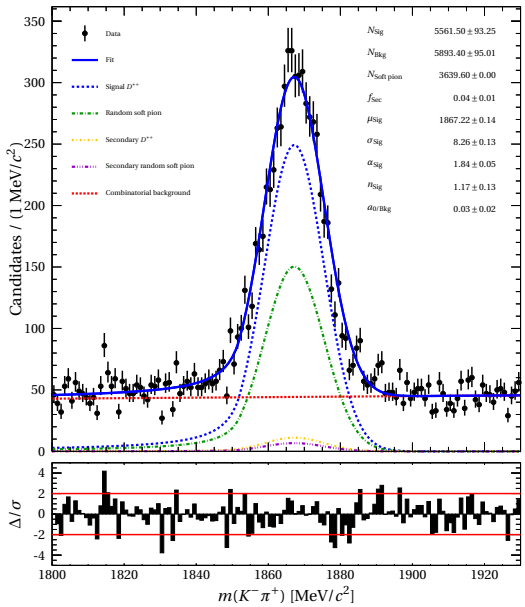

(d) $m\left(K^-\pi^+\right)$ fit

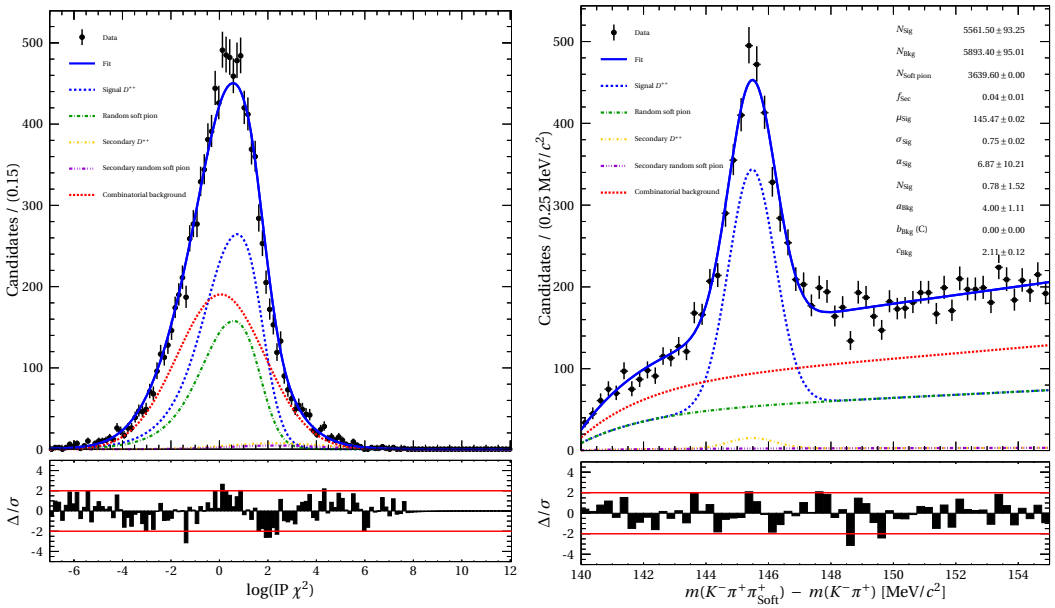

(e) D^0 impact parameter χ^2 fit

(f) $m\left(K^-\pi^+\pi^+\right) - m\left(K^-\pi^+\right)$ fit

Figure 6.1.1: Each stage of the fitting procedure for $D^{*+} \to \left(D^0 \to K^-\pi^+\right)\pi^+$ in the 2011 `MagDown` dataset.

6.2 Yield tables[1]

p_{T}[MeV/c]	y [2,2.5[	[2.5,3[	[3,3.5[	[3.5,4[	[4,4.5[
[0,1000[	330.9 ± 22.6	823.8 ± 34.8	733.0 ± 33.1	408.9 ± 25.7	91.8 ± 12.4
[1000,2000[	720.1 ± 29.8	1803.5 ± 48.0	1600.8 ± 46.0	1041.6 ± 37.7	276.1 ± 19.5
[2000,3000[	765.7 ± 29.7	1763.7 ± 47.2	1564.2 ± 45.2	1012.7 ± 36.3	287.0 ± 19.0
[3000,4000[	619.9 ± 26.6	1176.5 ± 38.0	1087.4 ± 36.4	663.9 ± 28.1	112.2 ± 11.8
[4000,5000[	373.5 ± 20.6	636.5 ± 27.5	565.2 ± 25.7	302.0 ± 18.6	25.3 ± 5.4
[5000,6000[	252.5 ± 16.9	322.4 ± 19.4	265.2 ± 17.4	127.7 ± 12.0	3.0 ± 1.7
[6000,7000[	163.7 ± 13.7	174.8 ± 14.4	141.0 ± 12.6	31.2 ± 6.2	0.0 ± 0.0
[7000,8000[	75.4 ± 9.6	117.7 ± 11.4	70.5 ± 9.0	7.0 ± 3.0	0.0 ± 0.0

Table 6.2.1: Raw signal yields extracted using a 2 dimensional fit for $D^0 \to K^-\pi^+$ decays.

[1] Here right half-open interval notation is used such that $p_T \in [0,1000[$ and $0 < p_T < 1000$ are equivalent.

p_T[MeV/c]	y [2,2.5[	[2.5,3[	[3,3.5[	[3.5,4[	[4,4.5[
[0,1000[	0.0 ± 0.0	0.0 ± 0.0	0.0 ± 0.0	0.0 ± 0.0	0.0 ± 0.0
[1000,2000[	0.0 ± 0.0	6.4 ± 3.1	5.4 ± 2.9	2.0 ± 1.6	0.0 ± 0.0
[2000,3000[	4.3 ± 1.9	34.8 ± 6.3	40.8 ± 7.0	15.7 ± 4.0	4.3 ± 2.2
[3000,4000[	9.6 ± 3.0	63.5 ± 8.4	52.2 ± 8.0	42.0 ± 7.2	2.9 ± 2.0
[4000,5000[	10.0 ± 3.0	54.8 ± 7.4	57.7 ± 8.7	33.5 ± 5.8	5.5 ± 2.8
[5000,6000[	9.6 ± 3.0	44.8 ± 7.0	35.1 ± 6.3	24.7 ± 5.3	3.4 ± 1.8
[6000,7000[	12.5 ± 3.6	28.5 ± 5.6	20.9 ± 4.6	15.9 ± 4.2	0.0 ± 0.0
[7000,8000[	11.9 ± 3.2	15.4 ± 4.1	13.9 ± 3.8	5.5 ± 2.7	0.0 ± 0.0

Table 6.2.2: Raw signal yields extracted using a 2 dimensional fit for $D^0 \to K^-\pi^+\pi^-\pi^+$ decays.

p_T[MeV/c]	y [2,2.5[	[2.5,3[	[3,3.5[	[3.5,4[	[4,4.5[
[0,1000[	0.0 ± 0.0	0.0 ± 0.0	22.7 ± 10.2	17.8 ± 9.0	4.0 ± 3.5
[1000,2000[	0.0 ± 0.0	28.0 ± 7.2	134.2 ± 16.6	95.8 ± 14.9	22.1 ± 7.3
[2000,3000[	5.9 ± 2.7	124.7 ± 12.7	254.6 ± 18.6	185.2 ± 16.7	43.4 ± 8.1
[3000,4000[	18.2 ± 4.7	138.5 ± 12.8	219.7 ± 16.3	111.4 ± 12.5	32.8 ± 6.3
[4000,5000[	25.6 ± 5.4	121.8 ± 11.6	122.3 ± 12.0	56.4 ± 8.3	7.0 ± 2.9
[5000,6000[	24.7 ± 5.2	67.0 ± 8.5	75.7 ± 9.1	38.4 ± 6.6	2.3 ± 1.6
[6000,7000[	13.4 ± 3.9	43.1 ± 6.8	38.6 ± 6.5	10.9 ± 3.7	0.0 ± 0.0
[7000,8000[	8.3 ± 3.0	33.5 ± 5.9	13.8 ± 3.9	5.9 ± 2.5	0.0 ± 0.0

Table 6.2.3: Raw signal yields extracted using a 3 dimensional fit for $D^{*+} \to \left(D^0 \to K^-\pi^+\right)\pi^+$ decays.

p_T[MeV/c]	y [2,2.5[	[2.5,3[	[3,3.5[	[3.5,4[	[4,4.5[
[0,1000[	0.0 ± 0.0	1.4 ± 1.7	0.0 ± 0.0	2.7 ± 2.2	0.0 ± 0.0
[1000,2000[	0.0 ± 0.0	21.7 ± 5.5	23.3 ± 6.0	13.5 ± 4.1	3.1 ± 1.9
[2000,3000[	15.0 ± 4.0	63.2 ± 8.9	60.3 ± 9.0	32.9 ± 6.7	5.8 ± 2.4
[3000,4000[	19.8 ± 4.6	60.3 ± 8.7	72.9 ± 9.6	24.2 ± 5.9	9.7 ± 3.2
[4000,5000[	18.7 ± 5.0	44.1 ± 7.6	47.6 ± 7.5	11.1 ± 3.7	1.9 ± 1.4
[5000,6000[	8.8 ± 3.3	15.4 ± 4.5	27.8 ± 5.5	12.1 ± 3.8	0.0 ± 0.0
[6000,7000[	11.8 ± 3.5	10.5 ± 3.7	14.6 ± 4.5	4.1 ± 2.6	0.0 ± 0.0
[7000,8000[	5.1 ± 2.7	2.8 ± 2.2	10.2 ± 3.4	1.5 ± 1.7	0.0 ± 0.0

Table 6.2.4: Raw signal yields extracted using a 2 dimensional fit for $D^+ \to K^-K^+\pi^+$ decays.

p_{T}[MeV/c]	y [2,2.5[	[2.5,3[	[3,3.5[	[3.5,4[	[4,4.5[
[0,1000[	6.1 ± 0.2	154.6 ± 1.3	274.8 ± 1.8	204.5 ± 1.6	56.1 ± 0.9
[1000,2000[	58.8 ± 0.7	602.9 ± 2.4	901.2 ± 3.1	646.5 ± 2.7	173.3 ± 1.3
[2000,3000[	174.0 ± 1.2	855.0 ± 2.8	1123.9 ± 3.3	689.5 ± 2.7	200.1 ± 1.4
[3000,4000[	224.5 ± 1.4	762.1 ± 2.6	842.3 ± 2.8	474.9 ± 2.1	116.7 ± 1.1
[4000,5000[	158.6 ± 1.2	505.9 ± 2.1	479.4 ± 2.1	294.6 ± 1.7	63.3 ± 0.8
[5000,6000[	130.6 ± 1.1	285.9 ± 1.6	253.2 ± 1.5	140.5 ± 1.1	12.6 ± 0.3
[6000,7000[	79.8 ± 0.8	173.6 ± 1.2	121.5 ± 1.0	54.8 ± 0.7	3.7 ± 0.2
[7000,8000[	43.6 ± 0.6	92.6 ± 0.9	79.7 ± 0.8	26.2 ± 0.5	0.0 ± 0.0

Table 6.2.5: Raw signal yields extracted using a 2 dimensional fit for $D^+ \to K^-\pi^+\pi^+$ decays.

p_{T}[MeV/c]	y [2,2.5[	[2.5,3[	[3,3.5[	[3.5,4[	[4,4.5[
[0,1000[	0.0 ± 0.0	2.4 ± 2.0	4.9 ± 3.2	0.0 ± 0.0	1.3 ± 1.3
[1000,2000[	5.9 ± 2.3	17.8 ± 4.5	25.7 ± 5.5	12.3 ± 4.1	0.0 ± 0.0
[2000,3000[	7.7 ± 2.7	46.7 ± 6.9	47.5 ± 7.1	35.7 ± 6.3	6.7 ± 2.6
[3000,4000[	23.1 ± 4.7	47.2 ± 6.8	73.5 ± 8.5	26.0 ± 5.2	8.3 ± 2.9
[4000,5000[	18.7 ± 4.2	25.5 ± 5.0	33.3 ± 5.8	10.1 ± 3.4	4.1 ± 2.5
[5000,6000[	9.1 ± 2.9	18.5 ± 4.3	13.7 ± 3.7	10.4 ± 3.3	0.0 ± 0.0
[6000,7000[	7.8 ± 2.8	12.1 ± 3.4	14.9 ± 3.8	3.3 ± 1.8	0.0 ± 0.0
[7000,8000[	9.4 ± 2.9	7.7 ± 2.7	6.0 ± 2.9	4.1 ± 2.1	0.0 ± 0.0

Table 6.2.6: Raw signal yields extracted using a 2 dimensional fit for $D_s^+ \to (\phi \to K^-K^+)\pi^+$ decays.

p_{T}[MeV/c]	y [2,4.5[
[2000,3000[	102.5 ± 15.2
[3000,4000[	150.3 ± 18.0
[4000,5000[	110.3 ± 15.1
[5000,6000[	58.8 ± 11.0
[6000,7000[	21.2 ± 7.5
[7000,8000[	12.4 ± 5.5

Table 6.2.7: Raw signal yields extracted using a 2 dimensional fit for $\Lambda_c^+ \to pK^-\pi^+$ decays.

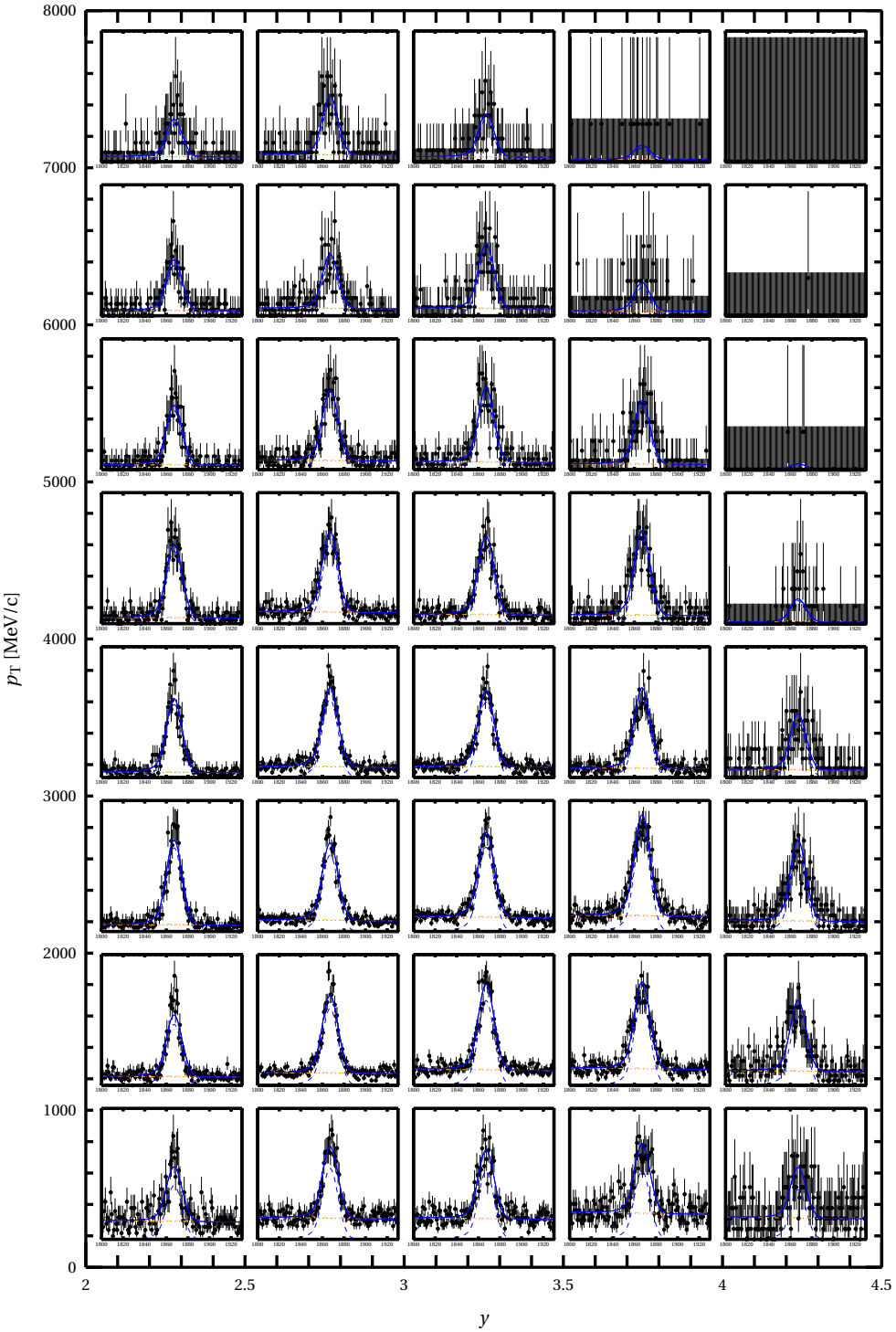

Figure 6.3.1: Fitted distribution of $m\left(K^-\pi^+\right)$ in $D^0 \to K^-\pi^+$

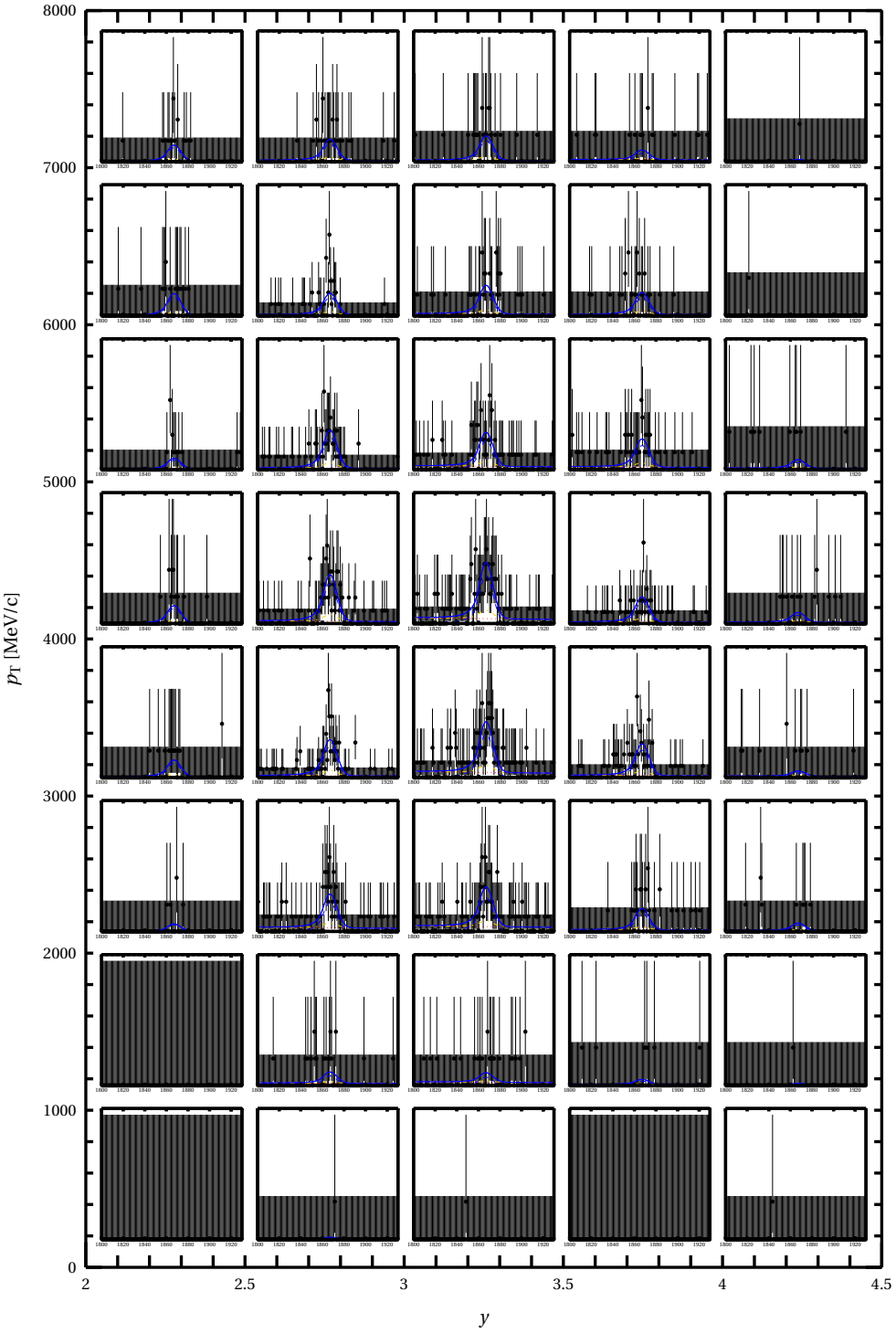

Figure 6.3.2: Fitted distribution of $m\left(K^-\pi^+\right)$ in $D^0 \to K^-\pi^+\pi^-\pi^+$

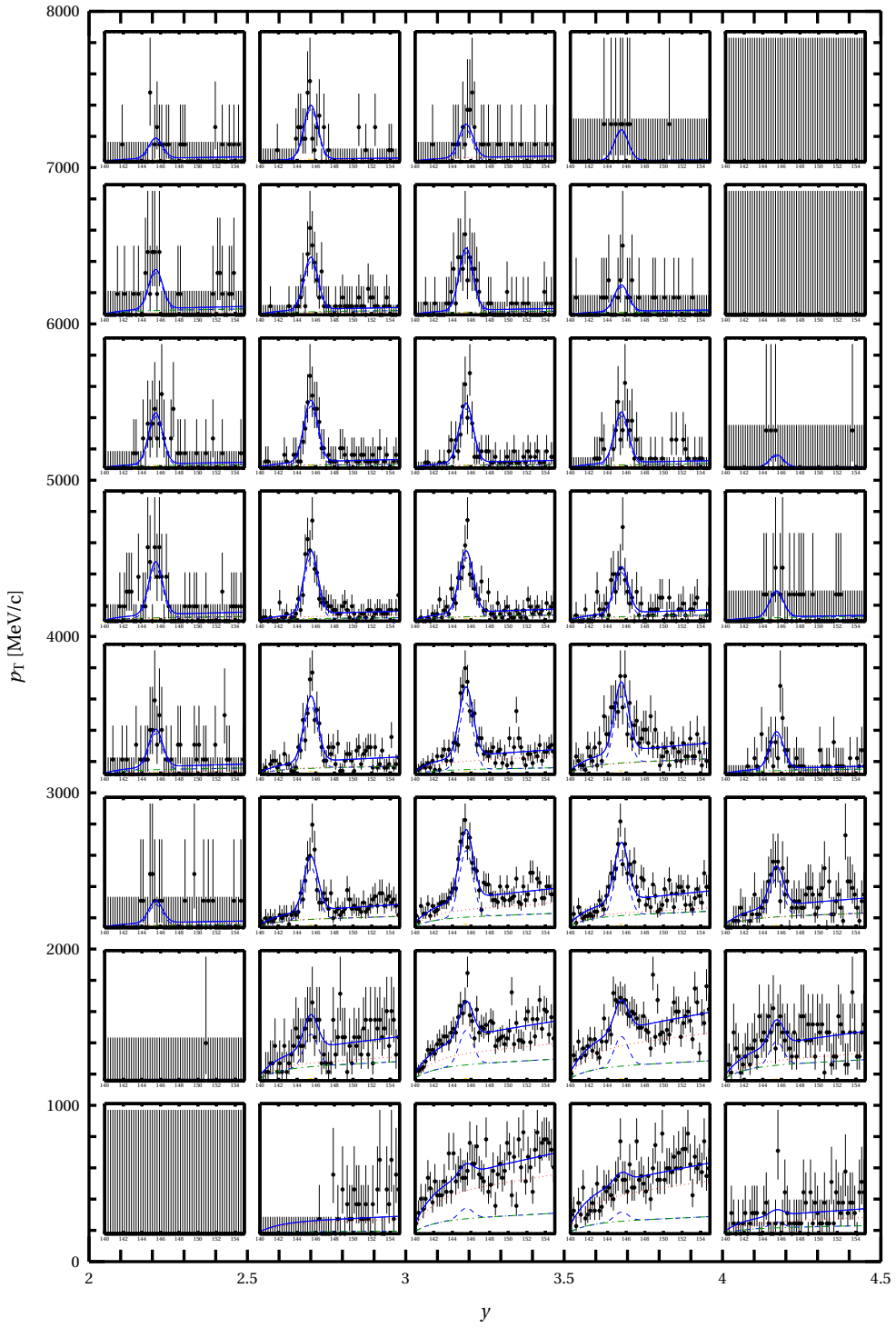

Figure 6.3.3: Fitted distribution of $m\left(K^-\pi^+\pi^+\right) - m\left(K^-\pi^+\right)$ in $D^{*+} \to \left(D^0 \to K^-\pi^+\right)\pi^+$

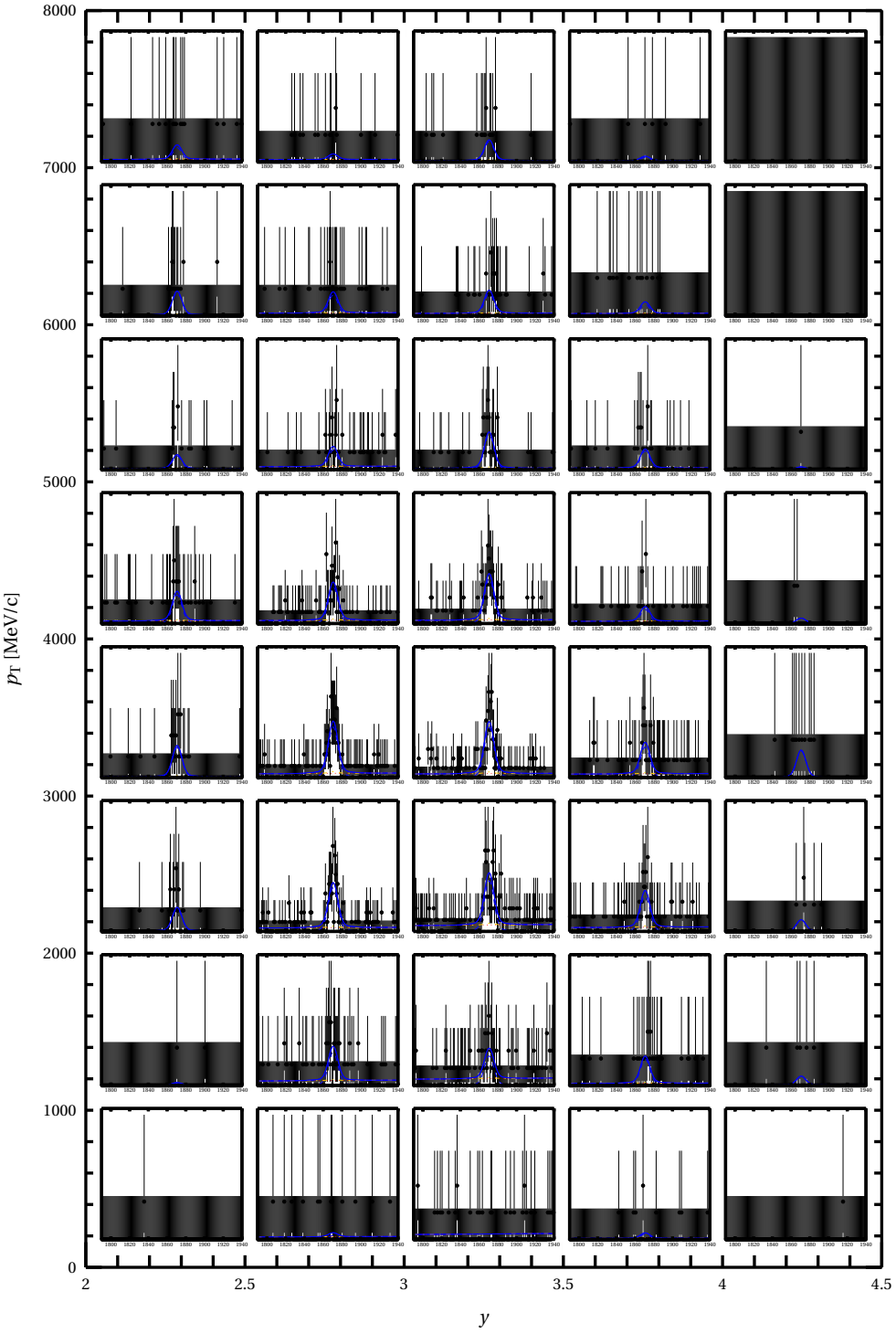

Figure 6.3.4: Fitted distribution of $m\left(K^-\pi^+\pi^+\right)$ in $D^+ \to K^-K^+\pi^+$

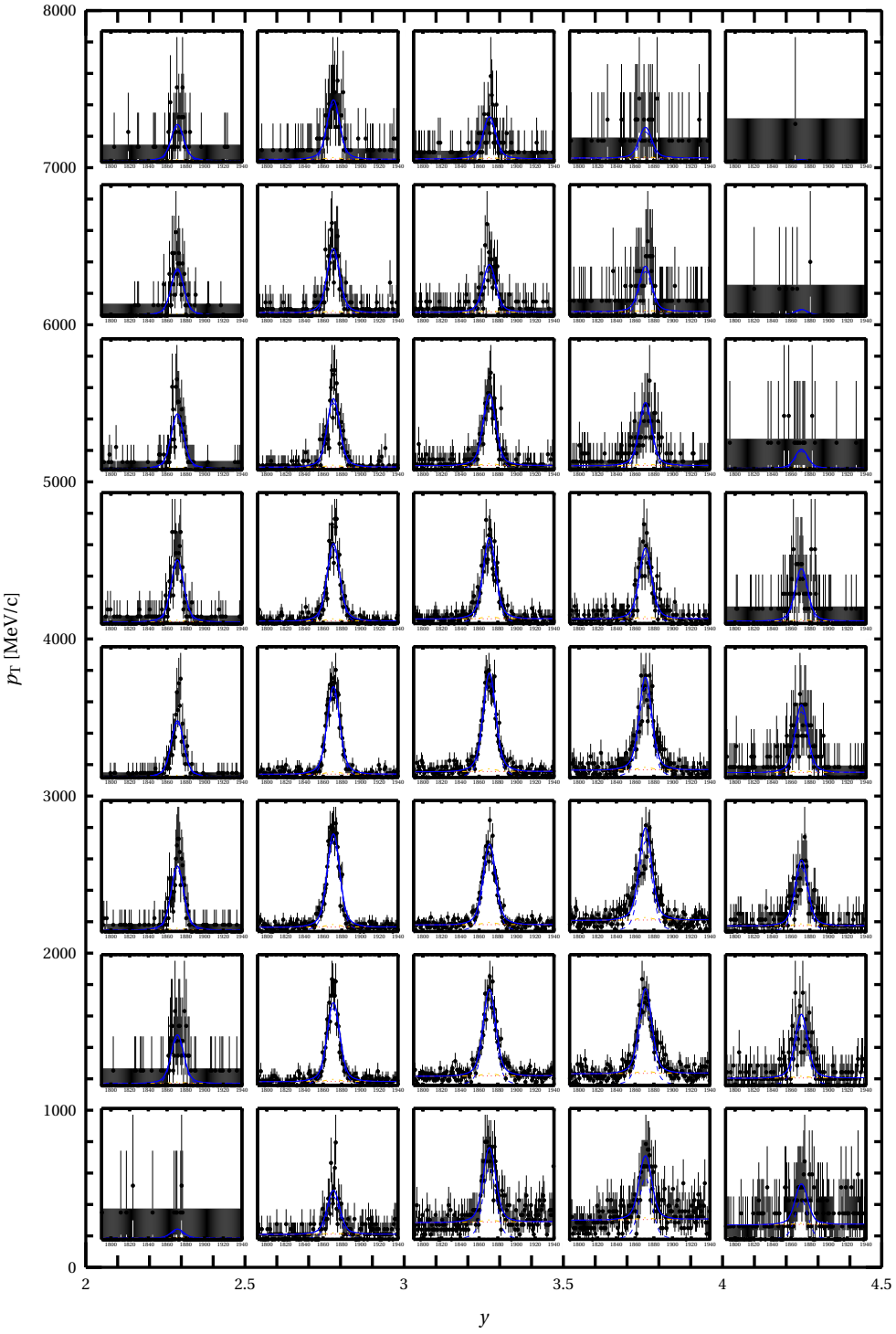

Figure 6.3.5: Fitted distribution of $m\left(K^-K^+\pi^+\right)$ in $D^+ \to K^-\pi^+\pi^+$

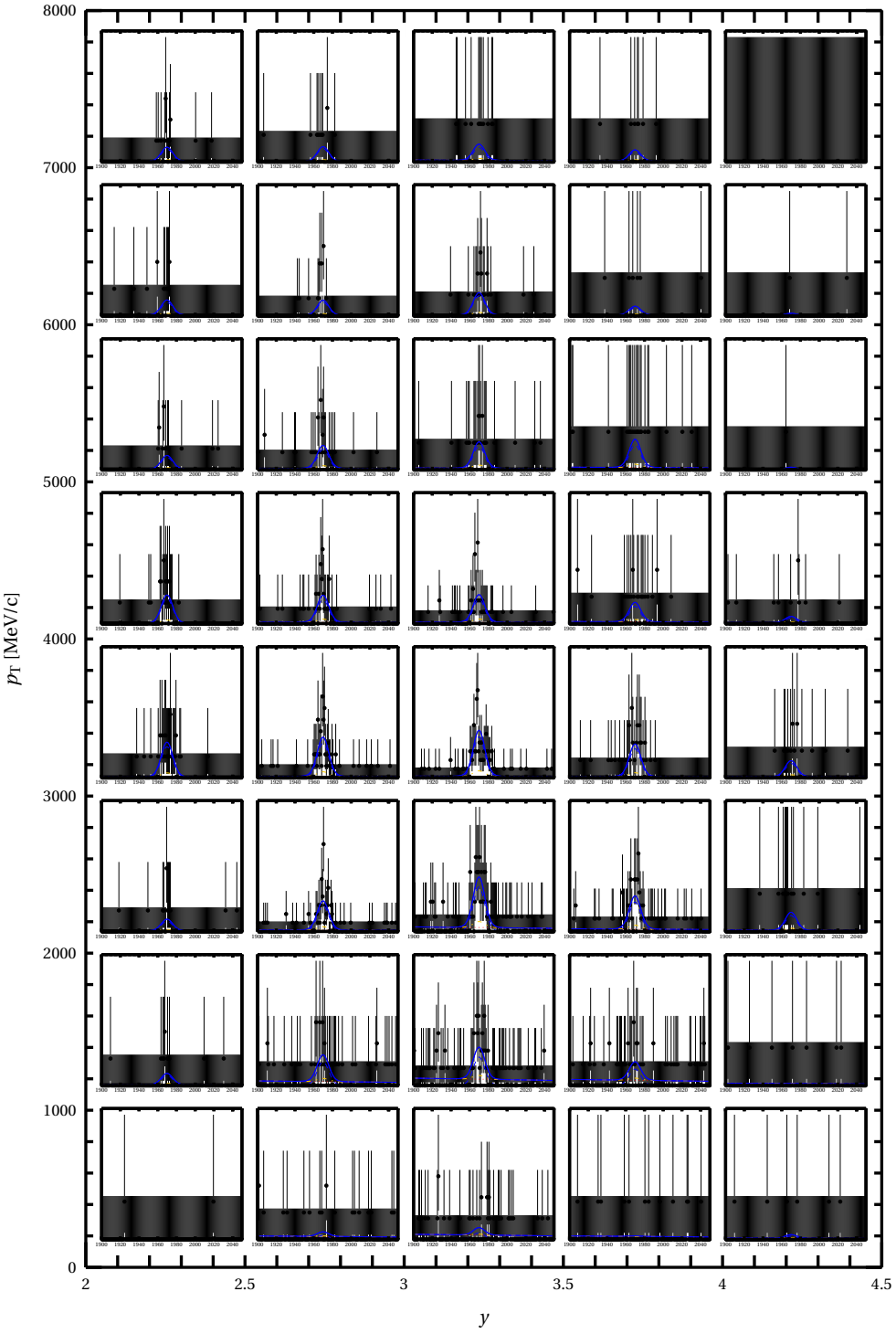

Figure 6.3.6: Fitted distribution of $m\left(K^-K^+\pi^+\right)$ in $D_s^+ \to \left(\phi \to K^-K^+\right)\pi^+$

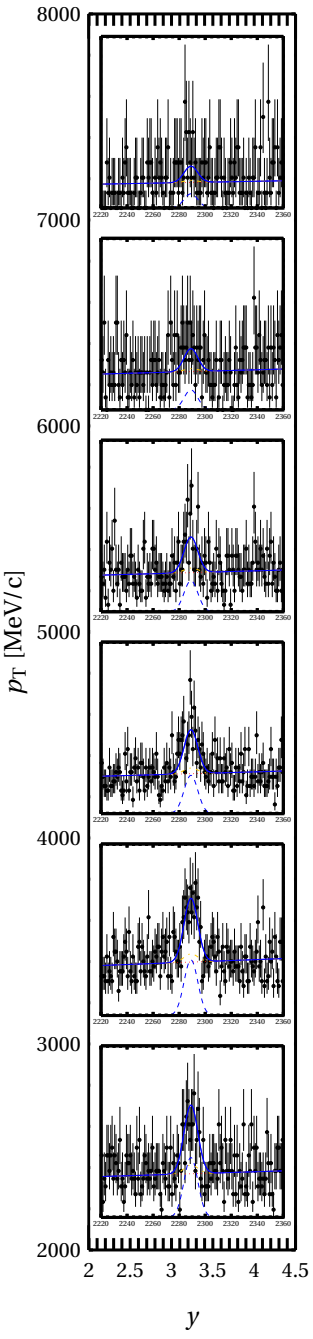

Figure 6.3.7: Fitted distribution of $m\left(pK^-\pi^+\right)$ in $\Lambda_c^+ \to pK^-\pi^+$

7 Efficiencies

The absolute efficiency by which candidates are obtained is comprised of several components as listed in Equation 7.1 where, for simplicity, the notation stating that each efficiency is dependent on those prior to it has been dropped. With exception of the PID efficiency, described in Section 7.4, each of these components are evaluated by applying each stage of the analysis to events which have been simulated using the production system provided by LHCb and summarised in Section 2.4.

$$\epsilon_{\text{Total}} = \epsilon_{\text{Acceptance}} \times \epsilon_{\text{Reconstruction}} \times \epsilon_{\text{Preselection}} \times \epsilon_{\text{BDT}} \times \epsilon_{\text{PID}} \tag{7.1}$$

7.1 Detector acceptance

$$\epsilon_{\text{Acceptance}} = \frac{N_{\texttt{DaughtersInLHCb}|\text{Generated}}}{N_{\text{Generated}}} \tag{7.2}$$

To reduce the computing resource overhead of the production of simulated events, a selection is applied after producing Monte Carlo particles but prior to simulating the effects of the detector. This is known as `DaughtersInLHCb` cut and requires all tracks of the decay that is being simulated to be within the pseudorapidity range $2 < \eta < 5$. While a counter of the number of events passing and failing this cut is kept, allowing the efficiency of be known, it is unsuitable for this measurement as this only shows the efficiency between the integrated LHCb acceptance and the 4π solid angle. Instead specialised production must be used to obtain the efficiency given by Equation 7.2.

7.2 Reconstruction

$$\epsilon_{\text{Reconstruction}} = \frac{N_{\text{Reconstructed}|\texttt{DaughtersInLHCb}}}{N_{\texttt{DaughtersInLHCb}|\text{Generated}}} \tag{7.3}$$

The reconstruction efficiency is a single value representing two separate efficiencies. One is the due to the imperfect nature of the detector elements resulting in not all tracks producing hits in the detector. This modelled by a description of the detector being used by GEANT4 to simulate the material interactions that cause this inefficiency. The

other component is due to the time constraints when executing the reconstruction algorithm necessitating the use of approximations and pattern recognition instead of comparing all possible combinations of detector hits. This effect is simulated by applying the reconstruction to the simulated detector hits, however, it is known that the efficiencies produced by this process are not representative of real data. As a result the LHCb collaboration's tracking group provides a series tables that give the ratio of the true efficiency to the simulated efficiency as a function of track kinematics and various detector properties, such as the number of hits in any particular sub-detector. These have been combined to a give a single table of ratios in Figure 7.2.1 which represent the individual track corrections, $\rho_{\text{Tracking},\,i}$. To obtain a total correction for a particular bin the correction for each event, ρ_{Tracking}, must be calculated using Equation 7.4. Tables of the tracking correction for each decay channel are available in Appendix C.

$$\epsilon_{\text{Tracking correction}} = \prod_{\text{events}} \rho_{\text{Tracking}} = \prod_{\text{events}} \left(\prod_{\text{tracks}} \rho_{\text{Tracking},\,i} \right) \tag{7.4}$$

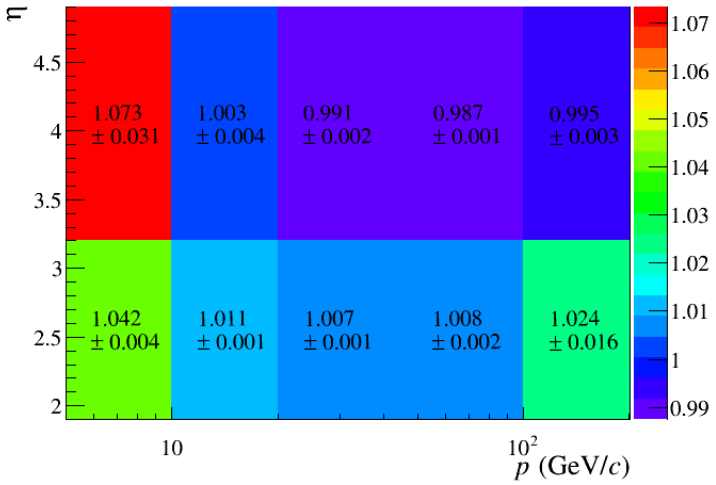

Figure 7.2.1: Table of the combined ratios for the tracking efficiency corrections in bins of transverse momentum and rapidity taken from Reference [36].

7.3 Selection

$$\epsilon_{\text{Preselection}} = \frac{N_{\text{Preselected|Reconstructed}}}{N_{\text{Reconstructed|DaughtersInLHCb}}} \qquad \epsilon_{\text{BDT}} = \frac{N_{\text{BDT|Preselected}}}{N_{\text{Preselected|Reconstructed}}} \tag{7.5}$$

The selection efficiency, excluding PID cuts, is separated into two components, given by Equation 7.5 and each of these components are found by applying the selection to the previously accepted Monte Carlo events from the reconstruction and the preselection respectively. These stages of the efficiency chain assume the simulation

accurately describes the real data and the validity of this assumption is discussed in Section 10.

7.4 Particle Identification

For the calculation of the efficiency of particle identification cuts, it is known that the efficiencies obtained from simulated events are unphysical when compared to real data and, as a result, a more data driven technique must be used. The method used in this analysis requires samples of the final state particles to be obtained from real data. These samples must have a very high signal purity and, in addition, their selection cannot use any variable which is derived from the particle identification system. Fortunately the particle ID group of the LHCb collaboration provides calibration samples of pions and kaons that have been selected from decays of D^{*+} mesons and of protons from decays of Λ baryons, from which efficiencies can be derived by applying the PID cuts used for this analysis. This process is further complicated by the efficiency of PID cuts being dependent upon the momentum and pseudorapidity of the given track, and the occupancy[1] of the detector as a whole. As a result, a weighting procedure must be employed to find the efficiency of the cuts when applied to tracks with differing distributions in these variables.

In order to reweight the calibration samples into the distribution of the studied process a binning scheme must be employed. Ideally each bin should be small to prevent any efficiency variation across the bin, however, this is not possible due to the finite nature of the calibration samples introducing statistical uncertainty in the efficiency of any applied cut in that bin. The binning schemes used for kaons and pions are respectively shown in Figure 7.4.1 and 7.4.2 and are optimised to balance the two contradicting effects using the following algorithm for each dependent variable:

1. Find the integrated efficiency across the entire variable range.

2. Subdivide every bin into 10 smaller bins with equal population, or equivalently equal statistical uncertainty, and perform a χ^2 test between the efficiency of smaller bins and the larger bin. Any bin with a summed result of less than 0.001 is further subdivided.

3. If the bin is to be divided, calculate the χ^2 between the integrated bin and the efficiency of 20 equal population bins. Then split the bin at the boundary which minimises the sum of these χ^2 values provided both new bins contain at least 2000 events.

[1] Occupancy refers to the number of tracks that are present in the detector for any given event and is henceforth referred to as `nTracks`.

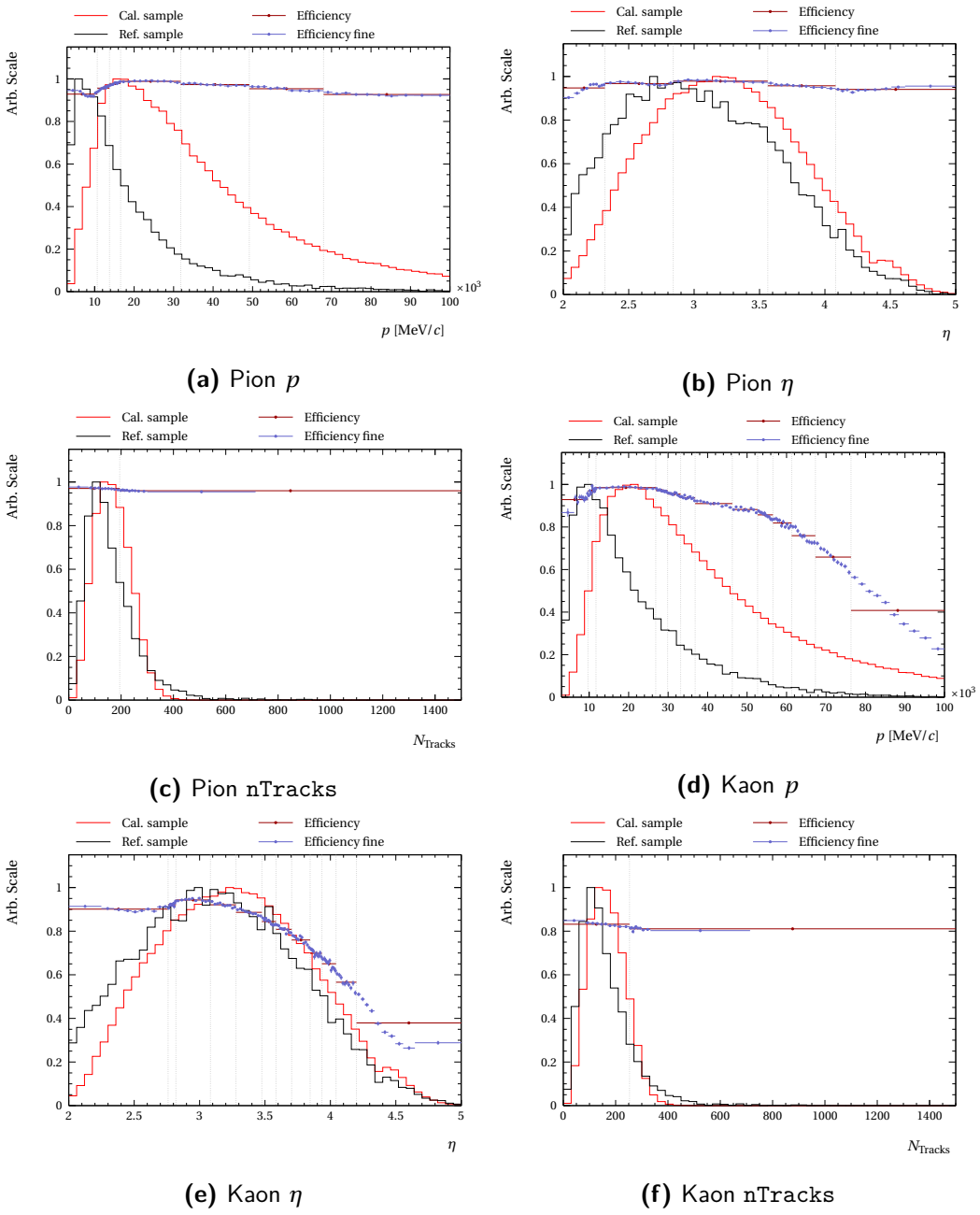

(a) Pion p **(b)** Pion η

(c) Pion `nTracks` **(d)** Kaon p

(e) Kaon η **(f)** Kaon `nTracks`

Figure 7.4.1: Plots showing the binning scheme and dependence of the PID efficiency on momentum, pseudorapidity and `nTracks` for pions and kaons in the PID calibration sample, with the distributions present in $D^0 \to K^-\pi^+$ shown for reference.

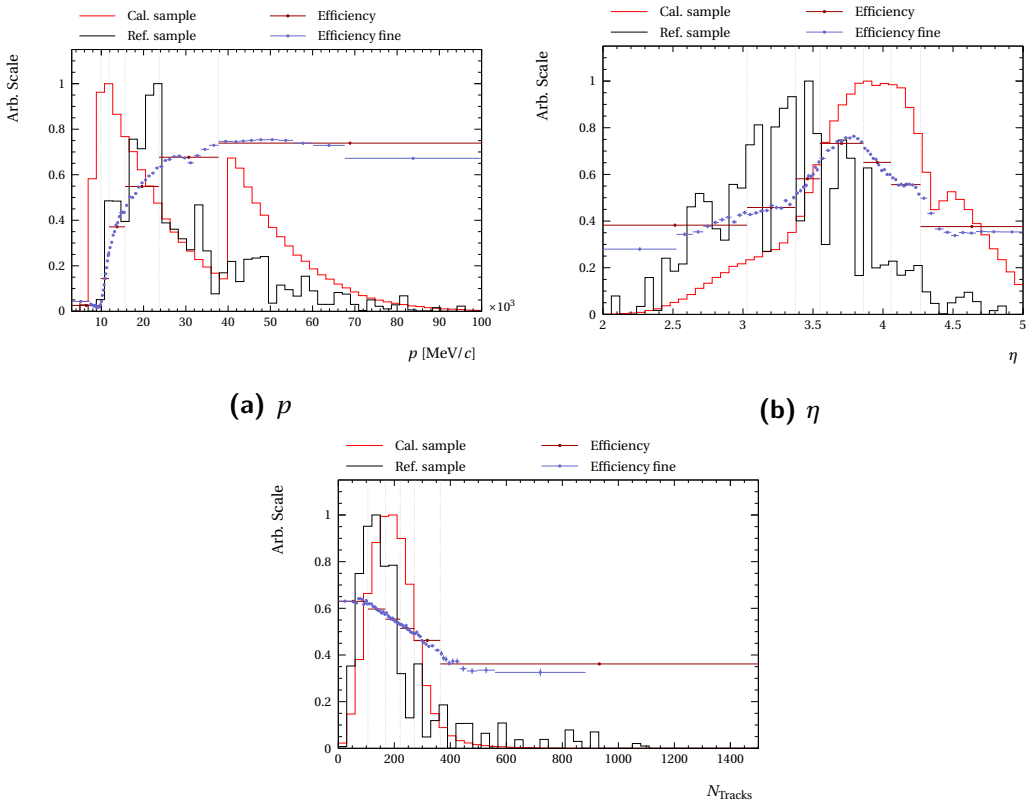

(a) p **(b)** η

(c) `nTracks`

Figure 7.4.2: Plots showing the binning scheme and dependence of the PID efficiency on momentum, pseudorapidity and `nTracks` for protons in the PID calibration sample, with the distributions present in $\Lambda_c^+ \to pK^-\pi^+$ shown for reference.

4. Repeat steps 2 and 3 until all bins either pass the χ^2 test or there exists no valid subdivision due to the minimum required number of events.

5. Finally if the efficiency of neighbouring bins agrees to within 3σ of the statistical error on each bin, merge them.

The three one dimensional binning schemes produced are then combined to produce a single three dimensional binning scheme in `nTracks`, p and η. A concern for generating the bin boundaries in this method is that any correlations that may affect the optimal choice are ignored, however, despite the variables being strongly correlated across the full ranges the correlation within a single bin produced with this method is negligible.

The other requirement to perform the weighting procedure is to obtain a reference sample with representative distributions for dependent variables of the PID cut. In contrast to the BDT training samples it was decided to use `sWeights` produced from the final fit as the detector occupancy is known to be poorly described in the simulation.

To calculate the total efficiency of a specified PID cut the efficiency of each reweighed bin must be known and is given by Equation 7.6 where C_i is the total number of candidates in a calibration bin, i and C_i' is the number of candidates passing the specified PID cut.

$$\epsilon_{\mathrm{i}} = \frac{C_i'}{C_i} \tag{7.6}$$

In addition a weight must be calculated for each bin using Equation 7.7 where a_j is the sWeight of the j^{th} candidate in the i^{th} bin of the reference sample, R is the total number of candidates in the reference sample and C is the total number of events in the calibration sample.

$$\omega_i = \frac{\sum\limits_j a_{ij}}{C_i} \cdot \frac{C}{R} \tag{7.7}$$

All calibration bins can then be summed over, as in Equation 7.8, to give the total efficiency of a PID cut on a single track and these can then be combined, with Equation 7.9, to give the total efficiency for multiple PID cuts.

$$\epsilon_{\mathrm{track}} = \frac{\sum\limits_{i\in\mathrm{bins}} \omega_i C_i \epsilon_i}{\sum\limits_{i\in\mathrm{bins}} \omega_i C_i} = \frac{\sum\limits_{i\in\mathrm{bins}} a_{ij}\epsilon_i}{\sum\limits_{i\in\mathrm{bins}} a_{ij}} = \frac{1}{R}\sum_{i\in\mathrm{bins}} a_{ij}\epsilon_i \tag{7.8}$$

$$\epsilon_{\mathrm{PID}} = \prod_{tracks} \epsilon_{\mathrm{track}} \tag{7.9}$$

Currently the method outlined here produces regions with unphysically large statistical errors in some regions, particularly for modes with low yields such as $D^+ \to K^-K^+\pi^+$. This effect is believed to be a result of the `sPlot` procure producing regions with negative weights and is currently under investigation.

7.5 Efficiency tables

See Appendix E

8

Statistical uncertainties

Statistical uncertainty arises from the desire to measure the true value of any given quantity using a finite sized dataset. This differs from the systematic uncertainties discussed in Chapter 10 which are typically defined as being errors which cannot be reduced through the use of a enlarged dataset.[1] This section describes the method used to calculate the statistical uncertainties that have been given in Chapter 6 and 7.

8.1 Binomial uncertainty

When calculating the acceptance, reconstruction and selection efficiencies (with exception of PID which is independently discussed in Section 7.4) each simulated candidate has two possible outcomes, it can pass or fail the selection, and as such, these can be thought of as a Bernoulli trial. When multiple Bernoulli trials are performed, a binomial distribution, Equation 8.1, arises where $f\left(k\right)$ is the probability of observing k events from n trials if the probability of any individual event passing is p.

$$f\left(k;n,p\right)=\binom{n}{k}p^{k}\left(1-p\right)^{n-k} \tag{8.1}$$

While this provides an accurate description of the distribution of $f\left(k\right)$ the distribution of interest is actually $f\left(p\right)$ given k passes have been observed from n trials. In the limit of large n this can be approximated by the normal distribution, however, in the case of large numbers of events, high efficiencies or low efficiencies this approximation yields unphysical uncertainties. Various alternative methods for the calculation of confidence intervals exist, such as Wilson or Clopper-Pearson intervals, however, for these measurements Agresti-Coull[37] intervals are used.

[1] While this is typically the case, many systematics can often be studied in greater detail through the addition of more data or are dependent upon other data taken alongside the main dataset, such as the PID calibration samples.

8.2 Tracking efficiency correction

The statistical error of the tracking efficiency correction on a single track is provided by the LHCb tracking efficiency group. These can then be propagated using Gaussian error propagation as show in Equation 8.2 where a is the total number of tracks and a_i is the number of tracks in a bin, i.

$$\Delta\epsilon_{\text{tracking, stat}} = \sum_{p\in n} \frac{a_i^2}{a^2} \left(\Delta\epsilon_i\right)^2 \tag{8.2}$$

8.3 Fit yield

The fitting procedure is performed by `RooFit` which is in turn based upon `MINUIT`. The statistical error is calculated by `MINUIT` using the techniques described in Reference [38].

8.4 Particle ID

The calculation of the statistical error of the particle identification cuts starts with the calculation of the binomial uncertainty of the efficiency in each bin of the calibration sample, $\Delta\epsilon_{f(e)}$, using the procedure described in Section 8.1. These can then be propagated using Gaussian error propagation to give the total error on a hadron with n PID cuts applied.

$$\Delta\epsilon_e = \epsilon_e \sqrt{\sum_{p\in n}\sum_{k\in n} \delta_{pk} \cdot \frac{\Delta\epsilon_{f_p(e)}}{\epsilon_{f_p(e)}} \cdot \frac{\Delta\epsilon_{f_k(e)}}{\epsilon_{f_k(e)}}} \tag{8.3}$$

As the efficiency is fully correlated in the case of multiple PID cuts being applied to tracks of the same species that fall in the same calibration bin the Kronecker delta, δ_{pk}, is used to account for these correlations. The per bin errors can then be combined to give the total error using the estimated error on the sample mean with Bessel's correction applied as given in Equation 8.4.

$$\Delta\epsilon_{\text{PID, stat}} = \sqrt{\frac{1}{R\left(R-1\right)} \sum_{e\in\text{events}} \left(\epsilon_e - \epsilon\right)^2 a_e} \tag{8.4}$$

9 Results

In this chapter the currently available results are presented in the follow forms:

Normalised cross-section ratio

Here each result is normalised to the specified region to show the variation of the cross-section across transverse momentum and rapidity. The errors are stated in the form $n \pm stat \pm sys$ where n is the nominal value, $stat$ is the combination of the statistical errors listed in Chapter 8 combined using Gaussian error propagation and sys is the systematic error from the finite size of the PID calibration sample, calculated using the technique described in Section 10.

Deviation from the previous LHCb measurement

For comparisons to be made between the previous LHCb result the analysis performed here, the previous LHCb result must first be normalised. As the dominant source of systematic uncertainty in the previous measurement arose from the luminosity measurement, which can be reasonably assumed to be correlated between all parts of the previous measurement, only the statistical uncertainty was considered when propagating the errors through the normalisation. The ratio $\frac{\sigma_{2011,\,\mathrm{norm}}}{\sigma_{2010,\,\mathrm{norm}}}$ is then calculated. As the expectation value of this ratio is 1 the tables presented here are in units of the standard deviation, as defined in Equation 9.1 where $\mathscr{R}$ is the ratio in the given bin with an error $\Delta\mathscr{R}$.

$$\left|\frac{1-\mathscr{R}}{\Delta\mathscr{R}}\right| \tag{9.1}$$

Deviation from the theory

For D^0, $D^{*+}$and $D^+$the obtained result is compared to theoretical prediction from the `FONLL` model. The method of obtaining the prediction is described in Appendix B. As with the comparison to the previous LHCb result, the comparison is presented in units of standard deviation with the exception that all errors in the prediction are assumed to be uncorrelated across the whole p_T-y space.

These show a significant deviation from previous results in the upper and lower rapidity regions and the cause of this deviation is currently unknown. One cause that has been considered is the particle identification efficiency producing unrealistic efficiencies as mentioned in Section 7.4, however, this efficiency is too high to account for the observed discrepancy. Another possible cause is the reconstruction efficiency which shows significant degradation in the effected region and studies into this effect are ongoing.

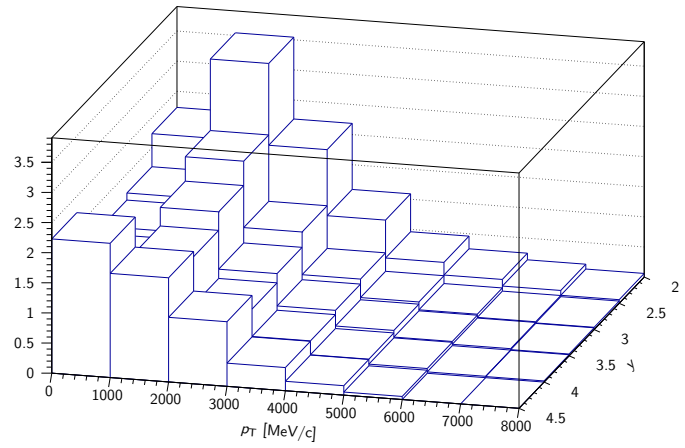

Figure 9.0.1: Plot of the D^0 cross-section normalised to the measured result for $2\,\text{GeV} < p_T < 3\,\text{GeV}$ and $3.0 < y < 3.5$ from $D^0 \to K^-\pi^+$ decays. Any regions with a greater than 100 % statistical error have been removed.

	[2.0, 2.5[	[2.5, 3.0[	[3.0, 3.5[	[3.5, 4.0[	[4.0, 4.5[
[0.0, 1000.0[	$2.23 \pm 0.18 \pm 0.42$	$1.68 \pm 0.10 \pm 0.34$	$1.57 \pm 0.09 \pm 0.30$	$1.44 \pm 0.11 \pm 0.27$	$2.23 \pm 0.34 \pm 0.42$
[1000.0, 2000.0[	$3.54 \pm 0.20 \pm 0.67$	$2.36 \pm 0.10 \pm 3.01$	$1.95 \pm 0.09 \pm 3.71$	$1.64 \pm 0.08 \pm 0.33$	$1.73 \pm 0.15 \pm 0.33$
[2000.0, 3000.0[	$2.19 \pm 0.12 \pm 0.41$	$1.25 \pm 0.06 \pm 0.28$	-	$0.85 \pm 0.04 \pm 0.36$	$1.07 \pm 0.09 \pm 0.20$
[3000.0, 4000.0[	$1.09 \pm 0.06 \pm 0.21$	$0.55 \pm 0.03 \pm 0.10$	$0.46 \pm 0.02 \pm 0.09$	$0.39 \pm 0.02 \pm 0.08$	$0.38 \pm 0.05 \pm 0.07$
[4000.0, 5000.0[	$0.46 \pm 0.03 \pm 0.09$	$0.24 \pm 0.01 \pm 0.05$	$0.20 \pm 0.01 \pm 0.04$	$0.16 \pm 0.01 \pm 0.03$	$0.16 \pm 0.04 \pm 0.03$
[5000.0, 6000.0[	$0.25 \pm 0.02 \pm 0.05$	$0.11 \pm 0.01 \pm 0.02$	$0.09 \pm 0.01 \pm 0.02$	$0.08 \pm 0.01 \pm 0.01$	$0.05 \pm 0.03 \pm 0.01$
[6000.0, 7000.0[	$0.14 \pm 0.01 \pm 0.03$	$0.06 \pm 0.01 \pm 0.01$	$0.05 \pm 0.00 \pm 0.01$	$0.02 \pm 0.01 \pm 0.00$	-
[7000.0, 8000.0[	$0.06 \pm 0.01 \pm 0.01$	$0.04 \pm 0.00 \pm 0.01$	$0.03 \pm 0.00 \pm 0.01$	$0.02 \pm 0.01 \pm 0.00$	-

Table 9.0.1: Table of the D^0 cross-section normalised to the measured result for $2\,\text{GeV} < p_T < 3\,\text{GeV}$ and $3.0 < y < 3.5$ from $D^0 \to K^-\pi^+$ decays.

	[2.0, 2.5[	[2.5, 3.0[	[3.0, 3.5[	[3.5, 4.0[	[4.0, 4.5[
[0.0, 1000.0[	2.6σ	2.2σ	1.9σ	1.9σ	3.4σ
[1000.0, 2000.0[	5.2σ	1.5σ	0.5σ	0.0σ	2.8σ
[2000.0, 3000.0[	5.9σ	0.7σ	–	0.1σ	4.1σ
[3000.0, 4000.0[	5.6σ	1.0σ	0.2σ	2.0σ	2.6σ
[4000.0, 5000.0[	4.5σ	0.2σ	0.4σ	1.0σ	1.6σ
[5000.0, 6000.0[	4.1σ	1.9σ	0.1σ	0.7σ	0.1σ
[6000.0, 7000.0[	3.4σ	0.8σ	0.3σ	1.8σ	–
[7000.0, 8000.0[	1.9σ	0.3σ	1.5σ	0.2σ	–

Table 9.0.2: Variation in units of the standard deviation between the results presented here and the previous LHCb measurement for the cross-section of D^0 normalised to the measured result in $2\,\text{GeV} < p_T < 3\,\text{GeV}$ and $3.0 < y < 3.5$ from $D^0 \to K^-\pi^+$ decays.

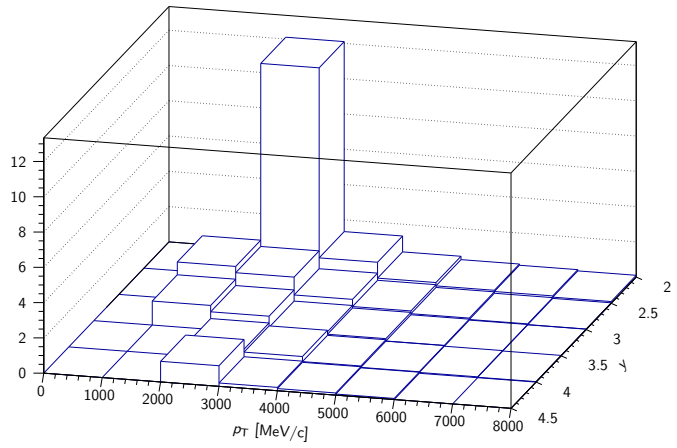

Figure 9.0.2: Plot of the D^0 cross-section normalised to the measured result for $2\,\text{GeV} < p_T < 3\,\text{GeV}$ and $3.0 < y < 3.5$ from $D^0 \to K^-\pi^+\pi^-\pi^+$ decays. Any regions with a greater than 100 % statistical error have been removed.

	[2.0, 2.5[	[2.5, 3.0[	[3.0, 3.5[	[3.5, 4.0[	[4.0, 4.5[
[0.0, 1000.0[	-	-	-	-	-
[1000.0, 2000.0[	-	$2.08 \pm 1.12 \pm 0.01$	$1.36 \pm 0.82 \pm 0.01$	$1.12 \pm 2.20 \pm 0.02$	-
[2000.0, 3000.0[	$12.10 \pm 7.80 \pm 0.05$	$1.73 \pm 0.46 \pm 0.01$	-	$0.62 \pm 0.20 \pm 0.00$	$1.17 \pm 0.69 \pm 0.02$
[3000.0, 4000.0[	$1.33 \pm 0.51 \pm 0.00$	$0.72 \pm 0.16 \pm 0.00$	$0.37 \pm 0.09 \pm 0.00$	$0.45 \pm 0.12 \pm 0.00$	$0.19 \pm 0.14 \pm 0.00$
[4000.0, 5000.0[	$0.43 \pm 0.16 \pm 0.00$	$0.31 \pm 0.07 \pm 0.00$	$0.23 \pm 0.05 \pm 0.00$	$0.16 \pm 0.04 \pm 0.00$	$0.12 \pm 0.07 \pm 0.00$
[5000.0, 6000.0[	$0.24 \pm 0.09 \pm 0.00$	$0.15 \pm 0.04 \pm 0.00$	$0.09 \pm 0.02 \pm 0.00$	$0.08 \pm 0.02 \pm 0.00$	$0.06 \pm 0.04 \pm 0.00$
[6000.0, 7000.0[	$0.17 \pm 0.06 \pm 0.00$	$0.07 \pm 0.02 \pm 0.00$	$0.04 \pm 0.01 \pm 0.00$	$0.05 \pm 0.02 \pm 0.00$	-
[7000.0, 8000.0[	$0.10 \pm 0.03 \pm 0.00$	$0.03 \pm 0.01 \pm 0.00$	$0.02 \pm 0.01 \pm 0.00$	$0.02 \pm 0.01 \pm 0.00$	-

Table 9.0.3: Table of the D^0 cross-section normalised to the measured result for $2\,\text{GeV} < p_T < 3\,\text{GeV}$ and $3.0 < y < 3.5$ from $D^0 \to K^-\pi^+\pi^-\pi^+$ decays.

	[2.0, 2.5[	[2.5, 3.0[	[3.0, 3.5[	[3.5, 4.0[	[4.0, 4.5[
[0.0, 1000.0[	–	–	–	–	–
[1000.0, 2000.0[	–	0.0σ	0.6σ	0.2σ	–
[2000.0, 3000.0[	1.4σ	1.1σ	–	1.1σ	0.8σ
[3000.0, 4000.0[	1.4σ	1.2σ	1.0σ	1.0σ	0.3σ
[4000.0, 5000.0[	1.0σ	1.0σ	0.3σ	0.4σ	0.5σ
[5000.0, 6000.0[	1.1σ	0.6σ	0.0σ	0.5σ	0.3σ
[6000.0, 7000.0[	1.6σ	0.5σ	0.4σ	0.7σ	–
[7000.0, 8000.0[	1.7σ	0.5σ	0.5σ	0.4σ	–

Table 9.0.4: Variation in units of the standard deviation between the results presented here and the previous LHCb measurement for the cross-section of D^0 normalised to the measured result in $2\,\text{GeV} < p_T < 3\,\text{GeV}$ and $3.0 < y < 3.5$ from $D^0 \to K^-\pi^+\pi^-\pi^+$ decays.

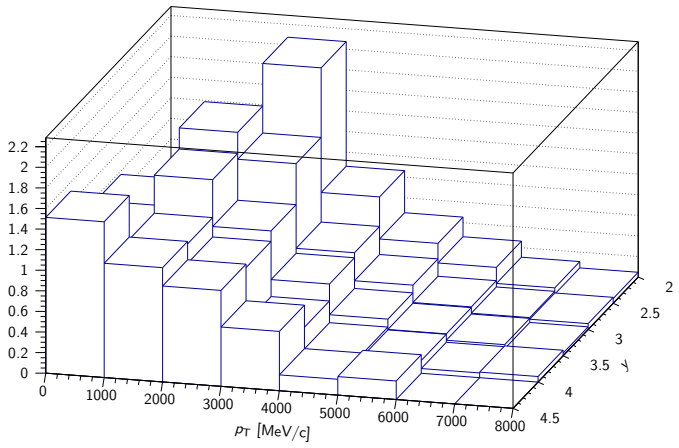

Figure 9.0.3: Plot of the D^{*+} cross-section normalised to the measured result for $2\,\text{GeV} < p_T < 3\,\text{GeV}$ and $3.0 < y < 3.5$ from $D^{*+} \to \left(D^0 \to K^-\pi^+\right)\pi^+$ decays. Any regions with a greater than 100 % statistical error have been removed.

	[2.0, 2.5[	[2.5, 3.0[	[3.0, 3.5[	[3.5, 4.0[	[4.0, 4.5[
[0.0, 1000.0[	-	-	$1.17 \pm 0.53 \pm 0.06$	$0.83 \pm 0.42 \pm 0.04$	$1.51 \pm 1.33 \pm 0.07$
[1000.0, 2000.0[	-	$1.66 \pm 0.45 \pm 0.38$	$1.46 \pm 0.22 \pm 0.93$	$1.09 \pm 0.19 \pm 0.15$	$1.11 \pm 0.38 \pm 0.05$
[2000.0, 3000.0[	$2.07 \pm 0.98 \pm 0.10$	$1.40 \pm 0.19 \pm 236.65$	-	$0.90 \pm 0.11 \pm 0.05$	$0.93 \pm 0.19 \pm 0.05$
[3000.0, 4000.0[	$0.86 \pm 0.23 \pm 0.04$	$0.58 \pm 0.07 \pm 0.03$	$0.53 \pm 0.06 \pm 0.17$	$0.36 \pm 0.05 \pm 0.08$	$0.58 \pm 0.13 \pm 0.03$
[4000.0, 5000.0[	$0.45 \pm 0.10 \pm 0.02$	$0.30 \pm 0.04 \pm 0.01$	$0.23 \pm 0.03 \pm 0.01$	$0.15 \pm 0.03 \pm 0.01$	$0.15 \pm 0.07 \pm 0.01$
[5000.0, 6000.0[	$0.26 \pm 0.06 \pm 0.01$	$0.13 \pm 0.02 \pm 0.01$	$0.13 \pm 0.02 \pm 0.01$	$0.12 \pm 0.02 \pm 0.01$	$0.18 \pm 0.14 \pm 0.01$
[6000.0, 7000.0[	$0.11 \pm 0.03 \pm 0.01$	$0.07 \pm 0.01 \pm 0.00$	$0.07 \pm 0.01 \pm 0.00$	$0.05 \pm 0.02 \pm 0.00$	-
[7000.0, 8000.0[	$0.05 \pm 0.02 \pm 0.00$	$0.06 \pm 0.01 \pm 0.00$	$0.03 \pm 0.01 \pm 0.00$	$0.05 \pm 0.03 \pm 0.00$	-

Table 9.0.5: Table of the D^{*+} cross-section normalised to the measured result for $2\,\text{GeV} < p_T < 3\,\text{GeV}$ and $3.0 < y < 3.5$ from $D^{*+} \to \left(D^0 \to K^-\pi^+\right)\pi^+$ decays.

	[2.0, 2.5[	[2.5, 3.0[	[3.0, 3.5[	[3.5, 4.0[	[4.0, 4.5[
[0.0, 1000.0[	–	–	0.2σ	1.4σ	0.3σ
[1000.0, 2000.0[	–	1.6σ	2.0σ	2.2σ	0.5σ
[2000.0, 3000.0[	–	0.7σ	–	0.5σ	0.8σ
[3000.0, 4000.0[	0.8σ	1.2σ	0.4σ	0.9σ	2.1σ
[4000.0, 5000.0[	0.4σ	1.0σ	0.5σ	0.9σ	0.2σ
[5000.0, 6000.0[	1.3σ	0.7σ	0.4σ	1.3σ	–
[6000.0, 7000.0[	0.3σ	0.1σ	1.2σ	0.8σ	–
[7000.0, 8000.0[	1.0σ	0.7σ	–	–	–

Table 9.0.6: Variation in units of the standard deviation between the results presented here and the previous LHCb measurement for the cross-section of D^{*+} normalised to the measured result in $2\,\text{GeV} < p_T < 3\,\text{GeV}$ and $3.0 < y < 3.5$ from $D^{*+} \to \left(D^0 \to K^-\pi^+\right)\pi^+$ decays.

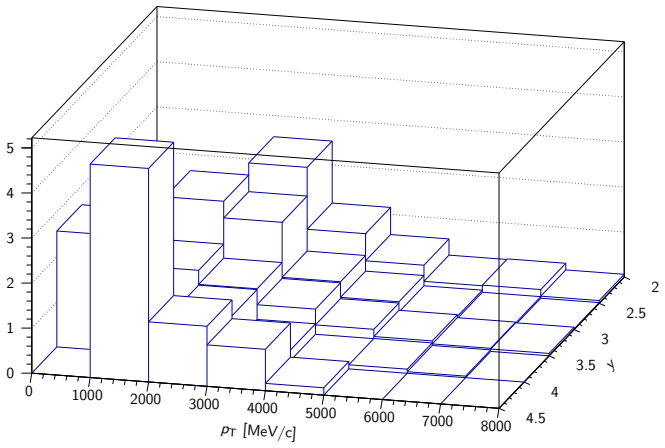

Figure 9.0.4: Plot of the D^+ cross-section normalised to the measured result for $2\,\text{GeV} < p_T < 3\,\text{GeV}$ and $3.0 < y < 3.5$ from $D^+ \to K^-K^+\pi^+$ decays. Any regions with a greater than 100 % statistical error have been removed.

	[2.0, 2.5[	[2.5, 3.0[	[3.0, 3.5[	[3.5, 4.0[	[4.0, 4.5[
[0.0, 1000.0[	-	$1.23 \pm 2.76 \pm 1.58$	-	$2.57 \pm 2.31 \pm 3.30$	-
[1000.0, 2000.0[	-	$2.26 \pm 0.75 \pm 2.91$	$1.31 \pm 0.91 \pm 5.85$	$1.29 \pm 1.43 \pm 3.27$	$4.74 \pm 3.14 \pm 6.09$
[2000.0, 3000.0[	$2.53 \pm 0.87 \pm 3.25$	$1.89 \pm 0.63 \pm 15.04$	-	$0.98 \pm 0.29 \pm 1.26$	$1.33 \pm 0.66 \pm 1.71$
[3000.0, 4000.0[	$1.16 \pm 0.36 \pm 1.48$	$0.67 \pm 0.17 \pm 0.86$	$0.65 \pm 0.16 \pm 0.83$	$0.32 \pm 0.10 \pm 0.41$	$0.92 \pm 0.36 \pm 1.18$
[4000.0, 5000.0[	$0.55 \pm 0.19 \pm 0.71$	$0.32 \pm 0.09 \pm 0.42$	$0.30 \pm 0.08 \pm 0.38$	$0.09 \pm 0.04 \pm 0.11$	$0.16 \pm 0.14 \pm 0.21$
[5000.0, 6000.0[	$0.19 \pm 0.08 \pm 0.25$	$0.10 \pm 0.04 \pm 0.12$	$0.14 \pm 0.04 \pm 0.17$	$0.09 \pm 0.04 \pm 0.12$	-
[6000.0, 7000.0[	$0.21 \pm 0.08 \pm 0.27$	$0.05 \pm 0.02 \pm 0.06$	$0.07 \pm 0.03 \pm 0.09$	$0.03 \pm 0.02 \pm 0.04$	-
[7000.0, 8000.0[	$0.06 \pm 0.04 \pm 0.08$	$0.02 \pm 0.01 \pm 0.02$	$0.05 \pm 0.02 \pm 0.07$	$0.02 \pm 0.03 \pm 0.02$	-

Table 9.0.7: Table of the D^+ cross-section normalised to the measured result for $2\,\text{GeV} < p_T < 3\,\text{GeV}$ and $3.0 < y < 3.5$ from $D^+ \to K^-K^+\pi^+$ decays.

	[2.0, 2.5[	[2.5, 3.0[	[3.0, 3.5[	[3.5, 4.0[	[4.0, 4.5[
[0.0, 1000.0[	–	0.1σ	–	0.7σ	–
[1000.0, 2000.0[	–	0.6σ	0.5σ	0.2σ	1.1σ
[2000.0, 3000.0[	1.7σ	1.2σ	–	0.6σ	1.2σ
[3000.0, 4000.0[	1.7σ	0.7σ	1.1σ	0.3σ	1.9σ
[4000.0, 5000.0[	1.6σ	0.7σ	1.2σ	1.4σ	0.6σ
[5000.0, 6000.0[	0.9σ	0.7σ	1.0σ	0.7σ	–
[6000.0, 7000.0[	1.8σ	0.4σ	0.2σ	0.3σ	–
[7000.0, 8000.0[	0.5σ	1.3σ	1.3σ	0.2σ	–

Table 9.0.8: Variation in units of the standard deviation between the results presented here and the previous LHCb measurement for the cross-section of D^+ normalised to the measured result in $2\,\text{GeV} < p_T < 3\,\text{GeV}$ and $3.0 < y < 3.5$ from $D^+ \to K^-K^+\pi^+$ decays.

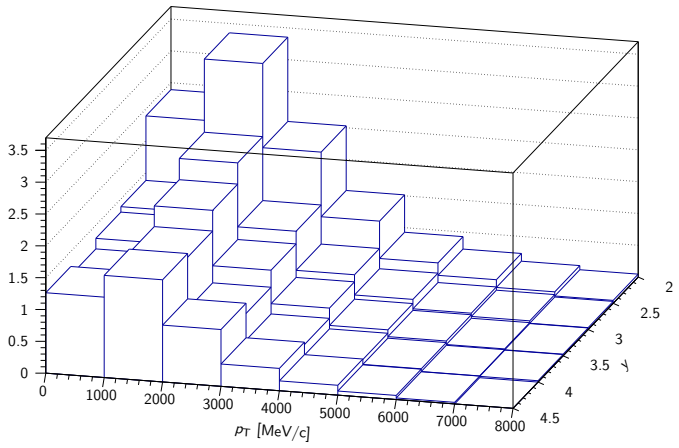

Figure 9.0.5: Plot of the D^+ cross-section normalised to the measured result for $2\,\text{GeV} < p_T < 3\,\text{GeV}$ and $3.0 < y < 3.5$ from $D^+ \to K^-\pi^+\pi^+$ decays. Any regions with a greater than 100 % statistical error have been removed.

	[2.0, 2.5[	[2.5, 3.0[	[3.0, 3.5[	[3.5, 4.0[	[4.0, 4.5[
[0.0, 1000.0[	$2.39 \pm 0.57 \pm 0.13$	$1.38 \pm 0.06 \pm 0.07$	$1.29 \pm 0.06 \pm 0.83$	$1.13 \pm 0.10 \pm 0.74$	$1.26 \pm 0.09 \pm 0.07$
[1000.0, 2000.0[	$3.35 \pm 0.23 \pm 0.18$	$2.20 \pm 0.07 \pm 2.40$	$1.87 \pm 0.08 \pm 1.40$	$1.55 \pm 0.06 \pm 57.87$	$1.60 \pm 0.07 \pm 0.08$
[2000.0, 3000.0[	$2.03 \pm 0.08 \pm 0.11$	$1.20 \pm 0.03 \pm 0.13$	-	$0.73 \pm 0.02 \pm 0.06$	$0.89 \pm 0.04 \pm 0.05$
[3000.0, 4000.0[	$1.01 \pm 0.03 \pm 0.05$	$0.59 \pm 0.01 \pm 0.18$	$0.47 \pm 0.01 \pm 0.03$	$0.31 \pm 0.01 \pm 0.14$	$0.35 \pm 0.02 \pm 0.02$
[4000.0, 5000.0[	$0.43 \pm 0.02 \pm 0.02$	$0.27 \pm 0.01 \pm 0.01$	$0.20 \pm 0.01 \pm 0.08$	$0.15 \pm 0.00 \pm 0.01$	$0.15 \pm 0.01 \pm 0.01$
[5000.0, 6000.0[	$0.23 \pm 0.01 \pm 0.01$	$0.12 \pm 0.00 \pm 0.01$	$0.09 \pm 0.00 \pm 0.00$	$0.07 \pm 0.00 \pm 0.00$	$0.06 \pm 0.01 \pm 0.00$
[6000.0, 7000.0[	$0.11 \pm 0.01 \pm 0.01$	$0.07 \pm 0.00 \pm 0.00$	$0.04 \pm 0.00 \pm 0.00$	$0.03 \pm 0.00 \pm 0.00$	$0.02 \pm 0.01 \pm 0.00$
[7000.0, 8000.0[	$0.05 \pm 0.00 \pm 0.00$	$0.03 \pm 0.00 \pm 0.00$	$0.03 \pm 0.00 \pm 0.00$	$0.02 \pm 0.00 \pm 0.00$	-

Table 9.0.9: Table of the D^+ cross-section normalised to the measured result for $2\,\text{GeV} < p_T < 3\,\text{GeV}$ and $3.0 < y < 3.5$ from $D^+ \to K^-\pi^+\pi^+$ decays.

	[2.0, 2.5[	[2.5, 3.0[	[3.0, 3.5[	[3.5, 4.0[	[4.0, 4.5[
[0.0, 1000.0[	–	0.6σ	1.1σ	0.9σ	2.3σ
[1000.0, 2000.0[	2.9σ	2.6σ	1.0σ	0.1σ	3.0σ
[2000.0, 3000.0[	5.0σ	1.4σ	–	1.4σ	4.0σ
[3000.0, 4000.0[	5.6σ	1.3σ	0.3σ	1.7σ	3.5σ
[4000.0, 5000.0[	4.5σ	0.6σ	0.1σ	0.4σ	3.0σ
[5000.0, 6000.0[	4.6σ	0.2σ	0.3σ	0.6σ	1.9σ
[6000.0, 7000.0[	3.2σ	1.3σ	6.1σ	0.1σ	–
[7000.0, 8000.0[	0.6σ	0.6σ	0.4σ	1.8σ	–

Table 9.0.10: Variation in units of the standard deviation between the results presented here and the previous LHCb measurement for the cross-section of D^+ normalised to the measured result in $2\,\text{GeV} < p_T < 3\,\text{GeV}$ and $3.0 < y < 3.5$ from $D^+ \to K^-\pi^+\pi^+$ decays.

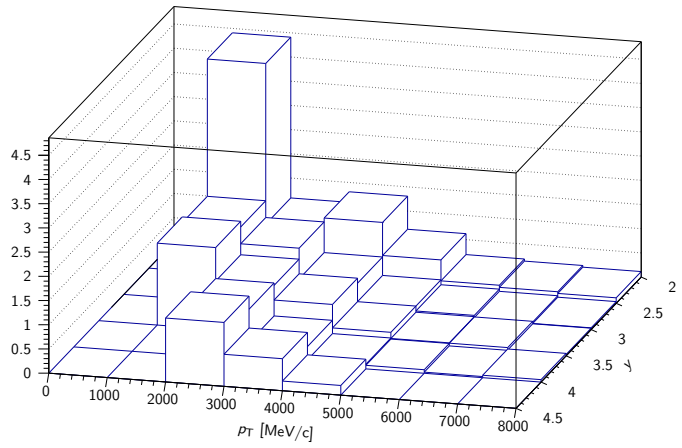

Figure 9.0.6: Plot of the D_s^+ cross-section normalised to the measured result for $2\,\text{GeV} < p_T < 3\,\text{GeV}$ and $3.0 < y < 3.5$ from $D_s^+ \to \left(\phi \to K^- K^+\right)\pi^+$ decays. Any regions with a greater than 100 % statistical error have been removed.

	[2.0, 2.5[	[2.5, 3.0[	[3.0, 3.5[	[3.5, 4.0[	[4.0, 4.5[
[0.0, 1000.0[	-	$0.52 \pm 0.71 \pm 0.06$	$4.99 \pm 5.58 \pm 132.77$	-	$5.48 \pm 12.49 \pm 0.20$
[1000.0, 2000.0[	$4.41 \pm 1.96 \pm 0.02$	$1.57 \pm 0.50 \pm 0.42$	$1.69 \pm 0.50 \pm 1.30$	$0.81 \pm 1.57 \pm 5.21$	-
[2000.0, 3000.0[	$1.09 \pm 0.42 \pm 0.01$	$1.23 \pm 0.27 \pm 0.06$	-	$1.05 \pm 0.25 \pm 0.01$	$1.32 \pm 0.59 \pm 0.01$
[3000.0, 4000.0[	$1.31 \pm 0.34 \pm 0.01$	$0.59 \pm 0.13 \pm 0.00$	$0.70 \pm 0.15 \pm 1.92$	$0.37 \pm 0.09 \pm 0.00$	$0.66 \pm 0.27 \pm 0.00$
[4000.0, 5000.0[	$0.62 \pm 0.17 \pm 0.00$	$0.21 \pm 0.05 \pm 0.00$	$0.21 \pm 0.05 \pm 0.00$	$0.10 \pm 0.04 \pm 0.00$	$0.20 \pm 0.13 \pm 0.00$
[5000.0, 6000.0[	$0.19 \pm 0.07 \pm 0.00$	$0.11 \pm 0.03 \pm 0.00$	$0.09 \pm 0.03 \pm 0.00$	$0.07 \pm 0.03 \pm 0.00$	-
[6000.0, 7000.0[	$0.15 \pm 0.06 \pm 0.00$	$0.07 \pm 0.02 \pm 0.00$	$0.08 \pm 0.02 \pm 0.00$	$0.02 \pm 0.01 \pm 0.00$	-
[7000.0, 8000.0[	$0.11 \pm 0.04 \pm 0.00$	$0.04 \pm 0.01 \pm 0.00$	$0.03 \pm 0.01 \pm 0.00$	$0.05 \pm 0.03 \pm 0.00$	-

Table 9.0.11: Table of the D_s^+ cross-section normalised to the measured result for $2\,\text{GeV} < p_T < 3\,\text{GeV}$ and $3.0 < y < 3.5$ from $D_s^+ \to \left(\phi \to K^- K^+\right)\pi^+$ decays.

	[2.0, 2.5[	[2.5, 3.0[	[3.0, 3.5[	[3.5, 4.0[	[4.0, 4.5[
[0.0, 1000.0[	–	–	0.7σ	–	–
[1000.0, 2000.0[	0.9σ	0.7σ	0.9σ	0.2σ	–
[2000.0, 3000.0[	0.9σ	1.2σ	–	1.0σ	1.0σ
[3000.0, 4000.0[	1.9σ	0.3σ	1.2σ	0.0σ	1.1σ
[4000.0, 5000.0[	1.7σ	0.0σ	1.0σ	1.3σ	–
[5000.0, 6000.0[	1.0σ	0.1σ	0.0σ	0.2σ	–
[6000.0, 7000.0[	1.0σ	0.5σ	0.6σ	–	–
[7000.0, 8000.0[	1.0σ	–	0.3σ	–	–

Table 9.0.12: Variation in units of the standard deviation between the results presented here and the previous LHCb measurement for the cross-section of D_s^+ normalised to the measured result in $2\,\text{GeV} < p_T < 3\,\text{GeV}$ and $3.0 < y < 3.5$ from $D_s^+ \to \left(\phi \to K^- K^+\right)\pi^+$ decays.

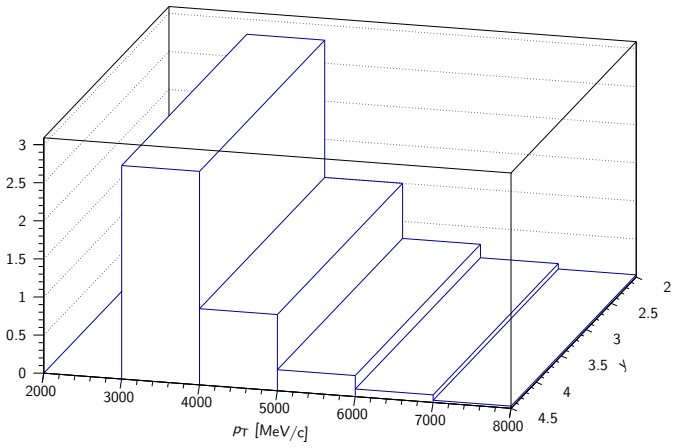

Figure 9.0.7: Plot of the Λ_c^+ cross-section normalised to the measured result for $2\,\text{GeV} < p_T < 3\,\text{GeV}$ and $3.0 < y < 3.5$ from $\Lambda_c^+ \to pK^-\pi^+$ decays. Any regions with a greater than 100 % statistical error have been removed.

	$[2.0, 4.5[$
$[2000.0, 3000.0[$	$15.80 \pm 24.68 \pm 115.47$
$[3000.0, 4000.0[$	$2.80 \pm 1.46 \pm 17.71$
$[4000.0, 5000.0[$	-
$[5000.0, 6000.0[$	$0.28 \pm 0.20 \pm 1.95$
$[6000.0, 7000.0[$	$0.10 \pm 0.08 \pm 0.62$
$[7000.0, 8000.0[$	$0.03 \pm 0.02 \pm 0.20$

Table 9.0.13: Table of the Λ_c^+ cross-section normalised to the measured result for $2\,\text{GeV} < p_T < 3\,\text{GeV}$ and $3.0 < y < 3.5$ from $\Lambda_c^+ \to pK^-\pi^+$ decays.

	$[2.0, 4.5[$
$[2000.0, 3000.0[$	0.5σ
$[3000.0, 4000.0[$	0.3σ
$[4000.0, 5000.0[$	–
$[5000.0, 6000.0[$	0.4σ
$[6000.0, 7000.0[$	1.2σ
$[7000.0, 8000.0[$	3.1σ

Table 9.0.14: Variation in units of the standard deviation between the results presented here and the previous LHCb measurement for the cross-section of Λ_c^+ normalised to the measured result in $2\,\text{GeV} < p_T < 3\,\text{GeV}$ and $3.0 < y < 3.5$ from $\Lambda_c^+ \to pK^-\pi^+$ decays.

10

Systematic uncertainties and further studies

The work described in this thesis forms an ongoing analysis in the LHCb collaboration. As previously discussed in Section 7.4 and Chapter 9, the cause of anomalies in the particle identification efficiency and the final result remain unknown and are being actively studied. In addition, this work forms the basis of the strategy that will be used to measure the open charm hadron production cross-section at $\sqrt{s} = 13\,\text{TeV}$ using data taken in the initial weeks LHC Run 2. Once the aforementioned discrepancies have been resolved, the systematic uncertainties associated with the measurement must be assessed. Some possible causes include:

PID binning scheme

The reweighing of the calibration sample to obtain the efficiency of the PID selection assumes that the efficiency is constant within any given bin. This assumption is invalid, as shown in Figure 7.4.2, and must be accounted for.

PID calibration sample size

The size of the calibration sample used for the PID efficiency determination is limited and has a statistical uncertainty associated with the efficiency of any selections applied to it. While this uncertainty is statistical in nature, it is taken as a systematic uncertainty for these measurements as it not strictly dependent on the size of the dataset used for this analysis.[1] This is the only systematic uncertainty listed in Chapter 9 and is calculated by performing toy studies. The efficiency in each bin of the calibration sample is taken to be a Gaussian distribution centred at the nominal efficiency with standard deviation equal to the statistical error. An efficiency is then generated at random for each calibration bin and the PID efficiency is recalculated. This process is repeated 1000 times and the standard deviation of these studies is taken as a systematic uncertainty.

[1] Of course the calibration sample size would likely increase with additional data taking as this is taken in parallel to the data used for this measurement.

Fit model

The probability distribution functions used to extract the signal yield for this analysis have been chosen empirically with little physical basis for their shapes. As such, there is a systematic uncertainty associated with the yield obtained to account for the difference between the distribution used and the true distributions present in the data. In addition, there exists an uncertainty on the proportion of secondary charm production present in the signal sample, especially as this method of extracting this quantity is reliant on simulated events to model the distribution of the impact parameter χ^2.

Monte Carlo-data disagreement

The Monte Carlo generators and subsequent detector simulation does not provide a perfect description of the physical data and some discrepancies are known to exist. Any areas of the analysis which are dependent on Monte Carlo must be checked with reweighing procedures used and/or systematic uncertainties assigned to account for any discrepancies.

Monte Carlo truth matching

After simulating an event the reconstruction algorithm is applied to Monte Carlo and associations are made between the generated and reconstructed tracks to find the number of correctly reconstructed events. The limited computing resources available prevents an exhaustive search being performed and therefore the true reconstruction efficiency is marginally larger than the one obtained from simulation.

Tracking

An estimate of the systematic uncertainty associated with the track reconstruction efficiency is provided by the LHCb collaboration's tracking group alongside the ratios used in Section 7.4. For the data shown here, this systematic uncertainty is 0.4 % per track, i.e. for $D^+ \to K^-\pi^+\pi^+$ the systematic uncertainty associated with the tracking efficiency would be 1.2 %. The techniques used to obtain this error are explained in Reference [39].

Other external sources

Sources of systematic uncertainty external to the analysis exist from the luminosity calibration, branching fractions, tracking and other sources.

In addition to the measurement that will be made at $\sqrt{s} = 13\,\text{TeV}$, this analysis is also planned to be repeated with data taken by the LHCb detector in 2012 with $\sqrt{s} = 8\,\text{TeV}$.

11
Conclusion

In conclusion, the measurement of the open production cross-sections of D^0, D^{*+}, D^+, D_s^+ and Λ_c^+ at $\sqrt{s} = 7\,\text{TeV}$ is progressing well and the analysis is expected to be ready in advance of the availability of LHC Run 2 data. Good agreement in seen with previous results in the central acceptance of the LHCb detector and the discrepancies in the outer regions are under active investigation. The evaluation of the systematic uncertainties associated with this analysis has begun and will follow well established techniques used for other LHCb measurements.

Bibliography

[1] R. Aaij et al. “Prompt charm production in pp collisions at sqrt(s)=7 TeV”. In: 871.1 (June 2013), pp. 1–20. ISSN: 05503213. URL: http://arxiv.org/abs/1302.2864.

[2] Matteo Cacciari et al. “Theoretical predictions for charm and bottom production at the LHC”. In: 2012.10 (Oct. 2012), p. 137. ISSN: 11266708. URL: http://link.springer.com/10.1007/JHEP10(2012)137.

[3] Julie Haffner. “The CERN accelerator complex”. In: (Oct. 2013). URL: http://cds.cern.ch/record/1621894/.

[4] The ATLAS Collaboration. *ATLAS Integrated Luminosity 2012*. 2012. URL: http://cern.ch/go/N6gL.

[5] The CMS Collaboration. *CMS Integrated Luminosity 2012*. 2012. URL: http://cern.ch/go/wH9p.

[6] The LHCb Collaboration. *LHCb Integrated Luminosity 2012*. 2012. URL: http://cern.ch/go/998V.

[7] LHCb collaboration et al. “LHCb Detector Performance”. In: (Dec. 2014). URL: http://arxiv.org/abs/1412.6352.

[8] The LHCb Collaboration. *bb production angle plots*. 2008. URL: http://lhcb.web.cern.ch/lhcb/speakersbureau/html/bb%5C_ProductionAngles.html.

[9] Rolf Lindner. *LHCb Detector Layout*. Feb. 2008. URL: https://cds.cern.ch/record/1087860.

[10] The LHCb Collaboration et al. “The LHCb Detector at the LHC”. In: 3.08 (Aug. 2008), S08005–S08005. ISSN: 1748-0221. URL: http://stacks.iop.org/1748-0221/3/i=08/a=S08005.

[11] R Aaij et al. “Performance of the LHCb Vertex Locator”. In: 9.09 (Sept. 2014), P09007–P09007. ISSN: 1748-0221. URL: https://cds.cern.ch/record/1707015?ln=en.

[12] R Aaij et al. “Precision measurement of the B0s-B0sbar oscillation frequency with the decay B0s Ds +”. In: *IOP Publishing* 15.5 (2013), p. 053021. URL: http://iopscience.iop.org/1367-2630/15/5/053021/article/.

[13] Xavier Vilasís Cardona. “First years of running for the LHCb calorimeters”. In: 404.1 (Dec. 2012), p. 012003. ISSN: 1742-6588. URL: http://stacks.iop.org/1742-6596/404/i=1/a=012003.

[14] Torbjörn Sjöstrand, Stephen Mrenna, and Peter Skands. “PYTHIA 6.4 physics and manual”. In: 2006.05 (May 2006), pp. 026–026. ISSN: 1029-8479. URL: http://stacks.iop.org/1126-6708/2006/i=05/a=026.

[15] I Beiyaev et al. “Handling of the generation of primary events in Gauss, the LHCb simulation framework”. In: *IEEE*. IEEE, Oct. 2010, pp. 1155–1161. ISBN: 978-1-4244-9106-3. URL: http://ieeexplore.ieee.org/lpdocs/epic03/wrapper.htm?arnumber=5873949.

[16] David J. Lange. “The EvtGen particle decay simulation package”. In: 462.1-2 (Apr. 2001), pp. 152–155. ISSN: 01689002. URL: http://www.sciencedirect.com/science/article/pii/S0168900201000894.

[17] P. Golonka and Z. Was. “PHOTOS Monte Carlo: a precision tool for QED correctionsin Z and W decays”. In: 45.1 (Jan. 2006), pp. 97–107. ISSN: 1434-6044. URL: http://www.springerlink.com/index/10.1140/epjc/s2005-02396-4.

[18] S. Agostinelli et al. “Geant4-a simulation toolkit”. In: 506.3 (July 2003), pp. 250–303. ISSN: 01689002. URL: http://www.sciencedirect.com/science/article/pii/S0168900203013688.

[19] M Clemencic et al. “The LHCb Simulation Application, Gauss: Design, Evolution and Experience”. In: 331.3 (Dec. 2011), p. 032023. ISSN: 1742-6596. URL: http://stacks.iop.org/1742-6596/331/i=3/a=032023.

[20] Bernd A. Kniehl et al. “Inclusive charmed-meson production at the CERN LHC”. In: 72.7 (July 2012), p. 2082. ISSN: 1434-6044. URL: http://www.springerlink.com/index/10.1140/epjc/s10052-012-2082-2.

[21] F. D. Aaron et al. “Combined measurement and QCD analysis of the inclusive e ś p scattering cross sections at HERA”. In: 2010.1 (Jan. 2010), p. 109. ISSN: 1029-8479. URL: http://link.springer.com/10.1007/JHEP01(2010)109.

[22] J. F. Owens, A. Accardi, and W. Melnitchouk. “Global parton distributions with nuclear and finite-Q extasciicircum{2} corrections”. In: 87.9 (May 2013), p. 094012. ISSN: 1550-7998. URL: http://inspirehep.net/record/1206325.

[23] A. D. Martin et al. “Parton distributions for the LHC”. In: 63.2 (July 2009), pp. 189–285. ISSN: 1434-6044. URL: http://arxiv.org/abs/0901.0002.

[24] S. Alekhin et al. “HERAFitter, Open Source QCD Fit Project”. In: (Oct. 2014), p. 18. URL: http://arxiv.org/abs/1410.4412.

[25] Oleksandr Zenaiev et al. “Impact of heavy-flavour production cross sections measured by the LHCb experiment on parton distribution functions at low x”. In: (Mar. 2015). URL: http://arxiv.org/abs/1503.04581.

[26] M G Aartsen et al. “Evidence for high-energy extraterrestrial neutrinos at the IceCube detector.” In: 342.6161 (Nov. 2013), p. 1242856. ISSN: 1095-9203. URL: http://www.sciencemag.org/content/342/6161/1242856.

[27] Atri Bhattacharya et al. “Perturbative charm production and the prompt atmospheric neutrino flux in light of RHIC and LHC”. In: (Feb. 2015), p. 19. URL: http://arxiv.org/abs/1502.01076.

[28] K.A. Olive. “Review of Particle Physics”. In: 38.9 (Aug. 2014), p. 090001. ISSN: 1674-1137. URL: http://stacks.iop.org/1674-1137/38/i=9/a=090001.

[29] M Bajko et al. “Report of the Task Force on the Incident of 19th September 2008 at the LHC”. In: (Mar. 2009). URL: https://cdsweb.cern.ch/record/1168025/.

[30] R. Aaij et al. “Measurement of J/ production in pp collisions at $\sqrt{\{s\}} = 7$ TeV”. In: 71.5 (May 2011), p. 1645. ISSN: 1434-6044. URL: http://arxiv.org/abs/1103.0423.

[31] M. Pivk and F.R. Le Diberder. “sPlot: A statistical tool to unfold data distributions”. In: 555.1-2 (Dec. 2005), pp. 356–369. ISSN: 01689002. URL: http://www.sciencedirect.com/science/article/pii/S0168900205018024.

[32] A. Hoecker et al. “TMVA - Toolkit for Multivariate Data Analysis”. In: (Mar. 2007), p. 135. URL: http://arxiv.org/abs/physics/0703039.

[33] R. J. Barlow. *Statistics: A Guide to the Use of Statistical Methods in the Physical Sciences*. John Wiley & Sons, 1989, p. 204. ISBN: 0471922951. URL: https://books.google.com/books?id=qqKgx47QMX8C%5C&pgis=1.

[34] M Adinolfi et al. “Performance of the LHCb RICH detector at the LHC.” In: 73.5 (Jan. 2012), p. 2431. ISSN: 1434-6044. URL: http://arxiv.org/abs/1211.6759.

[35] J Albrecht et al. “Implications of post-LS1 running conditions on LHCb’s data processing”. In: (June 2013). URL: https://cds.cern.ch/record/1556085?ln=en.

[36] The LHCb Collaboration. “Reco14 tracking efficiency ratios”. In: (2013). URL: https://twiki.cern.ch/twiki/bin/view/LHCb/TrackingEffStatus2012S20.

[37] Alan Agresti and Brent a Coull. “Estimation of Binomial Proportions”. In: 52.2 (2012), pp. 119–126.

[38] James Fred. *The Interpretation of Errors*. Tech. rep. 2014. URL: http://seal.web.cern.ch/seal/documents/minuit/mnerror.pdf.

[39] The LHCb collaboration. "Measurement of the track reconstruction efficiency at LHCb". In: 10.02 (Feb. 2015), P02007–P02007. ISSN: 1748-0221. URL: http://stacks.iop.org/1748-0221/10/i=02/a=P02007.

[40] Matteo Cacciari, Mario Greco, and Paolo Nason. "The p T spectrum in heavy-flavour hadroproduction". In: 1998.05 (May 1998), pp. 007–007. ISSN: 1029-8479. URL: http://arxiv.org/abs/hep-ph/9803400.

[41] L. Gladilin. "Charm Hadron Production Fractions". In: (Dec. 1999), p. 6. URL: http://arxiv.org/abs/hep-ex/9912064.

Appendices

A

Crossing angle correction

In the ideal case, each beam of the LHC would have momentum in only the $\pm z$ direction and therefore the centre of mass reference frame would be the same as the laboratory frame. Unfortunately this is not the case as the LHC is a storage ring and after each intersection the beams must be recaptured by the LHC and therefore a small crossing angle is present, as depicted in Figure A.0.1. As a result a Lorentz boost is require to obtain a value the transverse momentum and rapidity of particles in the centre of mass frame.

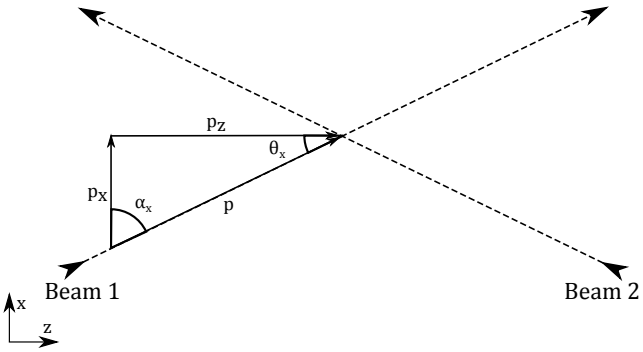

Figure A.0.1: Graphic showing the crossing of two beams in the z-x plane.

To find the required boost we must first find the scalar product between the beam momentum p and each transverse axis.

$$p_x = \mathbf{p} \cdot \hat{\mathbf{x}} = |\mathbf{p}| \cos(\alpha_x)$$
$$p_y = \mathbf{p} \cdot \hat{\mathbf{y}} = |\mathbf{p}| \cos(\alpha_y)$$

From these we can then find the z component of the beam momentum.

$$p_z = \sqrt{|\mathbf{p}|^2 - p_x^2 - p_y^2} = |\mathbf{p}| \sqrt{1 - \cos^2(\alpha_x) - \cos^2(\alpha_y)}$$

As the beam energy, E_b, and proton mass, m_p, are known the beam momentum is also

known.

$$|\mathbf{p}| = \sqrt{E_b^2 - m_p^2}$$

The crossing angle is generally defined in terms of θ rather than α, therefore the components of the beam momentum are given by:

$$\begin{aligned}
p_x &= \sin(\theta_x)\sqrt{E_b^2 - m_p^2} \\
p_y &= \sin(\theta_y)\sqrt{E_b^2 - m_p^2} \\
p_z &= \sqrt{E_b^2 - m_p^2}\sqrt{1 - \sin^2(\theta_x) - \sin^2(\theta_y)}
\end{aligned}$$

The laboratory frame of the two beams is then given by $\mathbf{p}_{\text{Lab}}$.

$$\begin{aligned}
\mathbf{p}_{\text{Lab}} &= \begin{pmatrix} E_b \\ \sin(\theta_x)\sqrt{E_b^2 - m_p^2} \\ \sin(\theta_y)\sqrt{E_b^2 - m_p^2} \\ \sqrt{E_b^2 - m_p^2}\sqrt{1 - \sin^2(\theta_x) - \sin^2(\theta_y)} \end{pmatrix} + \begin{pmatrix} E_b \\ \sin(\theta_x)\sqrt{E_b^2 - m_p^2} \\ \sin(\theta_y)\sqrt{E_b^2 - m_p^2} \\ -\sqrt{E_b^2 - m_p^2}\sqrt{1 - \sin^2(\theta_x) - \sin^2(\theta_y)} \end{pmatrix} \\
&= \begin{pmatrix} 2E_b \\ 2\sin(\theta_x)\sqrt{E_b^2 - m_p^2} \\ 2\sin(\theta_y)\sqrt{E_b^2 - m_p^2} \\ 0 \end{pmatrix}
\end{aligned}$$

Any product of the interaction with 4-momentum, $\mathbf{p}_{\text{hadron, lab}}$, can then be boosted to the centre of mass frame using,

$$\mathbf{p}_{\text{hadron, COM}} = \begin{pmatrix} \gamma & -\gamma\beta_x & -\gamma\beta_y & 0 \\ -\gamma\beta_x & 1 + (\gamma - 1)\dfrac{\beta_x^2}{\beta^2} & (\gamma - 1)\dfrac{\beta_x\beta_y}{\beta^2} & 0 \\ -\gamma\beta_y & (\gamma - 1)\dfrac{\beta_y\beta_x}{\beta^2} & 1 + (\gamma - 1)\dfrac{\beta_y^2}{\beta^2} & 0 \\ 0 & 0 & 0 & 1 \end{pmatrix} \cdot \mathbf{p}_{\text{hadron, lab}}$$

where,

$$\begin{aligned}
\beta_x &= -p_{\text{Lab, }x} \\
\beta_y &= -p_{\text{Lab, }y} \\
\beta^2 &= \sqrt{\beta_x^2 + \beta_y^2} \\
\gamma &= \frac{1}{\sqrt{1 - \beta^2}}.
\end{aligned}$$

B

FONLL predictions

Theoretical predictions using the FONLL model were obtained using the online web calculator available at:

http://www.lpthe.jussieu.fr/~cacciari/fonll/fonllform.html[40]

with the CTEQ6.6 PDF set and D meson fragmentation ratios shown in Table B.0.1.

Hadron	Fragmentation ratio
D^0	0.549
D^{*+}	0.235
D^+	0.232

Table B.0.1: Fragmentation ratios used in the hadronisation of charm quarks for the FONNLL predictions, taken from Reference [41].

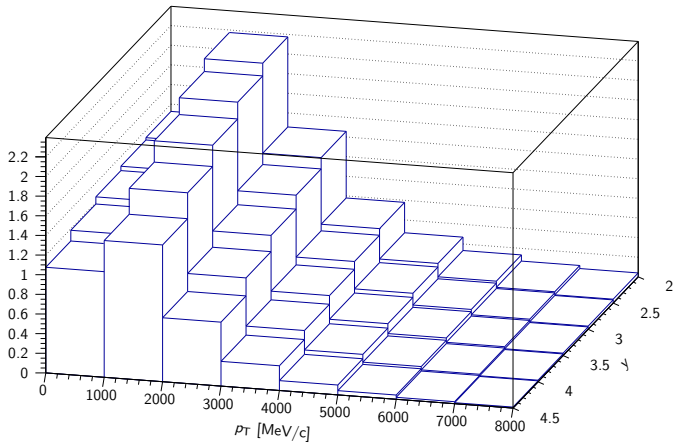

Figure B.0.1: Plot of the FONLL prediction for the D^0 cross-section normalised to the result for $2\,\text{GeV} < p_T < 3\,\text{GeV}$ and $3.0 < y < 3.5$.

	[2.0,2.5[	[2.5,3.0[	[3.0,3.5[	[3.5,4.0[	[4.0,4.5[
[0.0,1000.0[	1.33 ± 2.94	1.30 ± 2.90	1.26 ± 2.82	1.19 ± 2.68	1.08 ± 2.44
[1000.0,2000.0[	2.17 ± 3.86	2.04 ± 3.64	1.87 ± 3.34	1.66 ± 2.97	1.39 ± 2.51
[2000.0,3000.0[	1.26 ± 1.91	1.14 ± 1.74	-	0.83 ± 1.28	0.65 ± 1.00
[3000.0,4000.0[	0.58 ± 0.80	0.51 ± 0.71	0.43 ± 0.60	0.34 ± 0.48	0.25 ± 0.35
[4000.0,5000.0[	0.27 ± 0.35	0.23 ± 0.30	0.19 ± 0.25	0.15 ± 0.19	0.10 ± 0.13
[5000.0,6000.0[	0.13 ± 0.17	0.11 ± 0.14	0.09 ± 0.11	0.07 ± 0.08	0.04 ± 0.05
[6000.0,7000.0[	0.07 ± 0.09	0.06 ± 0.07	0.05 ± 0.06	0.03 ± 0.04	0.02 ± 0.02
[7000.0,8000.0[	0.04 ± 0.05	0.03 ± 0.04	0.02 ± 0.03	0.02 ± 0.02	0.01 ± 0.01

Table B.0.2: Table of the FONLL prediction for the D^0 cross-section normalised to the result for $2\,\text{GeV} < p_T < 3\,\text{GeV}$ and $3.0 < y < 3.5$.

	[2.0,2.5[	[2.5,3.0[	[3.0,3.5[	[3.5,4.0[	[4.0,4.5[
[0.0,1000.0[	0.2σ	0.1σ	0.1σ	0.1σ	0.2σ
[1000.0,2000.0[	0.2σ	0.1σ	0.0σ	0.0σ	0.1σ
[2000.0,3000.0[	0.3σ	0.1σ	–	0.0σ	0.3σ
[3000.0,4000.0[	0.3σ	0.0σ	0.0σ	0.1σ	0.2σ
[4000.0,5000.0[	0.3σ	0.0σ	0.0σ	0.1σ	0.3σ
[5000.0,6000.0[	0.4σ	0.0σ	0.0σ	0.1σ	0.1σ
[6000.0,7000.0[	0.4σ	0.0σ	0.0σ	0.3σ	–
[7000.0,8000.0[	0.3σ	0.1σ	0.1σ	0.1σ	–

Table B.0.3: Variation in units of the standard deviation between the results presented here and the FONLL prediction for the cross-section of D^0 normalised to the measured result in $2\,\text{GeV} < p_T < 3\,\text{GeV}$ and $3.0 < y < 3.5$ from $D^0 \to K^-\pi^+$ decays.

	[2.0,2.5[	[2.5,3.0[	[3.0,3.5[	[3.5,4.0[	[4.0,4.5[
[0.0,1000.0[	–	–	–	–	–
[1000.0,2000.0[	–	0.0σ	0.2σ	0.2σ	–
[2000.0,3000.0[	0.5σ	0.2σ	–	0.2σ	0.3σ
[3000.0,4000.0[	0.4σ	0.2σ	0.1σ	0.2σ	0.2σ
[4000.0,5000.0[	0.3σ	0.2σ	0.1σ	0.1σ	0.1σ
[5000.0,6000.0[	0.3σ	0.2σ	0.0σ	0.2σ	0.2σ
[6000.0,7000.0[	0.5σ	0.2σ	0.1σ	0.2σ	–
[7000.0,8000.0[	0.5σ	0.1σ	0.0σ	0.2σ	–

Table B.0.4: Variation in units of the standard deviation between the results presented here and the FONLL prediction for the cross-section of D^0 normalised to the measured result in $2\,\text{GeV} < p_T < 3\,\text{GeV}$ and $3.0 < y < 3.5$ from $D^0 \to K^-\pi^+\pi^-\pi^+$ decays.

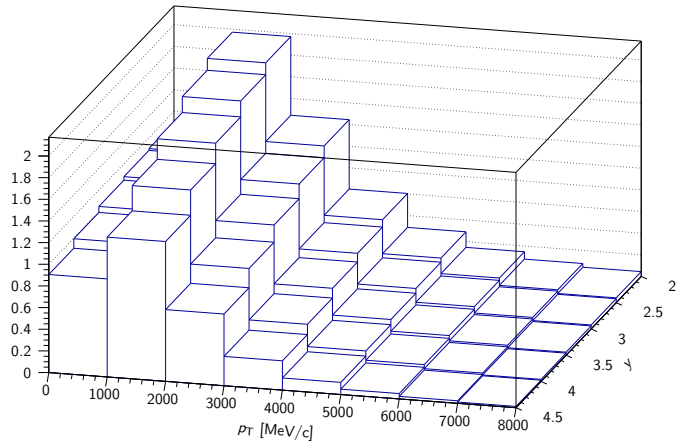

Figure B.0.2: Plot of the FONLL prediction for the D^{*+} cross-section normalised to the result for $2\,\text{GeV} < p_T < 3\,\text{GeV}$ and $3.0 < y < 3.5$.

	[2.0,2.5[	[2.5,3.0[	[3.0,3.5[	[3.5,4.0[	[4.0,4.5[
[0.0,1000.0[	1.10 ± 2.50	1.08 ± 2.47	1.05 ± 2.41	0.99 ± 2.30	0.91 ± 2.11
[1000.0,2000.0[	1.97 ± 3.60	1.86 ± 3.41	1.71 ± 3.15	1.52 ± 2.81	1.29 ± 2.40
[2000.0,3000.0[	1.24 ± 1.96	1.14 ± 1.79	-	0.84 ± 1.33	0.66 ± 1.05
[3000.0,4000.0[	0.60 ± 0.86	0.54 ± 0.77	0.46 ± 0.65	0.37 ± 0.52	0.27 ± 0.39
[4000.0,5000.0[	0.29 ± 0.39	0.25 ± 0.34	0.21 ± 0.28	0.16 ± 0.22	0.11 ± 0.15
[5000.0,6000.0[	0.15 ± 0.19	0.13 ± 0.16	0.10 ± 0.13	0.07 ± 0.10	0.05 ± 0.06
[6000.0,7000.0[	0.08 ± 0.10	0.07 ± 0.08	0.05 ± 0.06	0.04 ± 0.05	0.02 ± 0.03
[7000.0,8000.0[	0.04 ± 0.05	0.04 ± 0.05	0.03 ± 0.03	0.02 ± 0.02	0.01 ± 0.01

Table B.0.5: Table of the FONLL prediction for the D^{*+} cross-section normalised to the result for $2\,\text{GeV} < p_T < 3\,\text{GeV}$ and $3.0 < y < 3.5$.

	[2.0,2.5[	[2.5,3.0[	[3.0,3.5[	[3.5,4.0[	[4.0,4.5[
[0.0,1000.0[	–	–	0.0σ	0.1σ	0.2σ
[1000.0,2000.0[	–	0.1σ	0.1σ	0.2σ	0.1σ
[2000.0,3000.0[	0.2σ	0.1σ	–	0.0σ	0.2σ
[3000.0,4000.0[	0.2σ	0.0σ	0.1σ	0.0σ	0.4σ
[4000.0,5000.0[	0.3σ	0.1σ	0.1σ	0.0σ	0.2σ
[5000.0,6000.0[	0.3σ	0.1σ	0.2σ	0.3σ	0.5σ
[6000.0,7000.0[	0.2σ	0.1σ	0.2σ	0.1σ	–
[7000.0,8000.0[	0.0σ	0.3σ	0.1σ	0.5σ	–

Table B.0.6: Variation in units of the standard deviation between the results presented here and the FONLL prediction for the cross-section of D^{*+} normalised to the measured result in $2\,\text{GeV} < p_T < 3\,\text{GeV}$ and $3.0 < y < 3.5$ from $D^{*+} \to \left(D^0 \to K^-\pi^+\right)\pi^+$ decays.

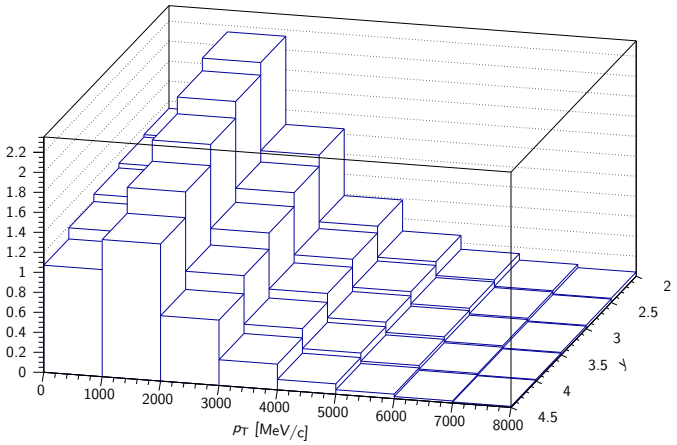

Figure B.0.3: Plot of the FONLL prediction for the D^+ cross-section normalised to the result for $2\,\text{GeV} < p_T < 3\,\text{GeV}$ and $3.0 < y < 3.5$.

	[2.0,2.5[	[2.5,3.0[	[3.0,3.5[	[3.5,4.0[	[4.0,4.5[
[0.0,1000.0[	1.33 ± 2.93	1.30 ± 2.89	1.26 ± 2.81	1.18 ± 2.67	1.07 ± 2.44
[1000.0,2000.0[	2.14 ± 3.81	2.01 ± 3.60	1.84 ± 3.31	1.63 ± 2.94	1.37 ± 2.49
[2000.0,3000.0[	1.25 ± 1.93	1.14 ± 1.76	-	0.84 ± 1.30	0.65 ± 1.02
[3000.0,4000.0[	0.59 ± 0.82	0.52 ± 0.73	0.44 ± 0.62	0.35 ± 0.49	0.26 ± 0.36
[4000.0,5000.0[	0.28 ± 0.36	0.24 ± 0.31	0.20 ± 0.26	0.15 ± 0.20	0.10 ± 0.14
[5000.0,6000.0[	0.14 ± 0.17	0.12 ± 0.15	0.09 ± 0.12	0.07 ± 0.09	0.05 ± 0.06
[6000.0,7000.0[	0.07 ± 0.09	0.06 ± 0.07	0.05 ± 0.06	0.03 ± 0.04	0.02 ± 0.03
[7000.0,8000.0[	0.04 ± 0.05	0.03 ± 0.04	0.03 ± 0.03	0.02 ± 0.02	0.01 ± 0.01

Table B.0.7: Table of the FONLL prediction for the D^+ cross-section normalised to the result for $2\,\text{GeV} < p_T < 3\,\text{GeV}$ and $3.0 < y < 3.5$.

	[2.0,2.5[	[2.5,3.0[	[3.0,3.5[	[3.5,4.0[	[4.0,4.5[
[0.0,1000.0[	0.2σ	0.0σ	0.0σ	0.0σ	0.1σ
[1000.0,2000.0[	0.2σ	0.0σ	0.0σ	0.0σ	0.1σ
[2000.0,3000.0[	0.2σ	0.0σ	–	0.1σ	0.2σ
[3000.0,4000.0[	0.3σ	0.1σ	0.1σ	0.1σ	0.2σ
[4000.0,5000.0[	0.3σ	0.1σ	0.0σ	0.0σ	0.2σ
[5000.0,6000.0[	0.3σ	0.0σ	0.0σ	0.0σ	0.2σ
[6000.0,7000.0[	0.3σ	0.1σ	0.2σ	0.2σ	0.1σ
[7000.0,8000.0[	0.1σ	0.1σ	0.0σ	0.1σ	–

Table B.0.8: Variation in units of the standard deviation between the results presented here and the FONLL prediction for the cross-section of D^+ normalised to the measured result in $2\,\text{GeV} < p_T < 3\,\text{GeV}$ and $3.0 < y < 3.5$ from $D^+ \to K^-\pi^+\pi^+$ decays.

	[2.0, 2.5[	[2.5, 3.0[	[3.0, 3.5[	[3.5, 4.0[	[4.0, 4.5[
[0.0, 1000.0[	–	0.0σ	–	0.2σ	–
[1000.0, 2000.0[	–	0.1σ	0.2σ	0.1σ	0.4σ
[2000.0, 3000.0[	0.3σ	0.3σ	–	0.1σ	0.3σ
[3000.0, 4000.0[	0.3σ	0.2σ	0.2σ	0.1σ	0.5σ
[4000.0, 5000.0[	0.4σ	0.2σ	0.3σ	0.5σ	0.2σ
[5000.0, 6000.0[	0.2σ	0.2σ	0.2σ	0.2σ	–
[6000.0, 7000.0[	0.5σ	0.2σ	0.2σ	0.0σ	–
[7000.0, 8000.0[	0.2σ	0.8σ	0.4σ	0.1σ	–

Table B.0.9: Variation in units of the standard deviation between the results presented here and the FONLL prediction for the cross-section of D^+ normalised to the measured result in $2\,\text{GeV} < p_T < 3\,\text{GeV}$ and $3.0 < y < 3.5$ from $D^+ \to K^-K^+\pi^+$ decays.

C

Tracking efficiency tables

p_T [MeV/c]	y [2,2.5[	[2.5,3[	[3,3.5[	[3.5,4[	[4,4.5[
[7000,8000[	1.0145 ± 0.0009	1.0119 ± 0.0011	1.0005 ± 0.0010	0.9933 ± 0.0015	0.9942 ± 0.0022
[6000,7000[	1.0179 ± 0.0012	1.0134 ± 0.0012	1.0012 ± 0.0011	0.9934 ± 0.0012	0.9940 ± 0.0019
[5000,6000[	1.0204 ± 0.0014	1.0146 ± 0.0014	1.0023 ± 0.0012	0.9931 ± 0.0011	0.9941 ± 0.0017
[4000,5000[	1.0241 ± 0.0019	1.0164 ± 0.0017	1.0041 ± 0.0014	0.9945 ± 0.0014	0.9943 ± 0.0016
[3000,4000[	1.0296 ± 0.0027	1.0190 ± 0.0022	1.0066 ± 0.0018	0.9967 ± 0.0017	0.9949 ± 0.0016
[2000,3000[	1.0370 ± 0.0039	1.0236 ± 0.0029	1.0106 ± 0.0023	1.0003 ± 0.0022	0.9966 ± 0.0020
[1000,2000[	1.0428 ± 0.0043	1.0302 ± 0.0037	1.0152 ± 0.0028	1.0047 ± 0.0029	0.9976 ± 0.0023
[0,1000[	1.0430 ± 0.0040	1.0348 ± 0.0036	1.0177 ± 0.0026	1.0054 ± 0.0028	0.9959 ± 0.0018

Table C.0.1: Tracking efficiency correction for $D^0 \to K^-\pi^+$ with statistical errors.

p_T [MeV/c]	y [2,2.5[	[2.5,3[	[3,3.5[	[3.5,4[	[4,4.5[
[7000,8000[	1.0247 ± 0.0019	1.0195 ± 0.0013	1.0082 ± 0.0025	0.9979 ± 0.0026	0.9940 ± 0.0015
[6000,7000[	1.0317 ± 0.0027	1.0243 ± 0.0020	1.0122 ± 0.0033	1.0012 ± 0.0034	0.9958 ± 0.0021
[5000,6000[	1.0346 ± 0.0030	1.0278 ± 0.0027	1.0158 ± 0.0043	1.0045 ± 0.0043	0.9974 ± 0.0026
[4000,5000[	1.0382 ± 0.0034	1.0318 ± 0.0034	1.0205 ± 0.0055	1.0080 ± 0.0052	0.9997 ± 0.0032
[3000,4000[	1.0417 ± 0.0039	1.0374 ± 0.0049	1.0265 ± 0.0071	1.0141 ± 0.0069	1.0040 ± 0.0045
[2000,3000[	1.0445 ± 0.0046	1.0439 ± 0.0072	1.0349 ± 0.0099	1.0215 ± 0.0090	1.0103 ± 0.0065
[1000,2000[	1.0462 ± 0.0054	1.0504 ± 0.0104	1.0457 ± 0.0142	1.0314 ± 0.0125	1.0175 ± 0.0087
[0,1000[	1.0474 ± 0.0063	1.0544 ± 0.0129	1.0534 ± 0.0177	1.0397 ± 0.0156	1.0228 ± 0.0105

Table C.0.2: Tracking efficiency correction for $D^0 \to K^-\pi^+\pi^-\pi^+$ with statistical errors.

p_T [MeV/c]	y [2,2.5[	[2.5,3[	[3,3.5[	[3.5,4[	[4,4.5[
[7000,8000[	1.0235 ± 0.0018	1.0216 ± 0.0017	1.0150 ± 0.0046	0.9999 ± 0.0024	0.9947 ± 0.0016
[6000,7000[	1.0261 ± 0.0020	1.0230 ± 0.0018	1.0218 ± 0.0075	1.0083 ± 0.0058	0.9959 ± 0.0016
[5000,6000[	1.0280 ± 0.0022	1.0239 ± 0.0019	1.0231 ± 0.0081	1.0140 ± 0.0083	0.9980 ± 0.0019
[4000,5000[	1.0303 ± 0.0025	1.0251 ± 0.0021	1.0251 ± 0.0089	1.0193 ± 0.0104	1.0024 ± 0.0033
[3000,4000[	1.0335 ± 0.0029	1.0272 ± 0.0027	1.0277 ± 0.0099	1.0225 ± 0.0113	1.0094 ± 0.0061
[2000,3000[	1.0369 ± 0.0036	1.0317 ± 0.0047	1.0311 ± 0.0112	1.0251 ± 0.0117	1.0176 ± 0.0096
[1000,2000[	1.0388 ± 0.0036	1.0387 ± 0.0090	1.0339 ± 0.0119	1.0276 ± 0.0121	1.0221 ± 0.0115
[0,1000[	1.0420 ± 0.0040	1.0431 ± 0.0116	1.0352 ± 0.0116	1.0281 ± 0.0120	1.0220 ± 0.0114

Table C.0.3: Tracking efficiency correction for $D^{*+} \to \left(D^0 \to K^-\pi^+\right)\pi^+$ with statistical errors.

p_T [MeV/c]	y [2,2.5[	[2.5,3[	[3,3.5[	[3.5,4[	[4,4.5[
[7000,8000[	1.0184 ± 0.0012	1.0126 ± 0.0008	1.0001 ± 0.0009	0.9913 ± 0.0010	0.9922 ± 0.0015
[6000,7000[	1.0256 ± 0.0020	1.0160 ± 0.0010	1.0023 ± 0.0013	0.9923 ± 0.0012	0.9918 ± 0.0012
[5000,6000[	1.0293 ± 0.0024	1.0188 ± 0.0014	1.0044 ± 0.0016	0.9936 ± 0.0014	0.9916 ± 0.0011
[4000,5000[	1.0337 ± 0.0029	1.0231 ± 0.0020	1.0076 ± 0.0022	0.9961 ± 0.0018	0.9925 ± 0.0013
[3000,4000[	1.0387 ± 0.0035	1.0292 ± 0.0032	1.0130 ± 0.0035	0.9994 ± 0.0023	0.9939 ± 0.0016
[2000,3000[	1.0433 ± 0.0043	1.0374 ± 0.0056	1.0217 ± 0.0061	1.0056 ± 0.0037	0.9972 ± 0.0024
[1000,2000[	1.0465 ± 0.0057	1.0470 ± 0.0096	1.0339 ± 0.0105	1.0143 ± 0.0062	1.0019 ± 0.0034
[0,1000[	1.0478 ± 0.0067	1.0541 ± 0.0137	1.0447 ± 0.0152	1.0215 ± 0.0087	1.0046 ± 0.0039

Table C.0.4: Tracking efficiency correction for $D^+ \to K^-K^+\pi^+$ with statistical errors.

p_T [MeV/c]	y [2,2.5[	[2.5,3[	[3,3.5[	[3.5,4[	[4,4.5[
[7000,8000[	1.0198 ± 0.0014	1.0153 ± 0.0011	1.0040 ± 0.0015	0.9947 ± 0.0016	0.9938 ± 0.0016
[6000,7000[	1.0256 ± 0.0019	1.0192 ± 0.0016	1.0065 ± 0.0021	0.9962 ± 0.0020	0.9945 ± 0.0016
[5000,6000[	1.0292 ± 0.0023	1.0216 ± 0.0020	1.0086 ± 0.0024	0.9980 ± 0.0024	0.9948 ± 0.0017
[4000,5000[	1.0332 ± 0.0028	1.0248 ± 0.0026	1.0124 ± 0.0033	1.0003 ± 0.0028	0.9963 ± 0.0022
[3000,4000[	1.0384 ± 0.0035	1.0298 ± 0.0038	1.0166 ± 0.0042	1.0045 ± 0.0037	0.9987 ± 0.0029
[2000,3000[	1.0434 ± 0.0045	1.0365 ± 0.0055	1.0233 ± 0.0058	1.0107 ± 0.0052	1.0030 ± 0.0042
[1000,2000[	1.0459 ± 0.0053	1.0442 ± 0.0078	1.0320 ± 0.0083	1.0183 ± 0.0073	1.0074 ± 0.0054
[0,1000[	1.0456 ± 0.0050	1.0489 ± 0.0094	1.0392 ± 0.0108	1.0239 ± 0.0091	1.0095 ± 0.0058

Table C.0.5: Tracking efficiency correction for $D^+ \to K^-\pi^+\pi^+$ with statistical errors.

p_{T} [MeV/c]	y [2,2.5[	[2.5,3[	[3,3.5[	[3.5,4[	[4,4.5[
[7000,8000[	1.0190 ± 0.0013	1.0136 ± 0.0008	1.0013 ± 0.0012	0.9928 ± 0.0012	0.9926 ± 0.0015
[6000,7000[	1.0257 ± 0.0020	1.0171 ± 0.0012	1.0039 ± 0.0016	0.9937 ± 0.0014	0.9925 ± 0.0013
[5000,6000[	1.0293 ± 0.0024	1.0200 ± 0.0015	1.0061 ± 0.0021	0.9953 ± 0.0017	0.9922 ± 0.0012
[4000,5000[	1.0337 ± 0.0029	1.0239 ± 0.0022	1.0093 ± 0.0028	0.9978 ± 0.0022	0.9933 ± 0.0014
[3000,4000[	1.0383 ± 0.0034	1.0292 ± 0.0033	1.0147 ± 0.0042	1.0015 ± 0.0030	0.9951 ± 0.0019
[2000,3000[	1.0431 ± 0.0044	1.0369 ± 0.0057	1.0223 ± 0.0063	1.0072 ± 0.0044	0.9987 ± 0.0027
[1000,2000[	1.0464 ± 0.0057	1.0456 ± 0.0092	1.0330 ± 0.0103	1.0155 ± 0.0068	1.0031 ± 0.0039
[0,1000[	1.0476 ± 0.0065	1.0520 ± 0.0126	1.0418 ± 0.0140	1.0211 ± 0.0087	1.0060 ± 0.0047

Table C.0.6: Tracking efficiency correction for $D_s^+ \to (\phi \to K^- K^+)\pi^+$ with statistical errors.

D

Binned fits

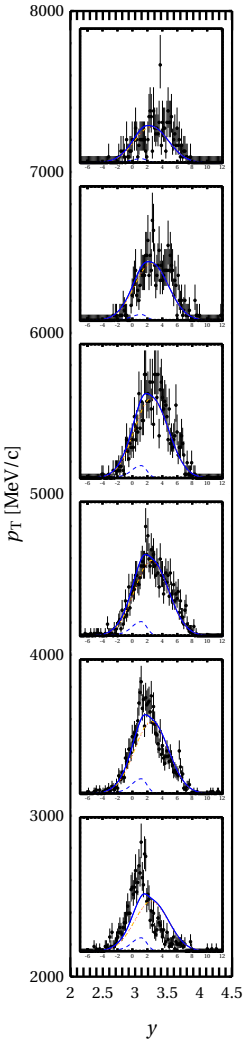

Figure D.0.1: Fitted impact parameter χ^2 distribution of Λ_c^+in $\Lambda_c^+ \to pK^-\pi^+$

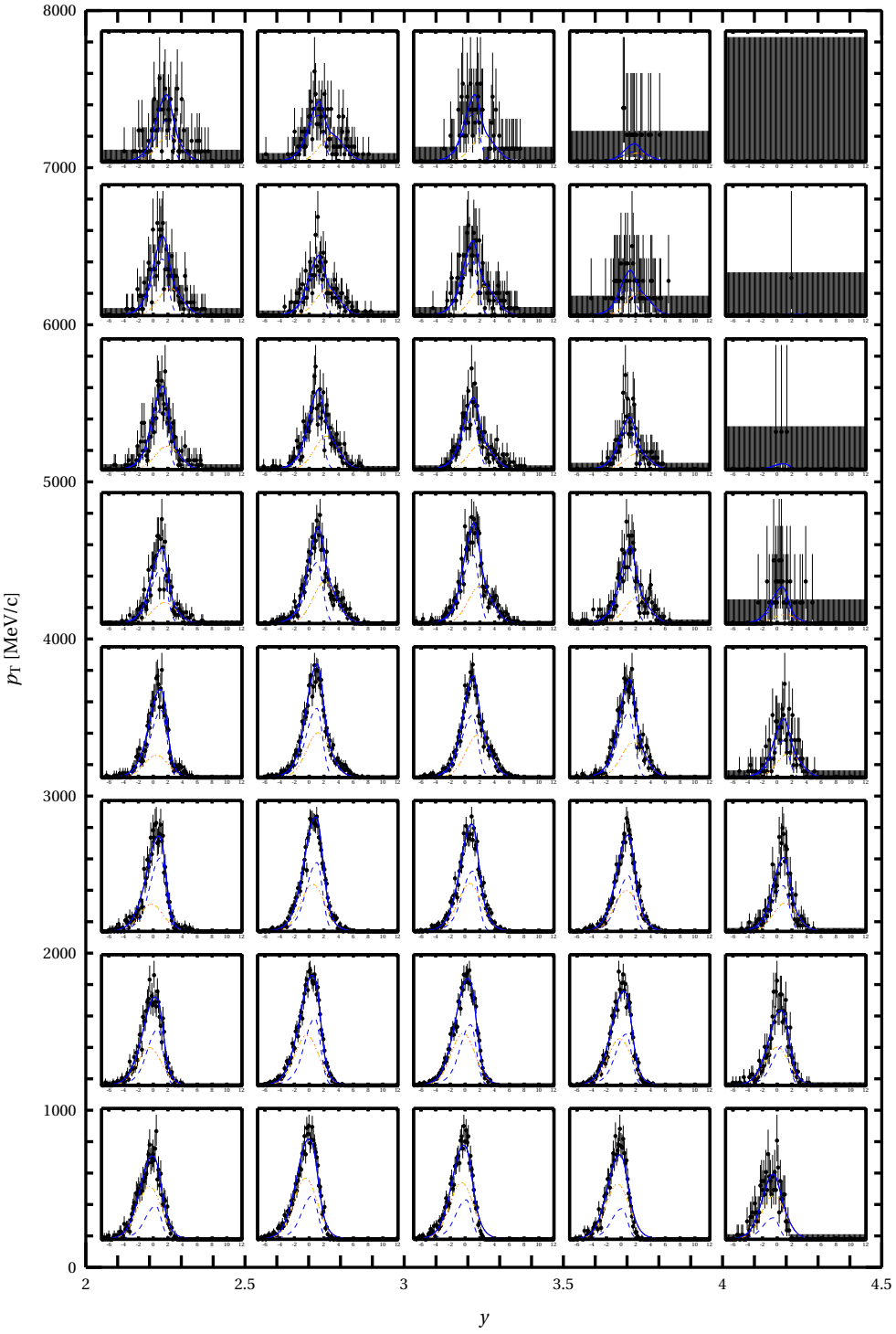

Figure D.0.2: Fitted impact parameter χ^2 distribution of D^0 in $D^0 \to K^-\pi^+$

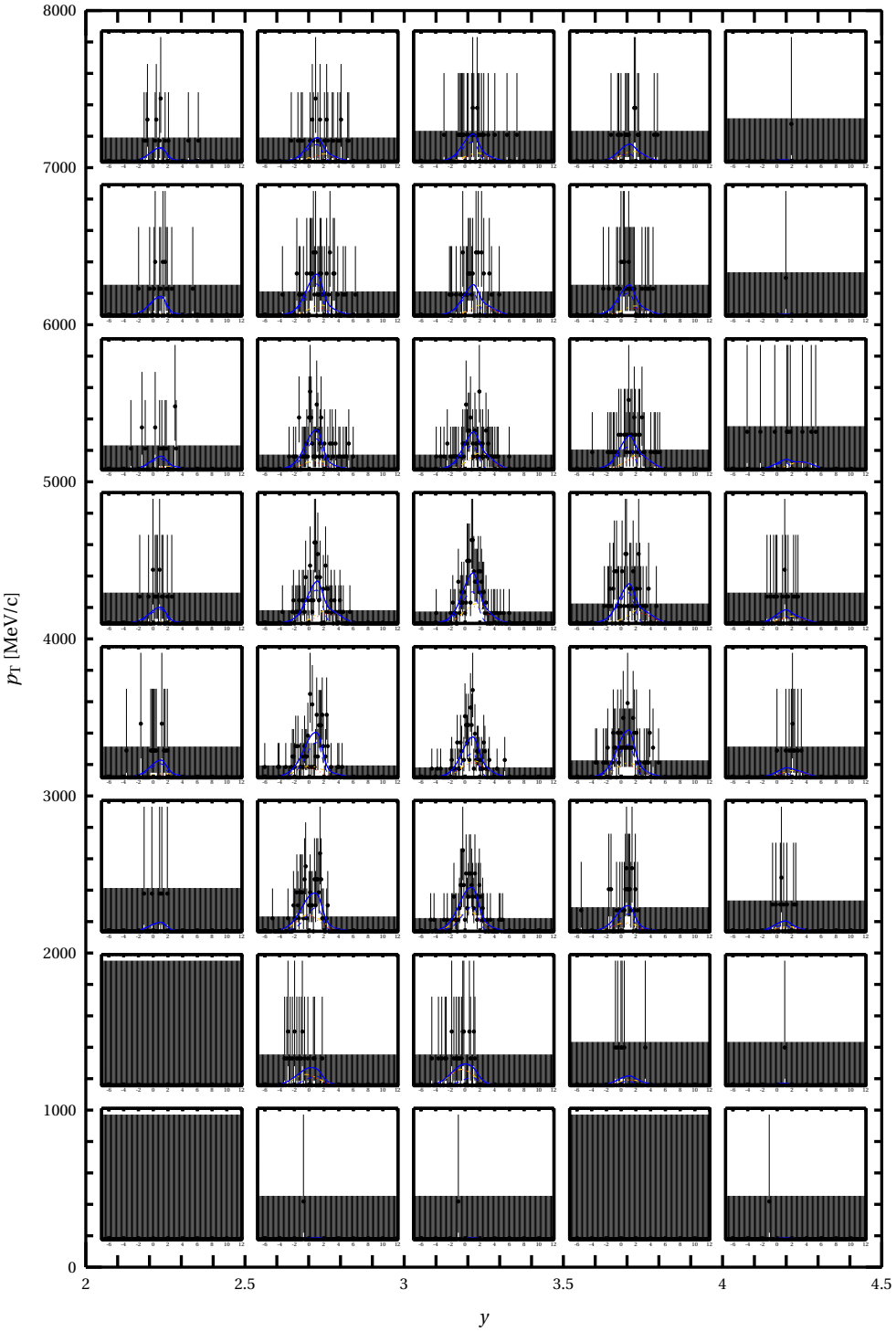

Figure D.0.3: Fitted impact parameter χ^2 distribution of D^0 in $D^0 \to K^-\pi^+\pi^-\pi^+$

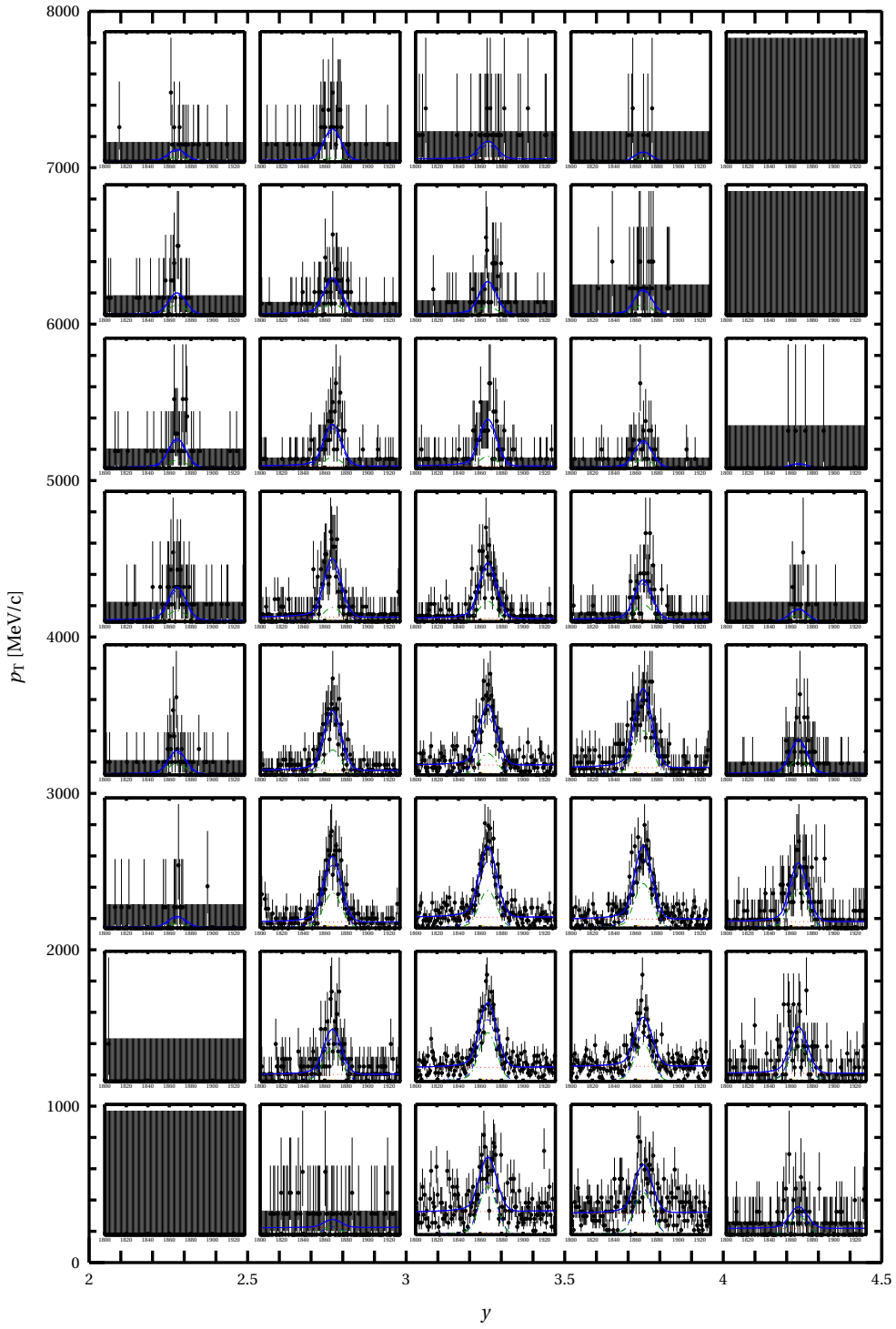

Figure D.0.4: Fitted distribution of $m\left(D^{*+}\right)$ in $D^{*+} \to \left(D^0 \to K^- \pi^+\right) \pi^+$

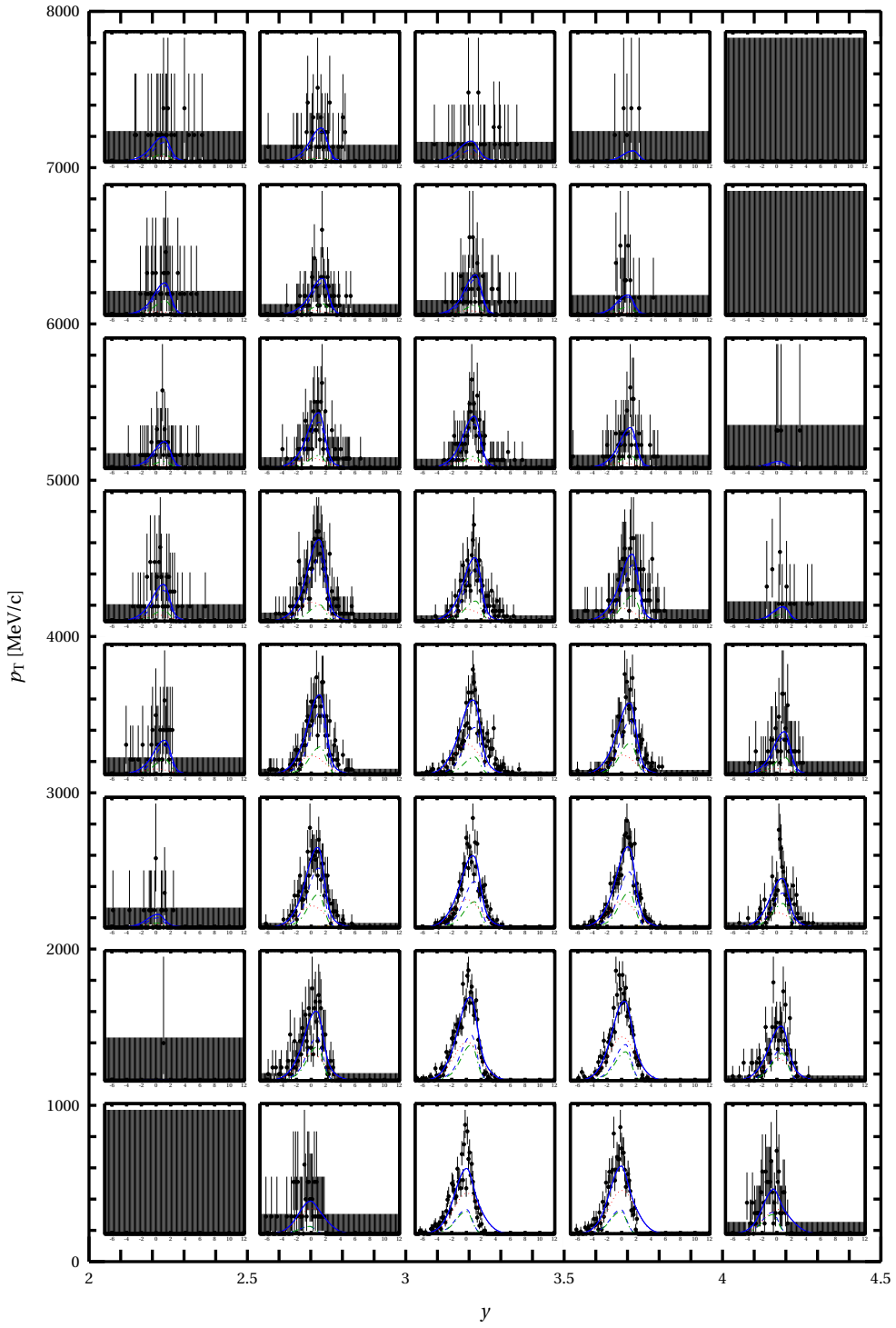

Figure D.0.5: Fitted impact parameter χ^2 distribution of D^{*+} in $D^{*+} \to \left(D^0 \to K^- \pi^+\right) \pi^+$

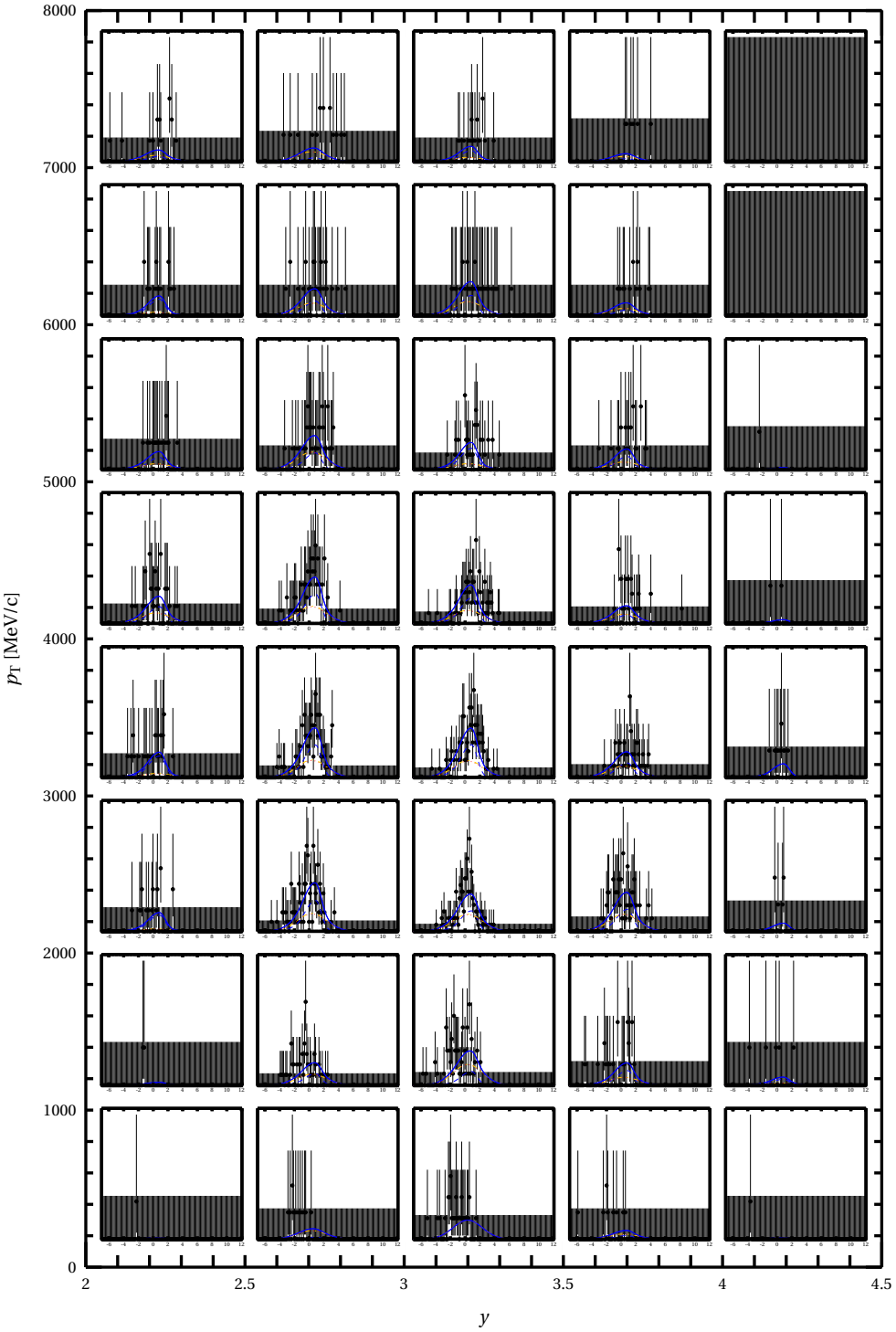

Figure D.0.6: Fitted impact parameter χ^2 distribution of D^+ in $D^+ \to K^- K^+ \pi^+$

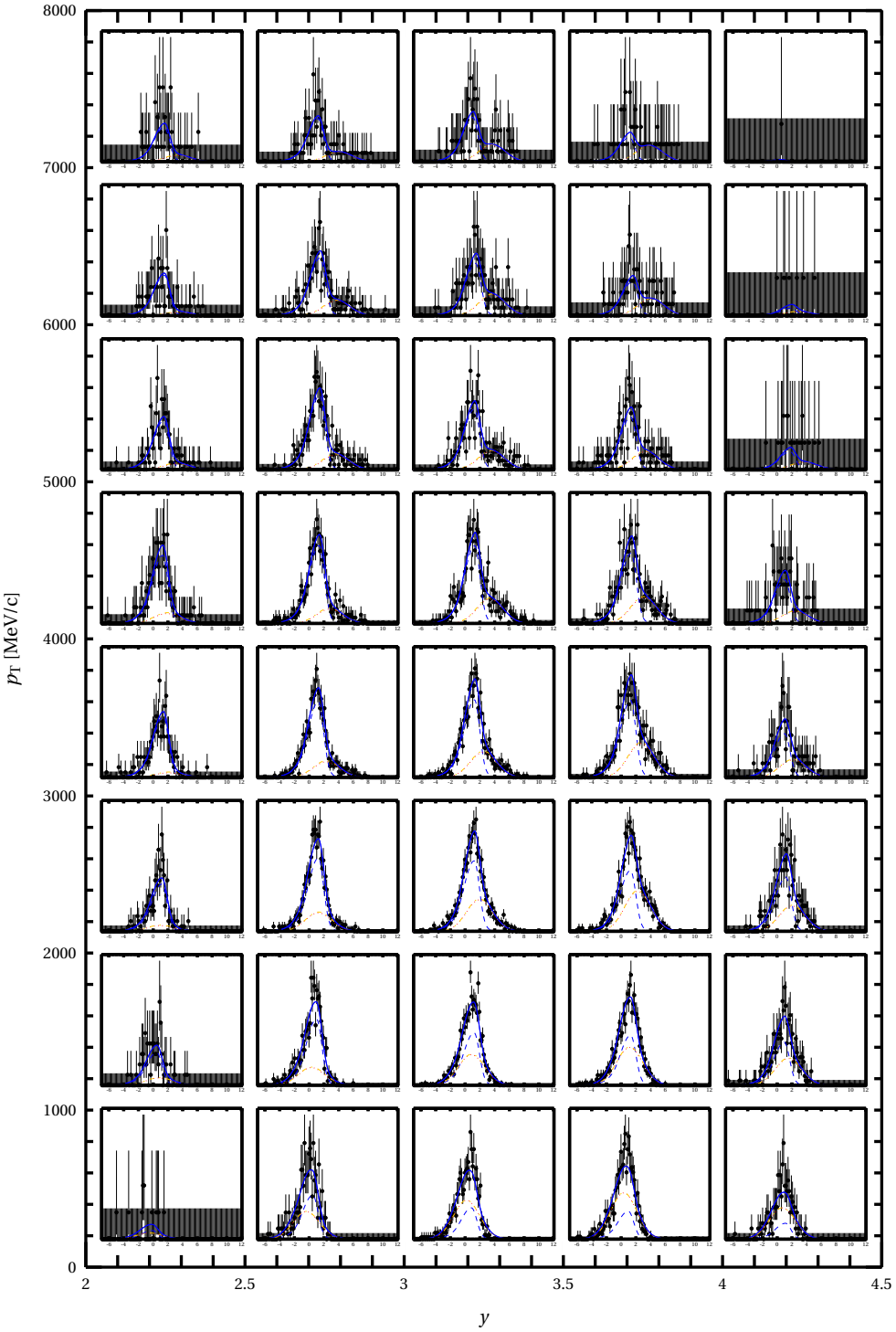

Figure D.0.7: Fitted impact parameter χ^2 distribution of D^+ in $D^+ \to K^-\pi^+\pi^+$

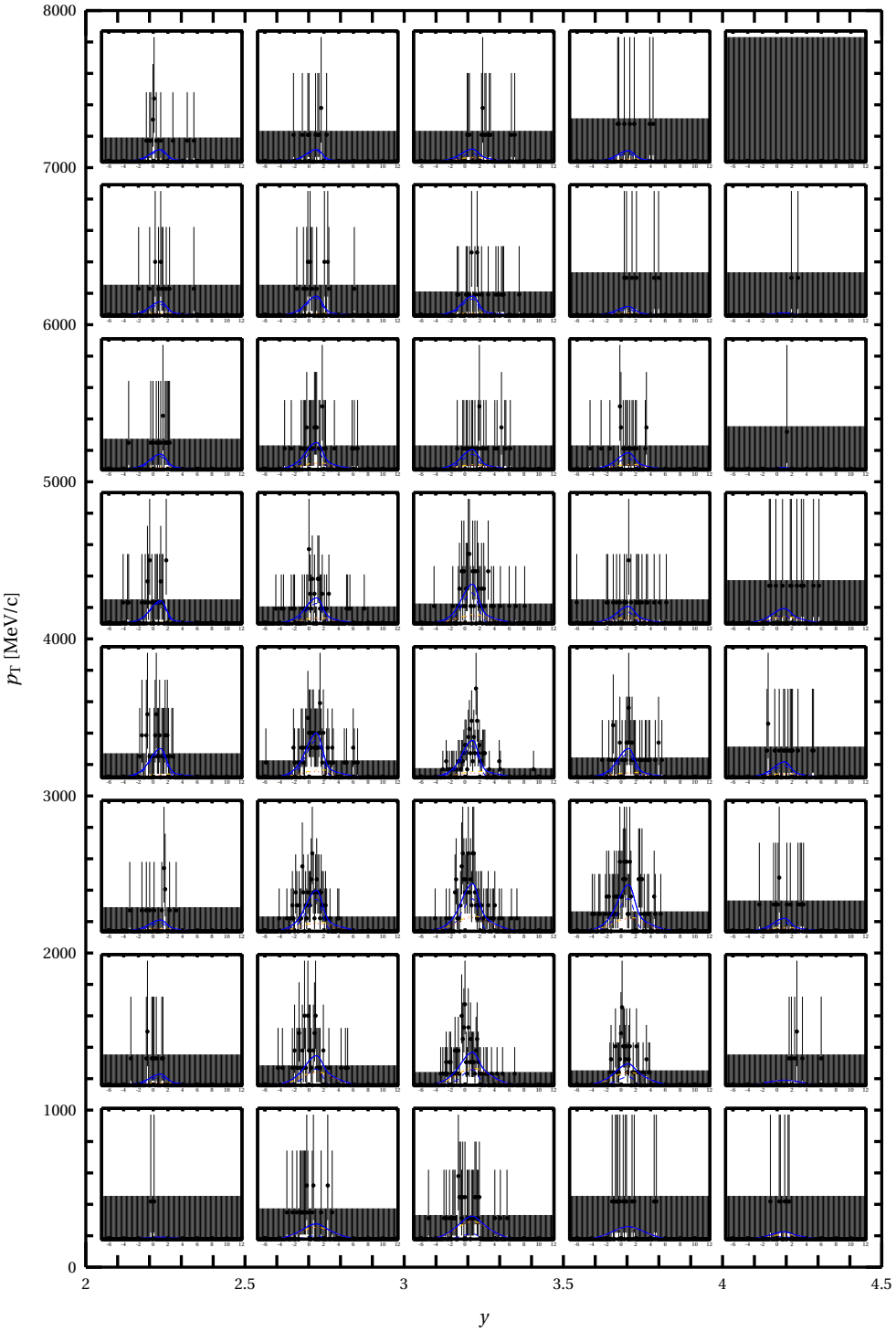

Figure D.0.8: Fitted impact parameter χ^2 distribution of D_s^+ in $D_s^+ \to (\phi \to K^- K^+)\pi^+$

E

Efficiency tables

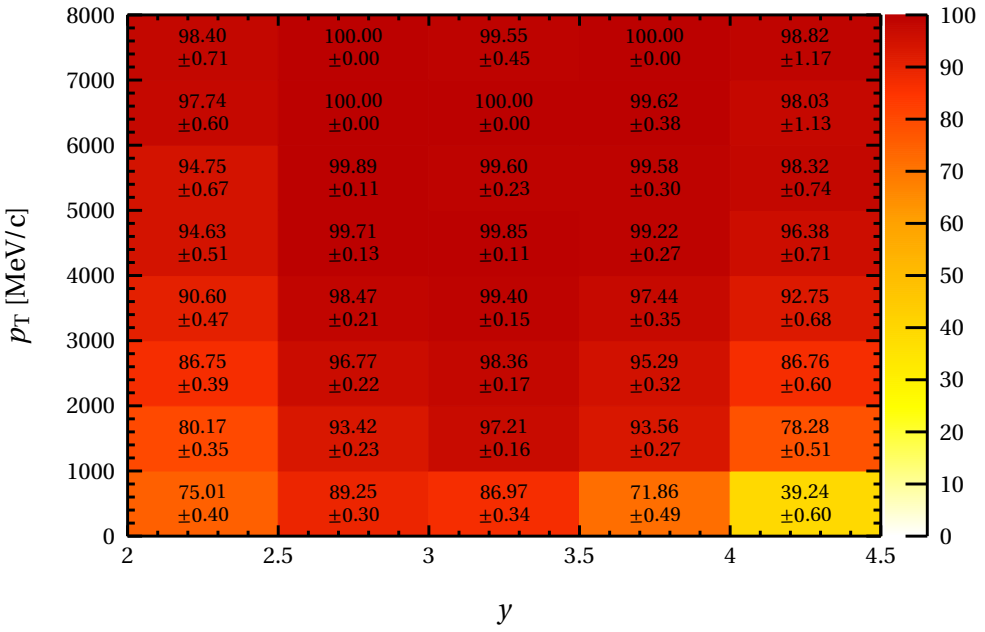

(a) Detector acceptance efficiency of $D^0 \to K^-\pi^+$ decays

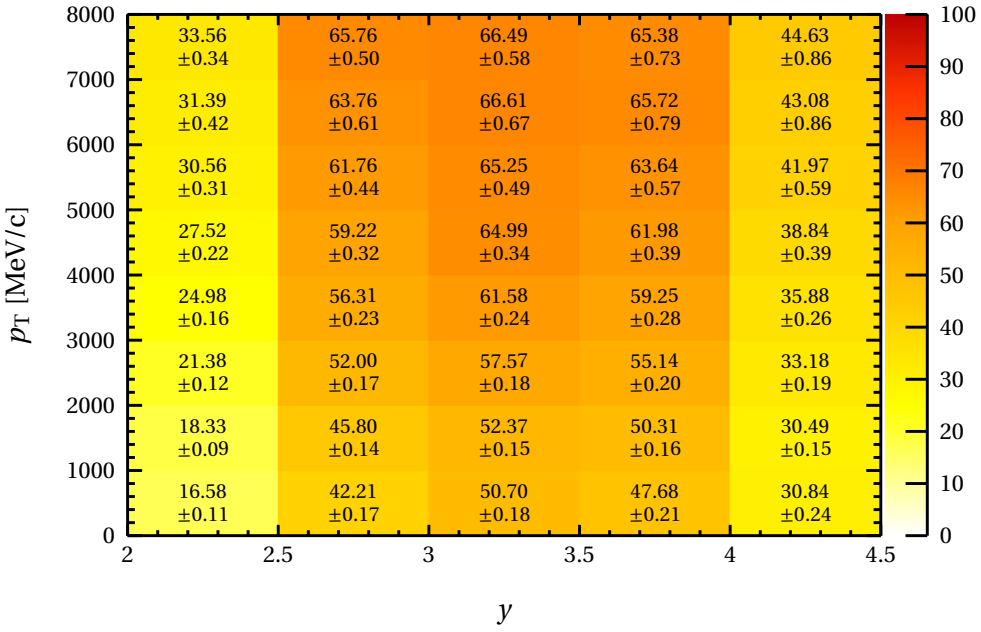

(b) Mother reconstruction efficiency for $D^0 \to K^-\pi^+$ decays

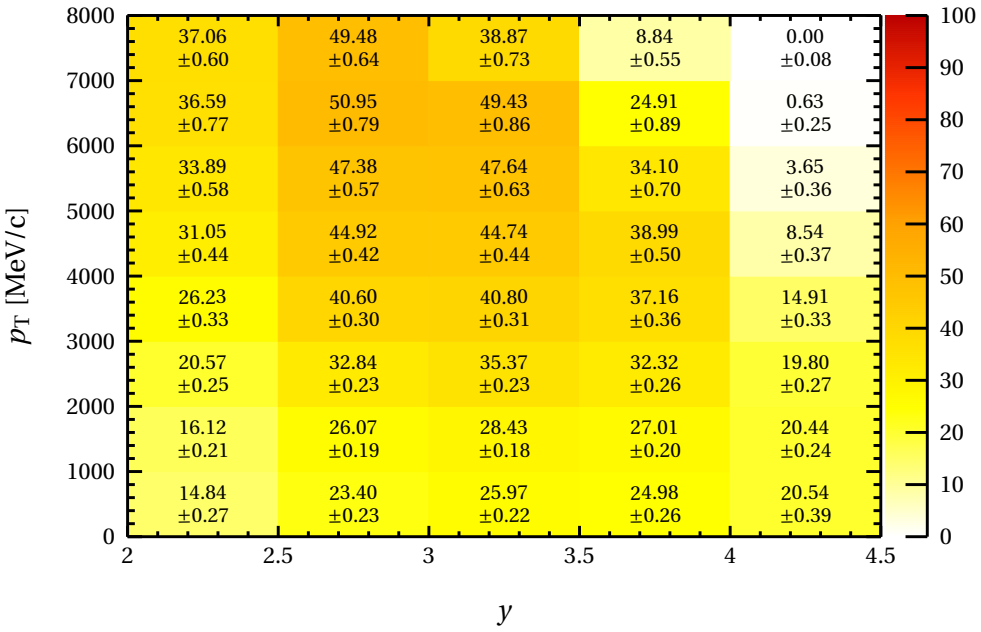

(c) Candidate preselection efficiency for $D^0 \to K^-\pi^+$ decays

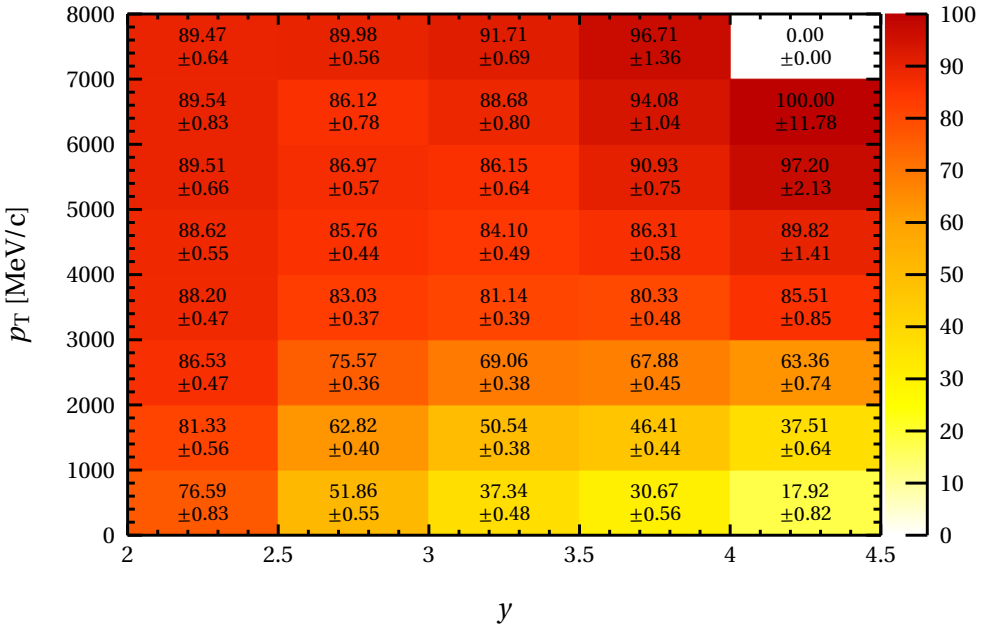

(d) Candidate BDT selection efficiency for $D^0 \to K^-\pi^+$ decays

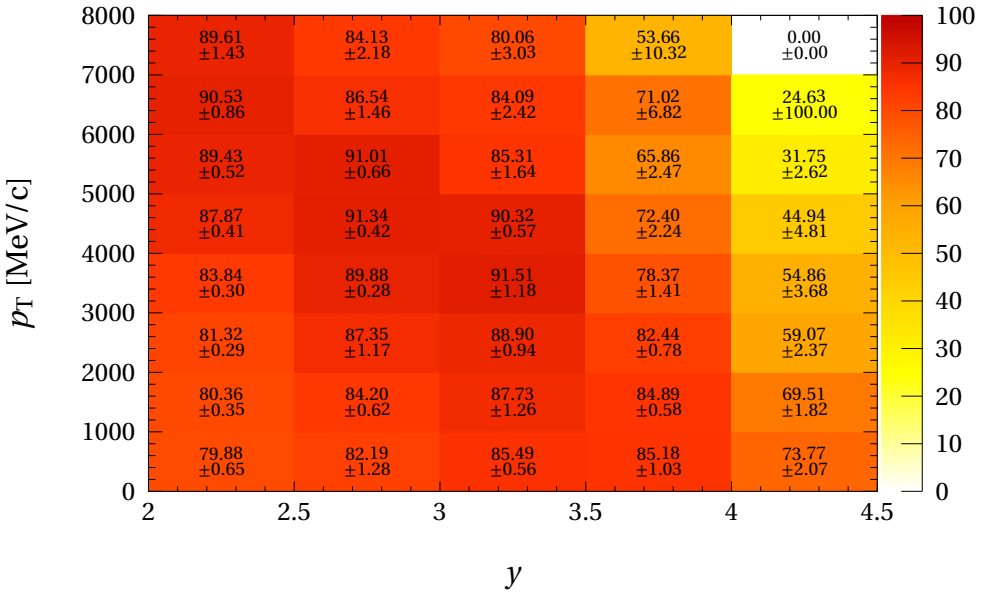

(e) Candidate particle identification selection efficiency for $D^0 \to K^-\pi^+$ decays

Figure E.0.1: Efficiency chain for $D^0 \to K^-\pi^+$ decays

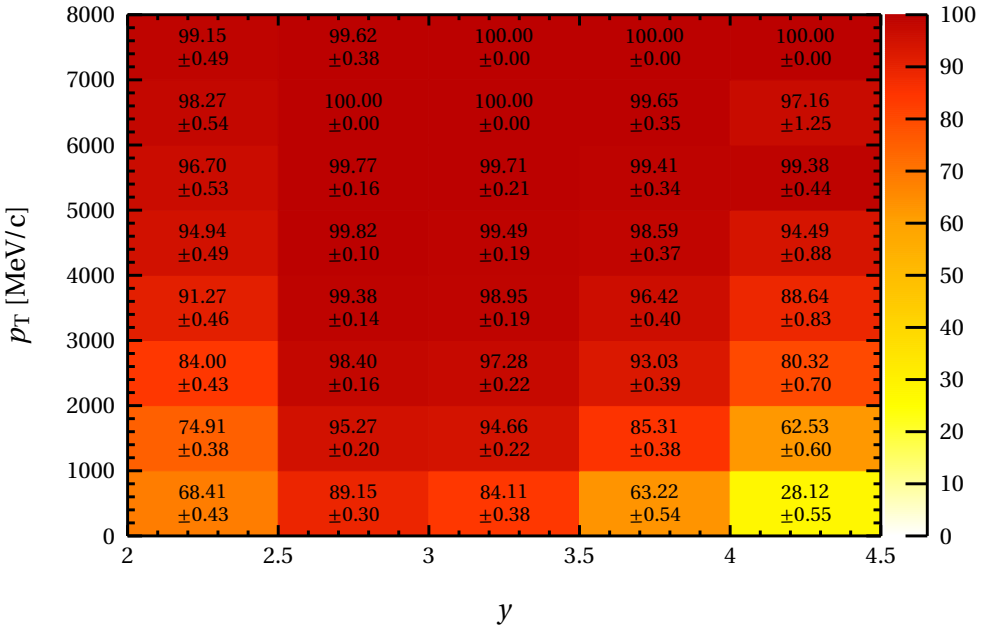

(a) Detector acceptance efficiency of $D^0 \to K^-\pi^+\pi^-\pi^+$ decays

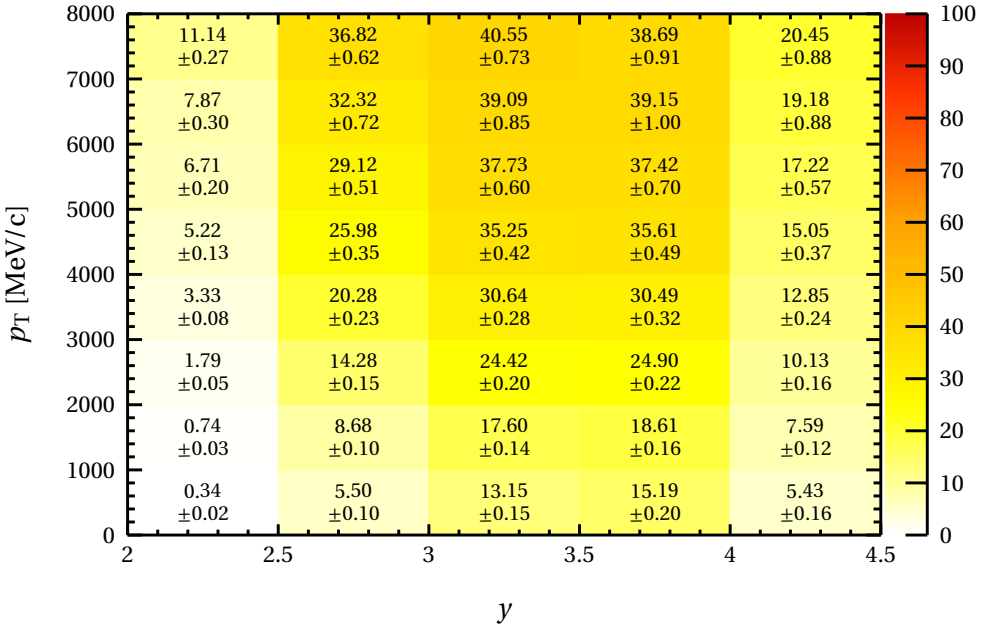

(b) Mother reconstruction efficiency for $D^0 \to K^-\pi^+\pi^-\pi^+$ decays

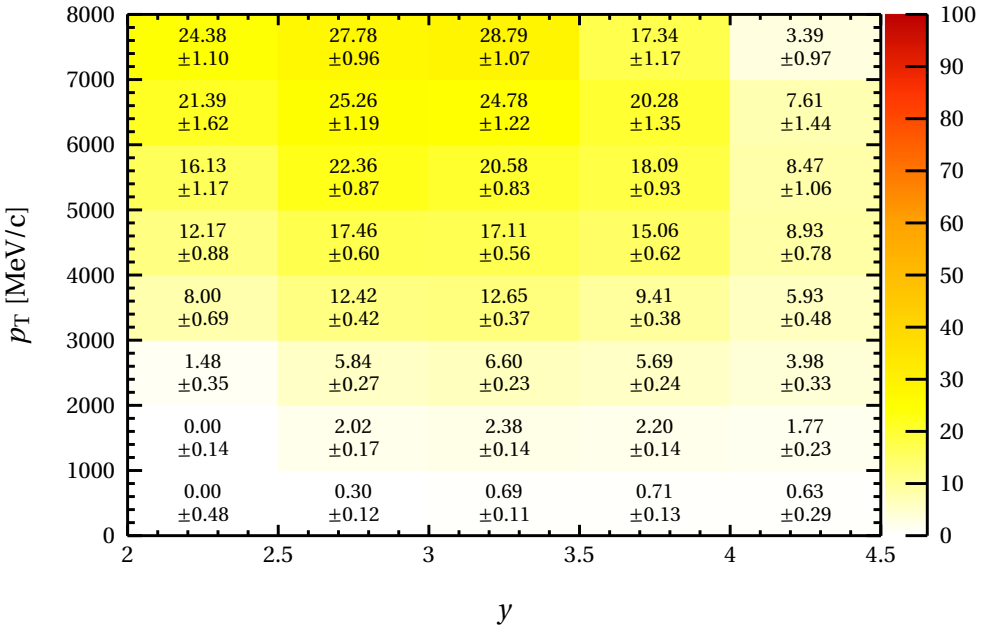

(c) Candidate preselection efficiency for $D^0 \to K^-\pi^+\pi^-\pi^+$ decays

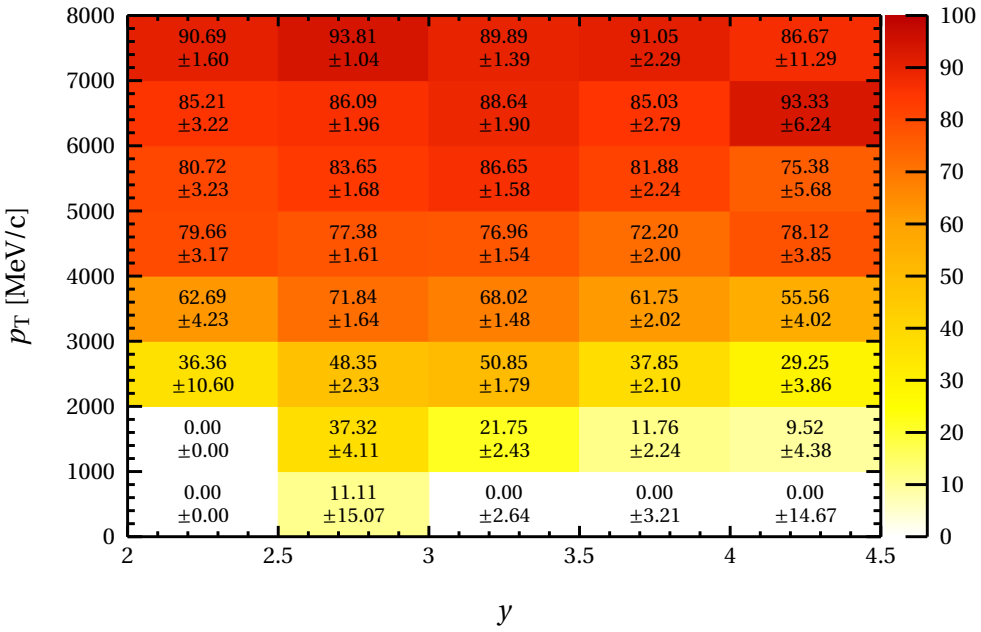

(d) Candidate BDT selection efficiency for $D^0 \to K^-\pi^+\pi^-\pi^+$ decays

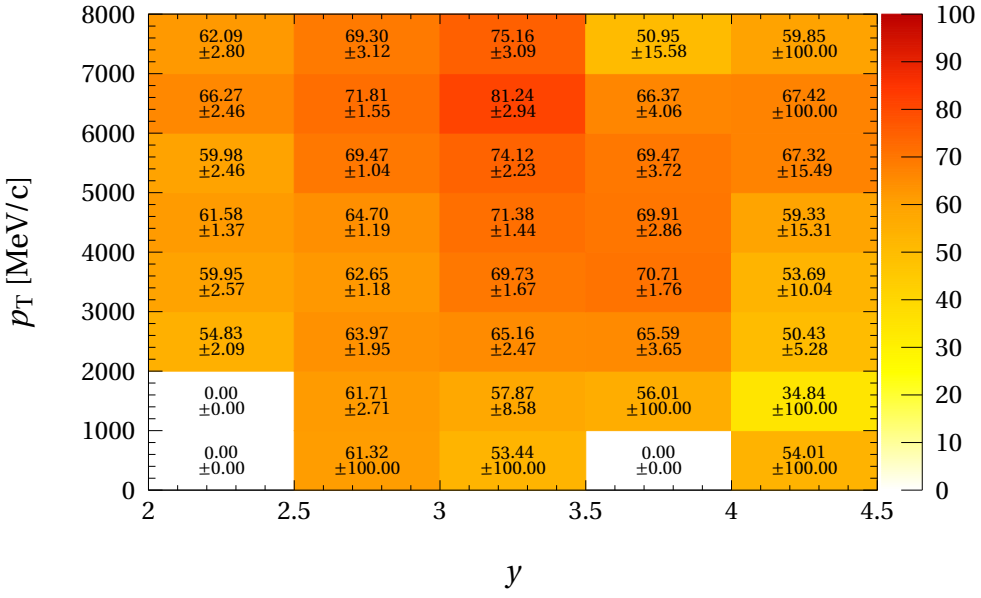

(e) Candidate particle identification selection efficiency for $D^0 \to K^-\pi^+\pi^-\pi^+$ decays

Figure E.0.2: Efficiency chain for $D^0 \to K^-\pi^+\pi^-\pi^+$ decays

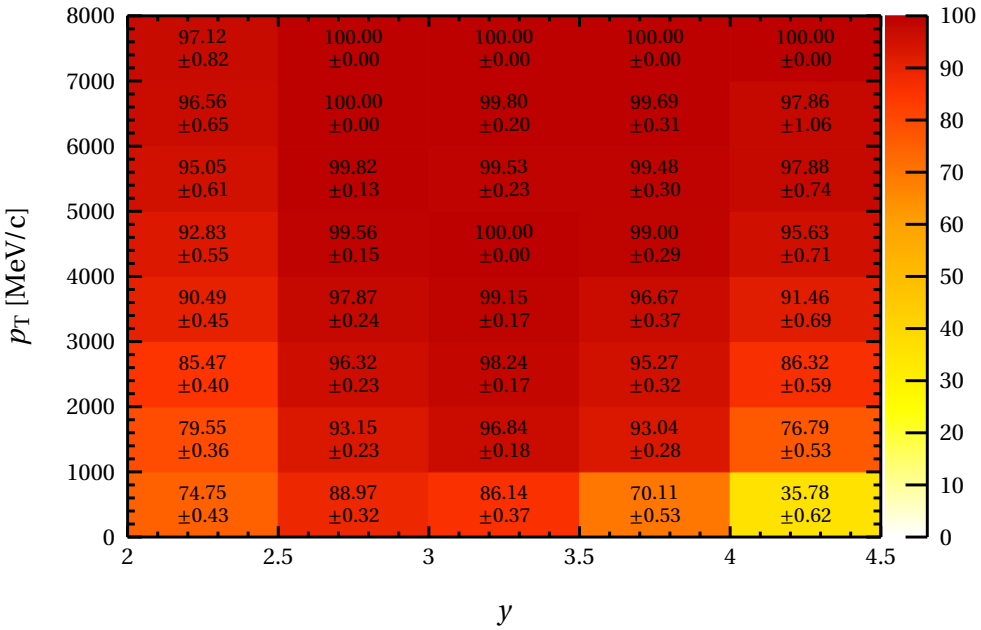

(a) Detector acceptance efficiency of $D^{*+} \to \left(D^0 \to K^-\pi^+\right)\pi^+$ decays

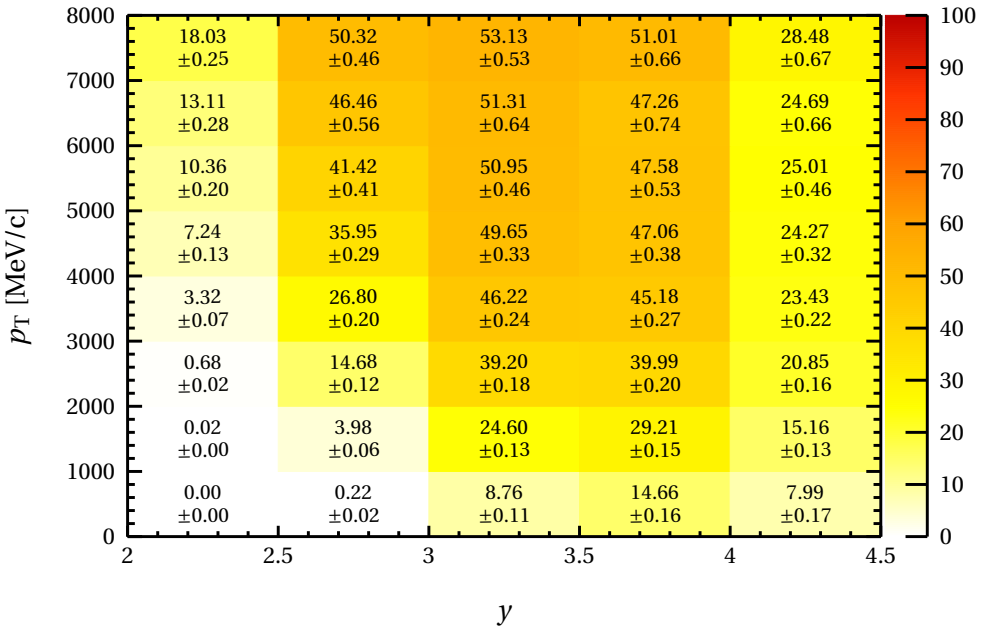

(b) Mother reconstruction efficiency for $D^{*+} \to \left(D^0 \to K^- \pi^+\right) \pi^+$ decays

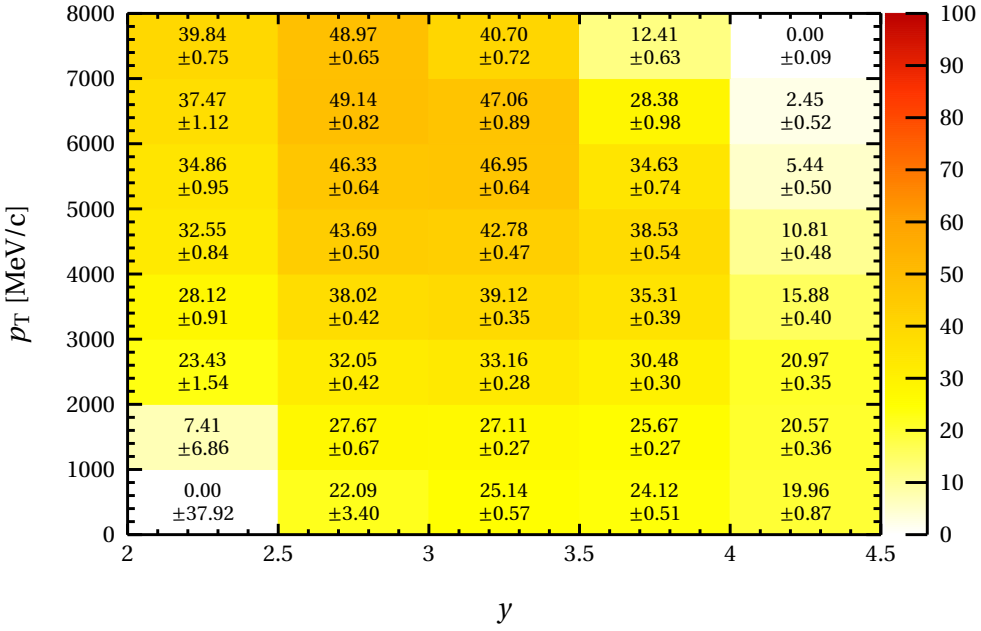

(c) Candidate preselection efficiency for $D^{*+} \to \left(D^0 \to K^- \pi^+\right) \pi^+$ decays

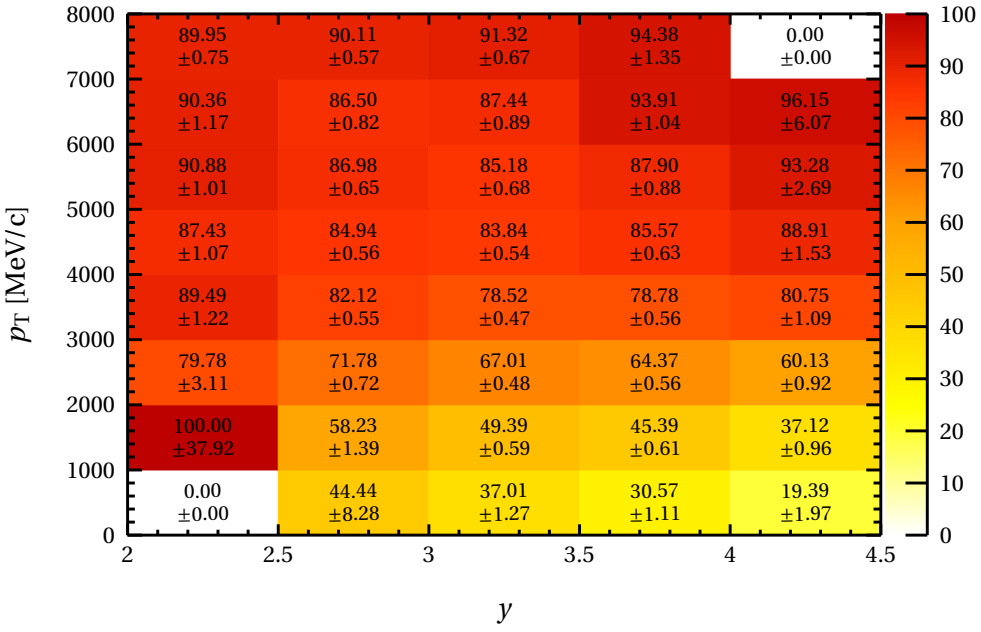

(d) Candidate BDT selection efficiency for $D^{*+} \to \left(D^0 \to K^-\pi^+\right)\pi^+$ decays

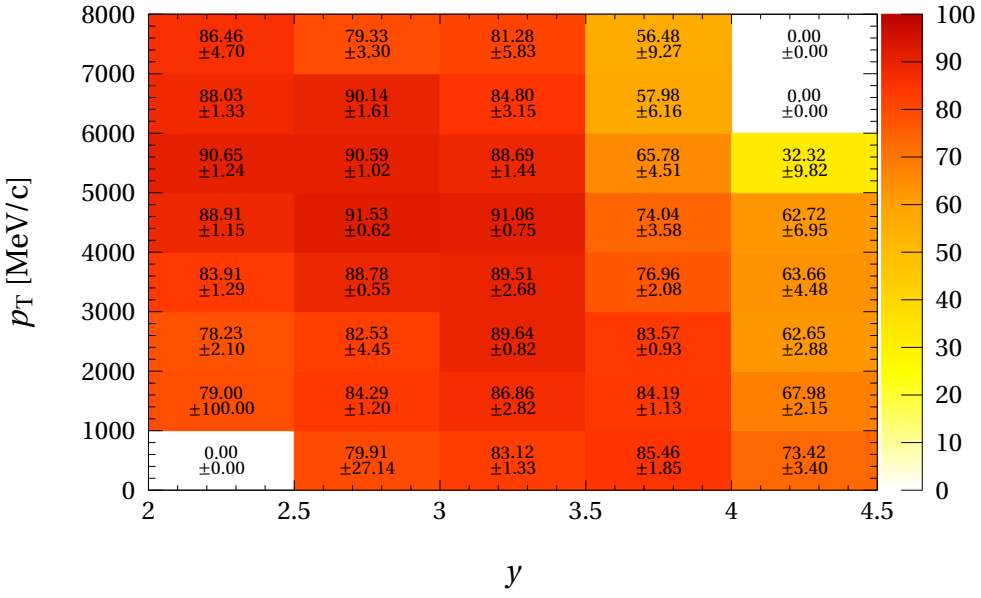

(e) Candidate particle identification selection efficiency for $D^{*+} \to \left(D^0 \to K^-\pi^+\right)\pi^+$ decays

Figure E.0.3: Efficiency chain for $D^{*+} \to \left(D^0 \to K^-\pi^+\right)\pi^+$ decays

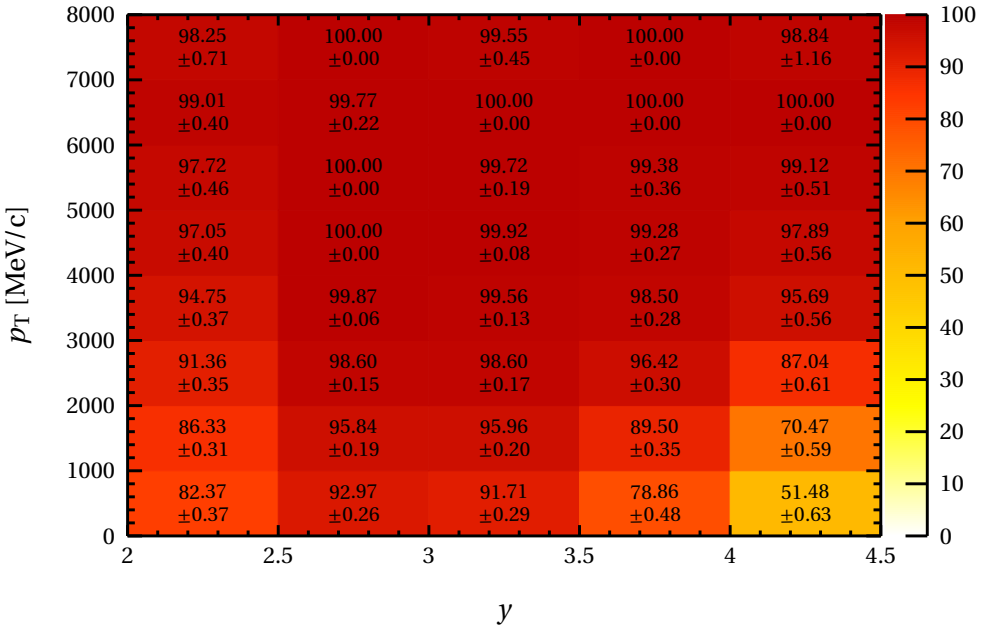

(a) Detector acceptance efficiency of $D^+ \to K^- K^+ \pi^+$ decays

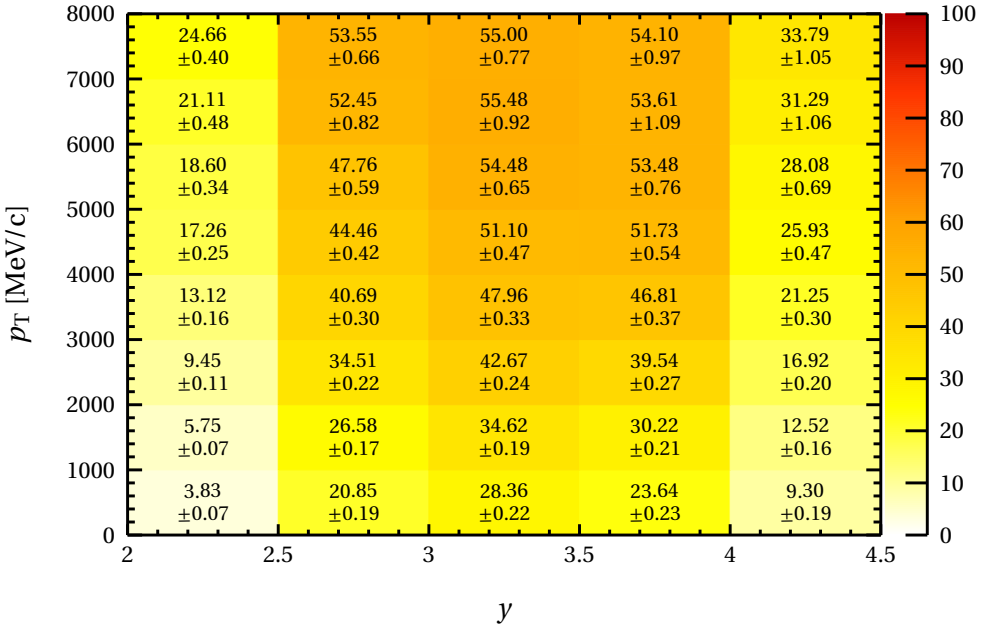

(b) Mother reconstruction efficiency for $D^+ \to K^- K^+ \pi^+$ decays

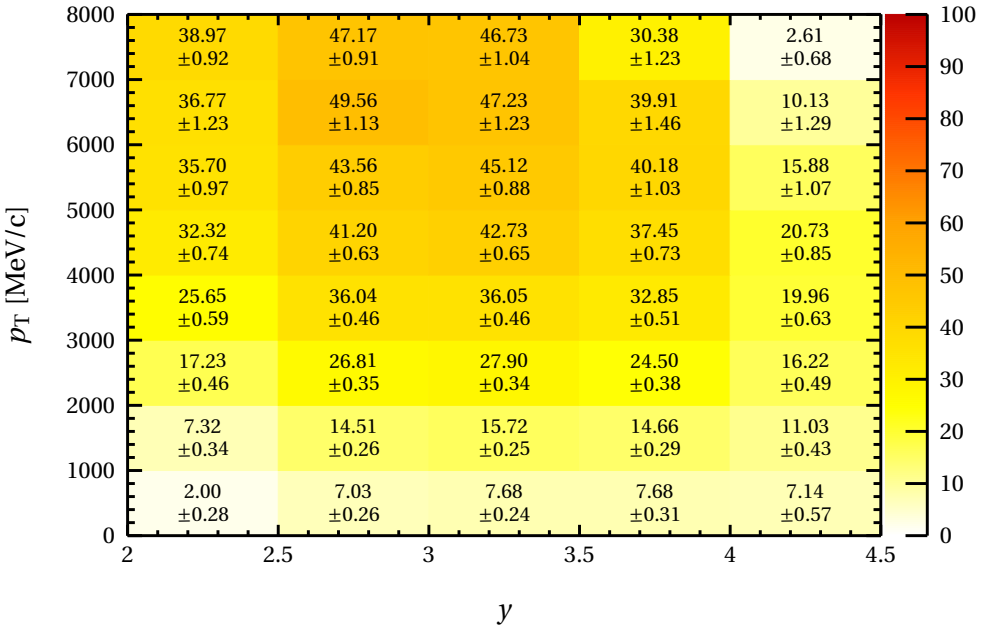

(c) Candidate preselection efficiency for $D^+ \to K^-K^+\pi^+$ decays

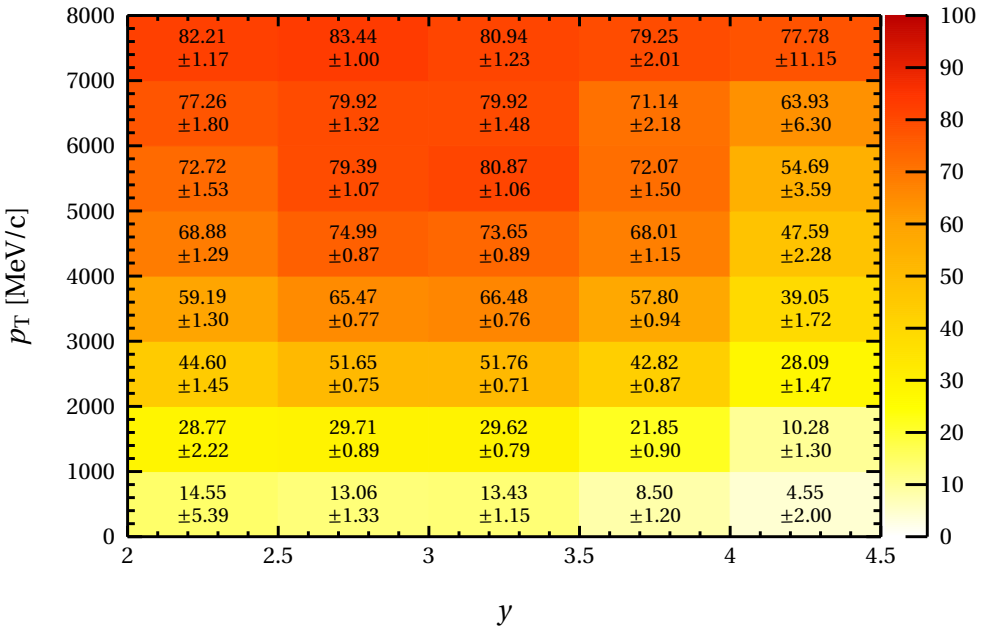

(d) Candidate BDT selection efficiency for $D^+ \to K^-K^+\pi^+$ decays

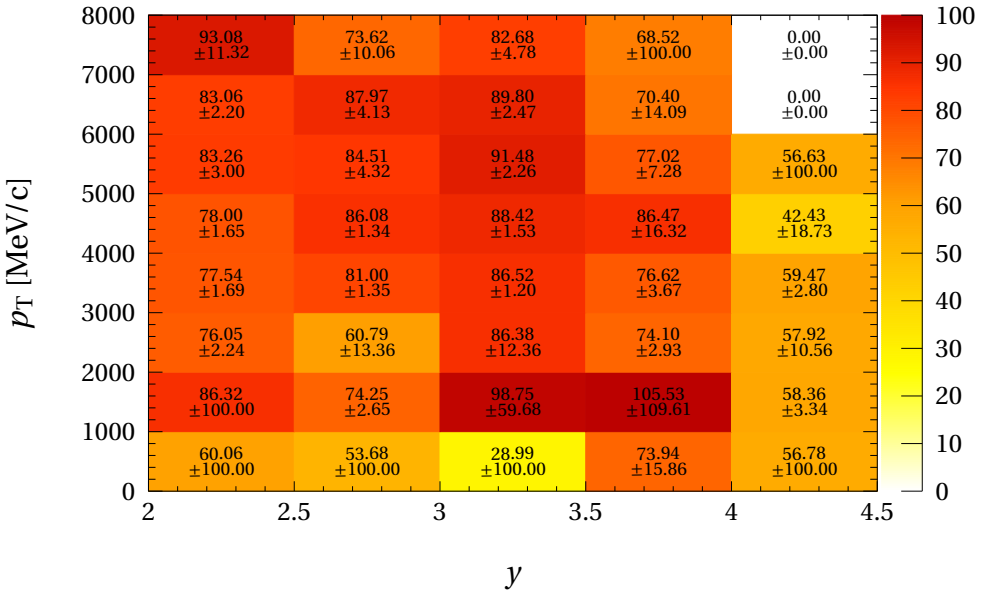

(e) Candidate particle identification selection efficiency for $D^+ \to K^-K^+\pi^+$ decays

Figure E.0.4: Efficiency chain for $D^+ \to K^-K^+\pi^+$ decays

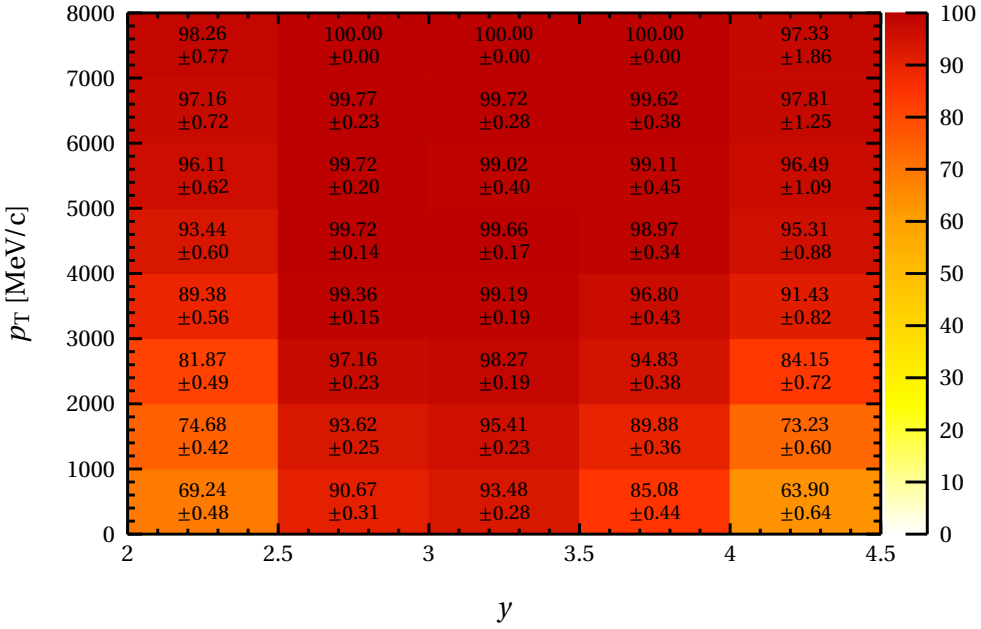

(a) Detector acceptance efficiency of $D^+ \to K^-\pi^+\pi^+$ decays

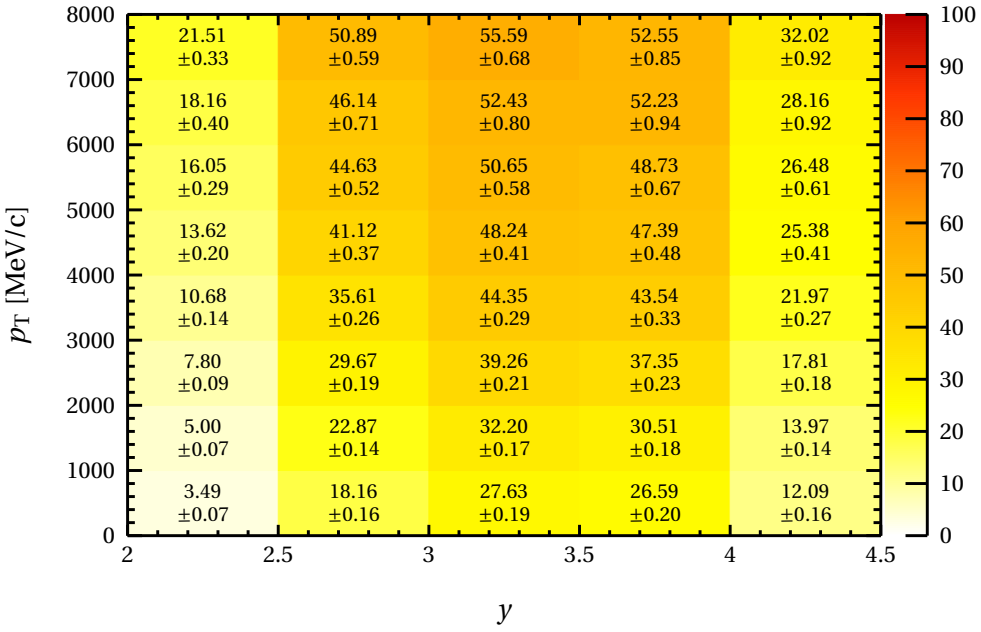

(b) Mother reconstruction efficiency for $D^+ \to K^-\pi^+\pi^+$ decays

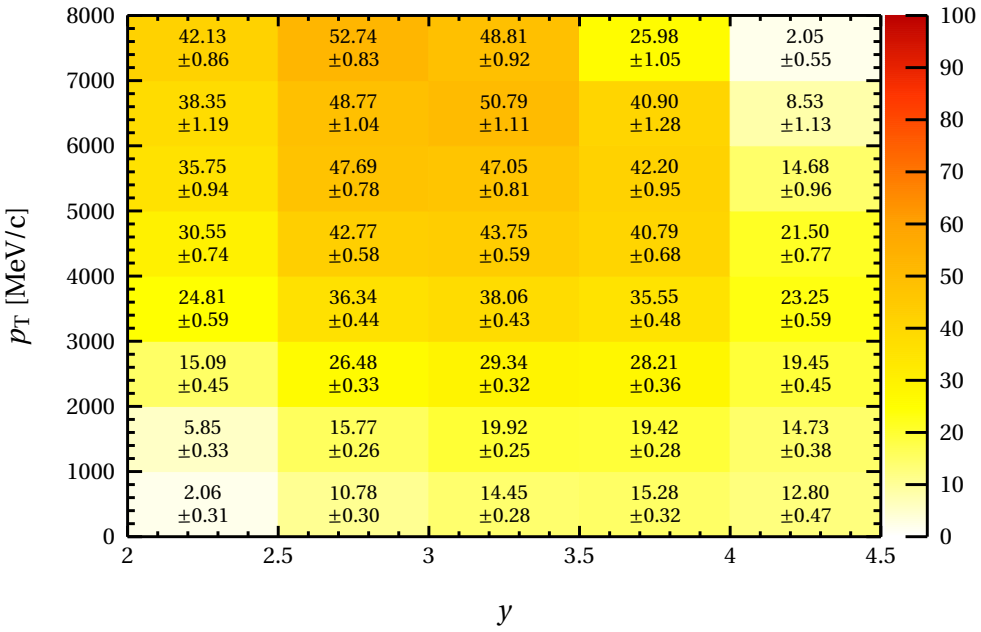

(c) Candidate preselection efficiency for $D^+ \to K^-\pi^+\pi^+$ decays

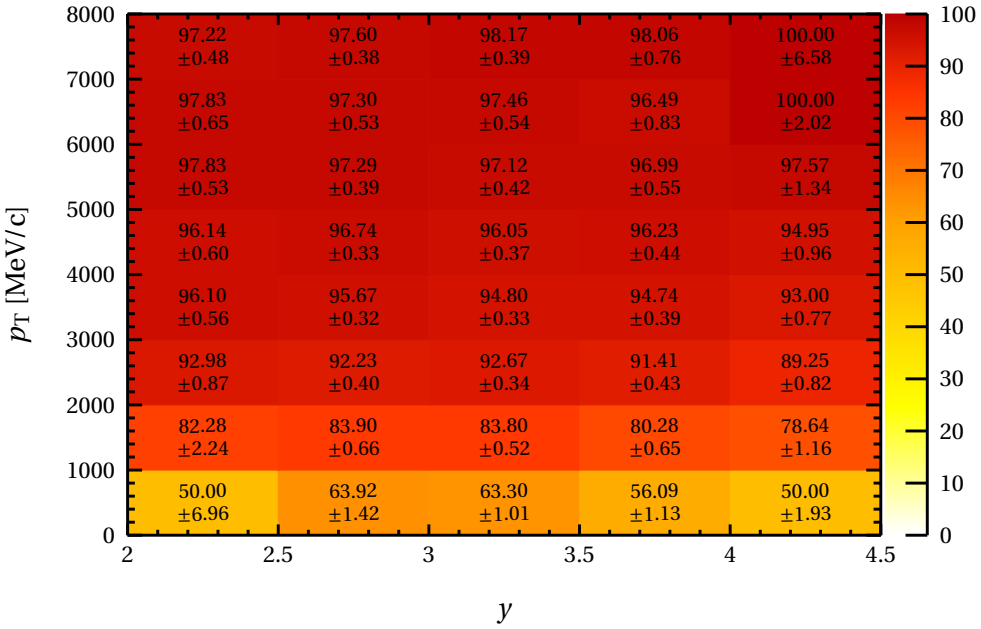

(d) Candidate BDT selection efficiency for $D^+ \to K^-\pi^+\pi^+$ decays

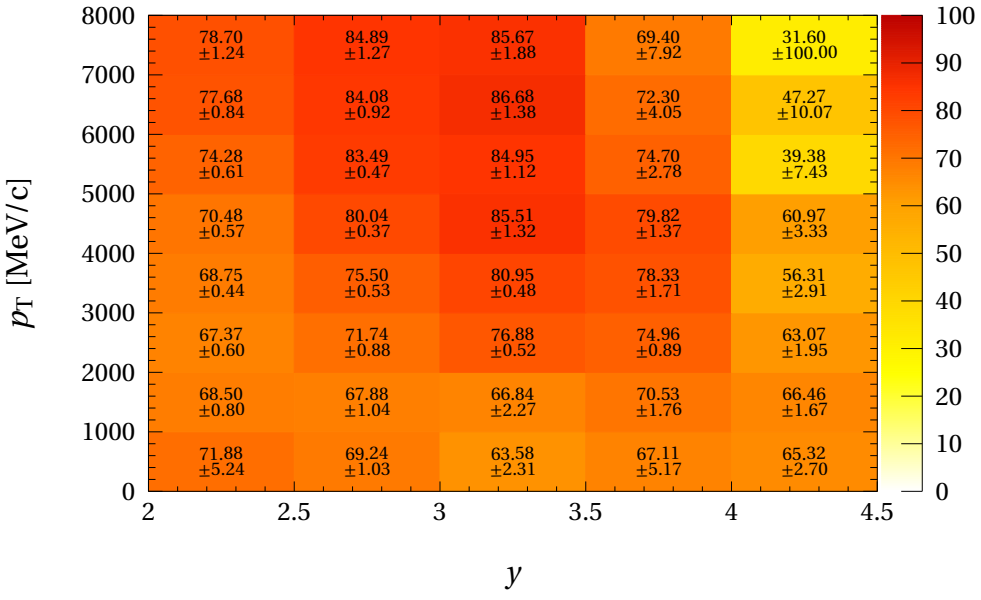

(e) Candidate particle identification selection efficiency for $D^+ \to K^-\pi^+\pi^+$ decays

Figure E.0.5: Efficiency chain for $D^+ \to K^-\pi^+\pi^+$ decays

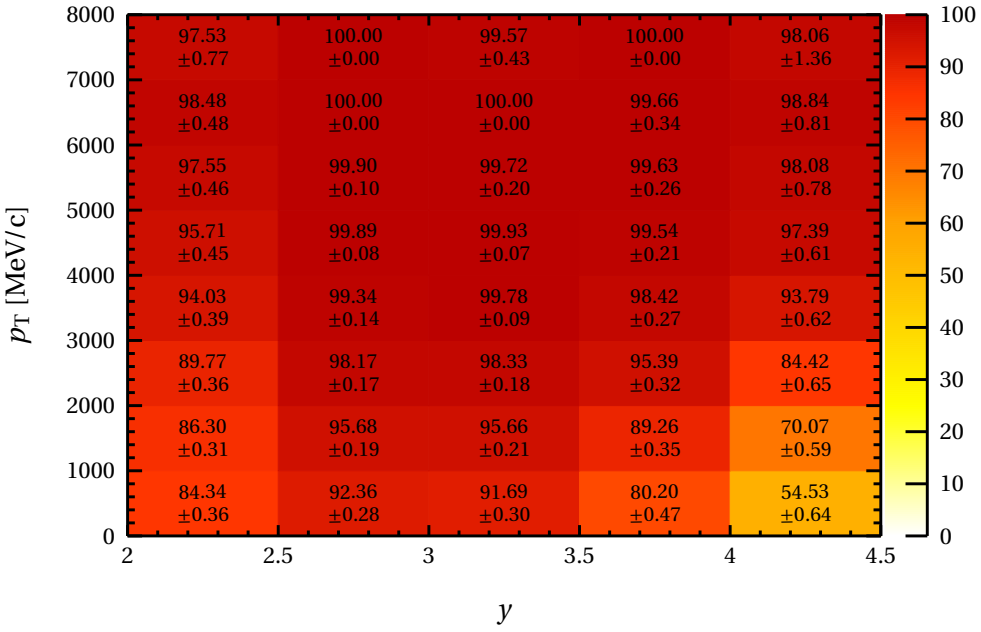

(a) Detector acceptance efficiency of $D_s^+ \to (\phi \to K^- K^+)\pi^+$ decays

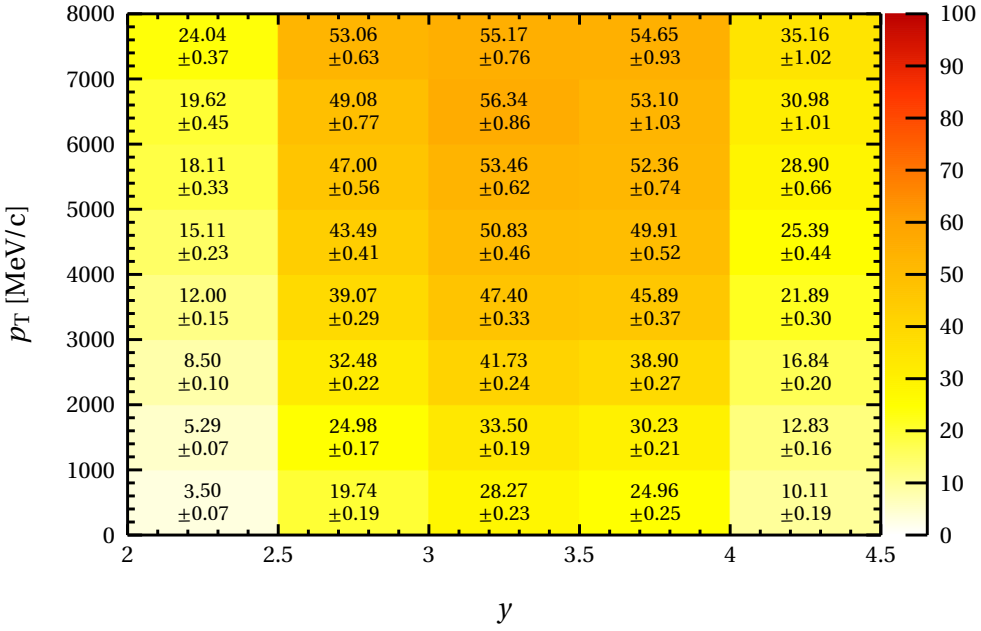

(b) Mother reconstruction efficiency for $D_s^+ \to (\phi \to K^- K^+)\pi^+$ decays

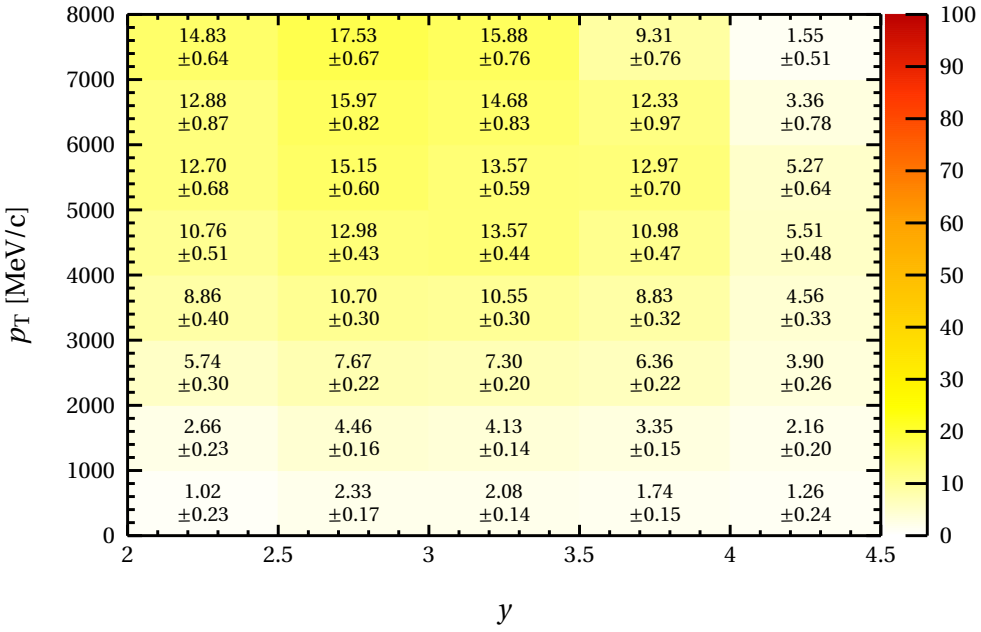

(c) Candidate preselection efficiency for $D_s^+ \to (\phi \to K^- K^+)\pi^+$ decays

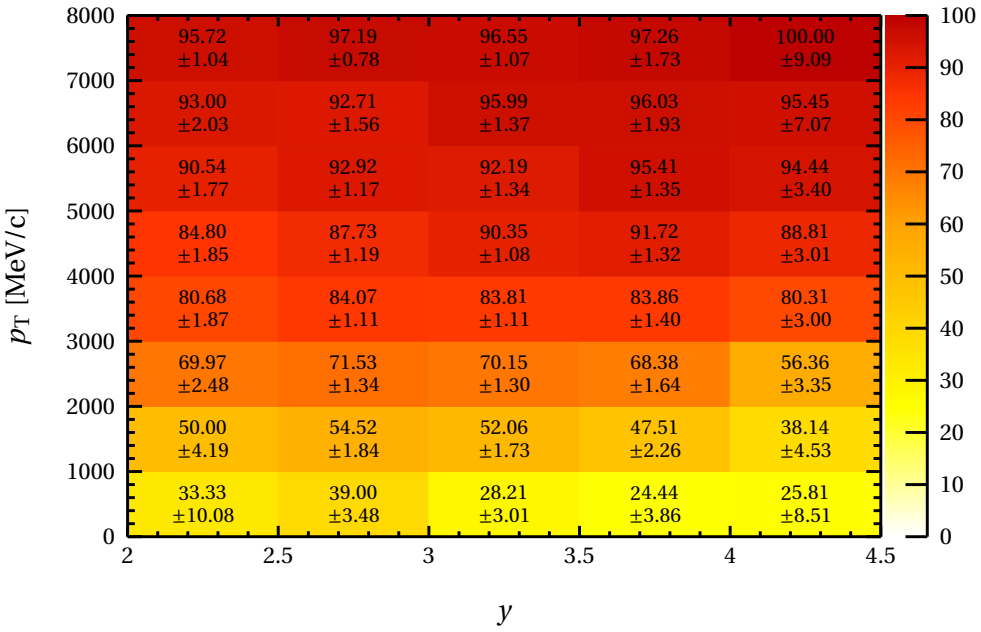

(d) Candidate BDT selection efficiency for $D_s^+ \to (\phi \to K^- K^+)\pi^+$ decays

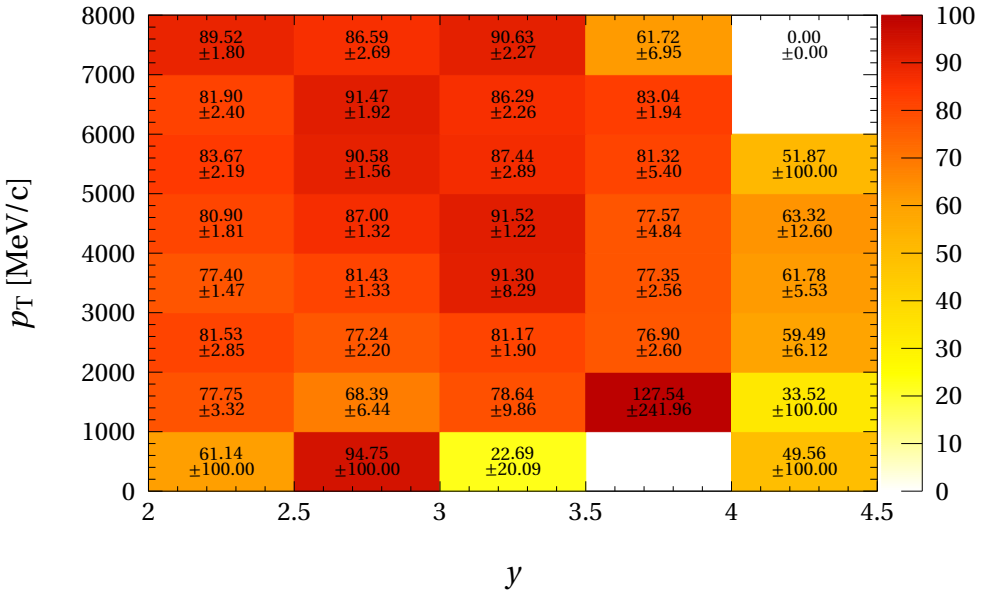

(e) Candidate particle identification selection efficiency for $D_s^+ \to (\phi \to K^- K^+)\pi^+$ decays

Figure E.0.6: Efficiency chain for $D_s^+ \to (\phi \to K^- K^+)\pi^+$ decays

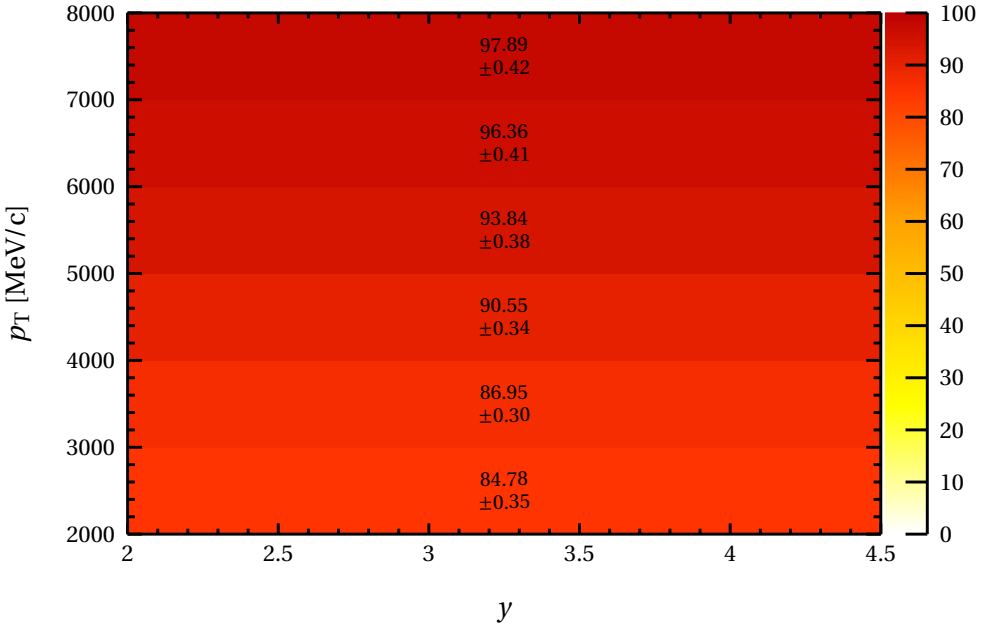

(a) Detector acceptance efficiency of $\Lambda_c^+ \to pK^-\pi^+$ decays

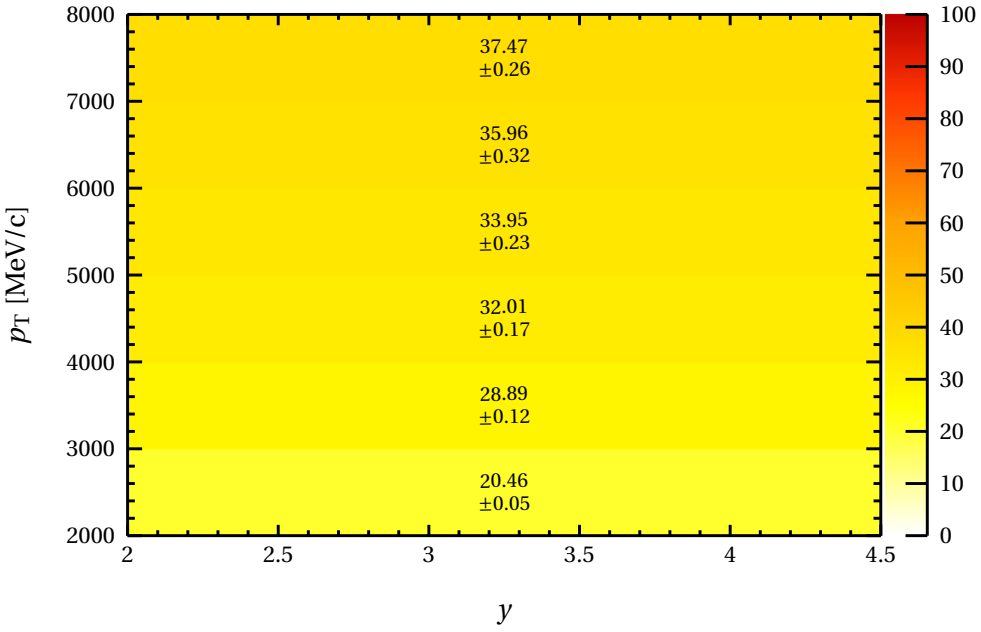

(b) Mother reconstruction efficiency for $\Lambda_c^+ \to pK^-\pi^+$ decays

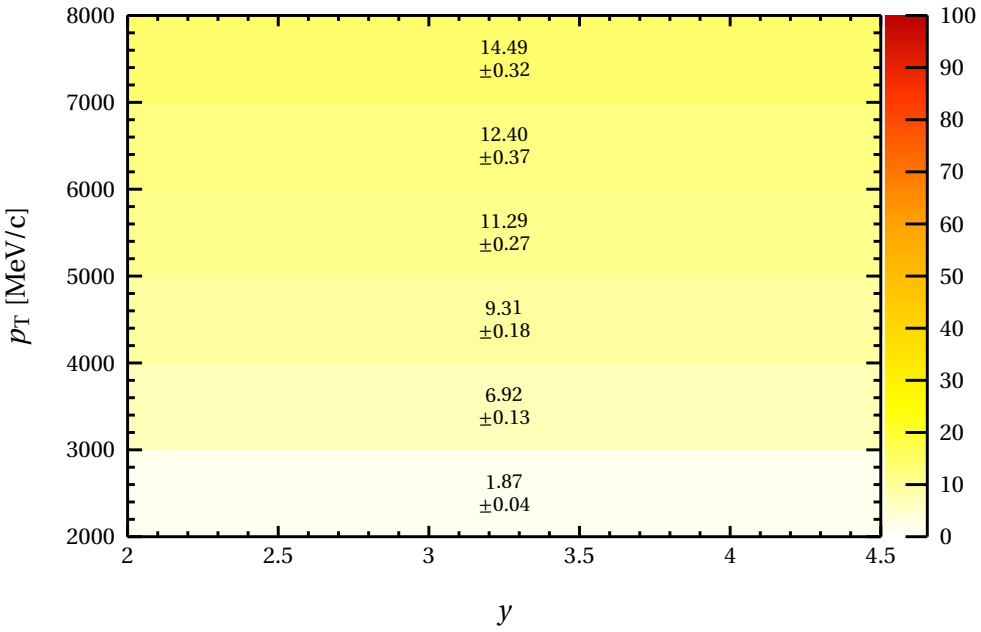

(c) Candidate preselection efficiency for $\Lambda_c^+ \to pK^-\pi^+$ decays

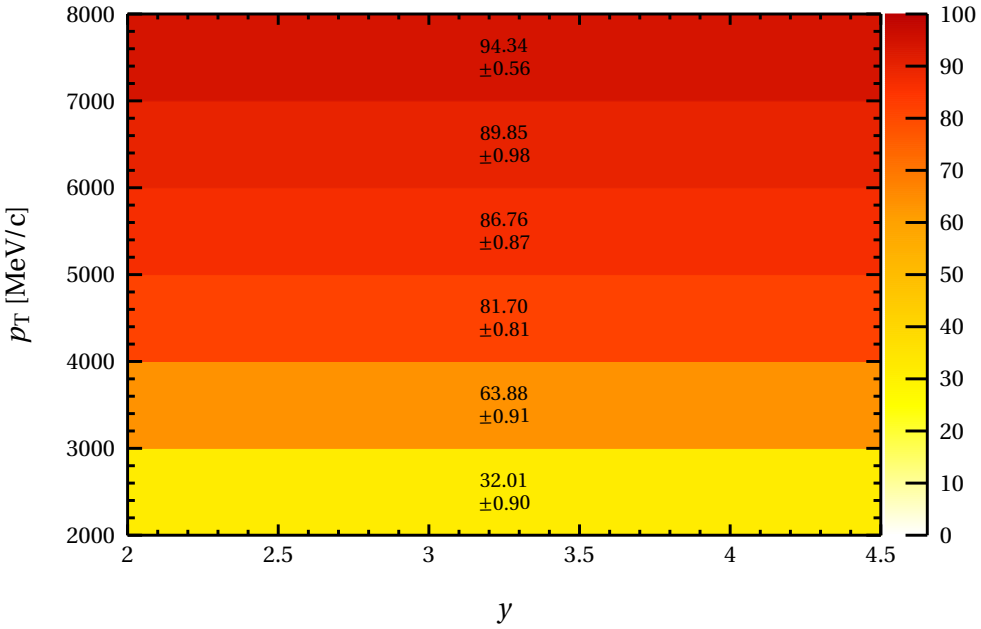

(d) Candidate BDT selection efficiency for $\Lambda_c^+ \to pK^-\pi^+$ decays

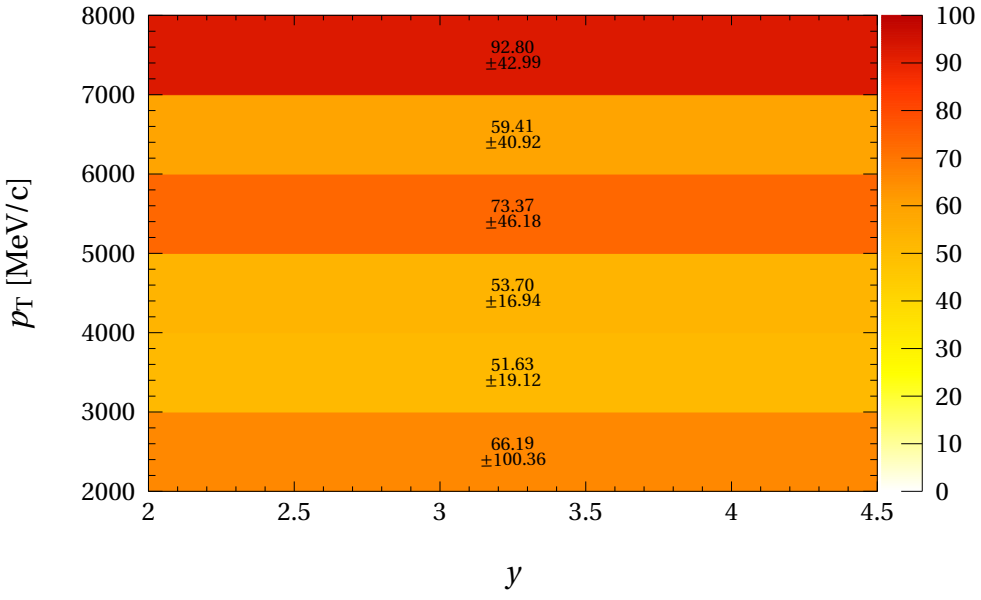

(e) Candidate particle identification selection efficiency for $\Lambda_c^+ \to pK^-\pi^+$ decays

Figure E.0.7: Efficiency chain for $\Lambda_c^+ \to pK^-\pi^+$ decays